University of Kentucky

UKnowledge

2020

DEVELOPING AND TESTING REDOX ACTIVE ORGANIC MOLECULES FOR NONAQUEOUS REDOX FLOW BATTERY APPLICATIONS

Nuwan Harsha Attanayake
University of Kentucky, harsha.attanayake@uky.edu
Author ORCID Identifier:
https://orcid.org/0000-0002-1741-8847
Digital Object Identifier: https://doi.org/10.13023/etd.2020.485

Right click to open a feedback form in a new tab to let us know how this document benefits you.

STUDENT AGREEMENT:

I represent that my thesis or dissertation and abstract are my original work. Proper attribution has been given to all outside sources. I understand that I am solely responsible for obtaining any needed copyright permissions. I have obtained needed written permission statement(s) from the owner(s) of each third-party copyrighted matter to be included in my work, allowing electronic distribution (if such use is not permitted by the fair use doctrine) which will be submitted to UKnowledge as Additional File.

I hereby grant to The University of Kentucky and its agents the irrevocable, non-exclusive, and royalty-free license to archive and make accessible my work in whole or in part in all forms of media, now or hereafter known. I agree that the document mentioned above may be made available immediately for worldwide access unless an embargo applies.

I retain all other ownership rights to the copyright of my work. I also retain the right to use in future works (such as articles or books) all or part of my work. I understand that I am free to register the copyright to my work.

REVIEW, APPROVAL AND ACCEPTANCE

The document mentioned above has been reviewed and accepted by the student's advisor, on behalf of the advisory committee, and by the Director of Graduate Studies (DGS), on behalf of the program; we verify that this is the final, approved version of the student's thesis including all changes required by the advisory committee. The undersigned agree to abide by the statements above.

<div align="right">

Nuwan Harsha Attanayake, Student

Dr. Susan Odom, Major Professor

Dr. Yinan Wei, Director of Graduate Studies

</div>

DEVELOPING AND TESTING REDOX ACTIVE ORGANIC MOLECULES FOR
NONAQUEOUS REDOX FLOW BATTERY APPLICATIONS

_____

DISSERTATION
_____

A dissertation submitted in partial fulfillment of the
requirements for the degree of Doctor of Philosophy in the
College of Arts and Sciences
at the University of Kentucky

By
Nuwan Harsha Attanayake
Lexington, Kentucky
Director: Dr. Susan Odom, Professor of Chemistry
Lexington, Kentucky
2020

ABSTRACT OF DISSERTATION

DEVELOPING AND TESTING REDOX ACTIVE ORGANIC MOLECULES FOR
NONAQUEOUS REDOX FLOW BATTERY APPLICATIONS

Non-emissive, sustainable energy sources such as solar, wind, and geothermal power have continued to provide an increasing amount of electricity to support electrical grids. Due to the intermittent nature of renewable energy sources like wind and solar, grid energy storage systems must adjust for variations in and mismatches between electricity production and consumption. Among the available energy storage technologies, redox flow batteries (RFBs) are expected to play a critical role in the grid energy storage due to their decoupled energy and power, long service life, and simple manufacturing. However, the worldwide market penetration of RFB systems is still limited due to technical and economic challenges. The commercially available aqueous vanadium redox flow batteries offer durable performance but suffer from low energy density and high chemical costs. A key advantage of transitioning from aqueous to nonaqueous systems is the possibility of achieving higher energy density through the wider windows of electrochemical stability associated with organic solvents. Further, nonaqueous systems would provide a greater selection of redox materials which do not fit into the aqueous systems due to lower solubility, instability or redox potentials outside the stability window of water. Despite these promises, nonaqueous flow batteries are still an immature concept and, to date, no redox chemistry has proven competitive due to a combination of low solubility and stability of redox couples and a lack of selective membranes/separators.

This thesis focuses on designing and testing robust, redox active organic molecules intended for use as either positive or negative active materials in nonaqueous RFBs. The two main redox active cores evaluated in this study are phenothiazine (as a positive active material) and viologen (as a negative active material) where both served as learning platforms. The molecules were functionalized through simple and scalable molecular synthetic approaches with particular emphasis on increasing solubility, ionic conductivity, redox potential, and chemical stability. Further, change in chemical stability of variably functionalized electron donating redox active organic cores (phenothiazine, triphenylamine, carbazole, dialkoxybenzene, and cyclopropenium) with different oxidation potentials was explored to identify the correlation between chemical stability of charged forms (radical cation) and coulombic efficiency in galvanostatic cycling. The analysis of chemical and electrochemical stabilities of developed redox active materials were conducted through a variety of spectro-electro analytical technique including cyclic voltammetry, UV-vis spectroscopy, bulk electrolysis, and flow cell cycling.

Nuwan Harsha Attanayake

(Name of Student)

08/05/2020

Date

DEVELOPING AND TESTING REDOX ACTIVE ORGANIC MOLECULES FOR
NONAQUEOUS REDOX FLOW BATTERY APPLICATIONS

By
Nuwan Harsha Attanayake

Dr. Susan A. Odom
Director of Dissertation

Dr. Yinan Wei
Director of Graduate Studies

08/05/2020
Date

To my family

None of this would be possible without your unyielding love, support, and encouragement.

ACKNOWLEDGMENTS

providing financial support to pursue many projects to develop stable and scalable materials for redox flow battery applications.

TABLE OF CONTENTS

LIST OF TABLES

LIST OF FIGURES

CHAPTER 1. INTRODUCTION

1.1   Demand for the Renewable Energy Sources and State of Grid Energy Storage

Current global energy demand is mainly fulfilled by the fossil fuels, such as coal, oil, and natural gas. According to 2018 report of International Energy Agency (IEA), about 80% of total global energy consumption is delivered from fossil fuel sources.[1] The Energy Information Administration (EIA) annual review (2018) reported that about 64% of electricity generated in the United States (U.S.) was delivered from fossil fuels, about 19% from nuclear energy, and about 17% from renewable energy sources.[2] However, severe depletion of fossil fuel reserves has occurred due to excessive usage. For example, global crude oil reserves deplete at a rate of more than 4 billion tons per year, and it has been predicted that oil deposits could run out by 2050.[3-4] Also, the combustion of fossil fuels mainly releases CO_2 and other green-house gases like N_2O, which will likely have negative impacts on global climate.[5-6] Thus, the demand for the non-emissive renewable energy sources, such as solar, wind, hydroelectric, geothermal, etc. has been increasing across the world.[5, 7-8] Hydroelectric and geothermal power sources are limited in amount due to geographical constraints. Solar energy and wind power are more promising alternatives for vast expansion.[9-10] Energy generation from solar and wind is intermittent, so scalable and cost-effective electrical energy storage technologies are expanding in order to implement a greater quantity of intermittent renewable energy onto the electrical grid.

Over the last few decades, a number of grid energy storage technologies have been introduced including thermal, pumped hydro, compressed air, and chemical/electrochemical systems.[11] According to the Grid Energy Storage report of U.S. Department of Energy (DOE), as of May 2019, the U.S. had approximately 31.2 GW of rated power in energy storage capacity, which represents about 2.4% of overall U.S. electricity generation. About 95% of total energy storage capacity is still provided by pumped hydro systems. The remaining 5% of overall storage capacity is provided by other storage technologies such as compressed air, thermal energy storage, batteries, and flywheels.[12-13] Electrochemical devices tend to receive more attention, as they can be installed without the geographical/geological restrictions placed on technologies that

require movement of air or water, and they have a further benefit of being more energy dense.
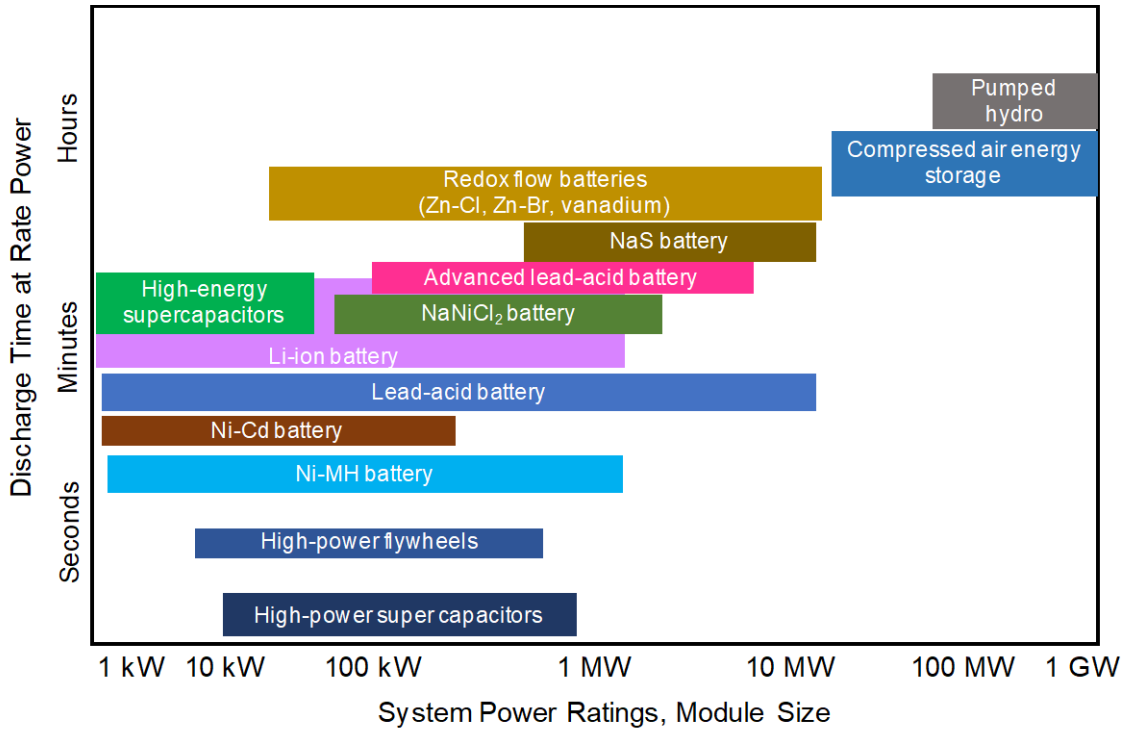
Figure 1.1. Comparison of current electrochemical energy storage (EES) technologies and associated power ratings and discharge time. Figure was taken from DOE/EPRI 2013 electricity storage handbook.[13]

To date, a set of electrochemical energy storage (EES) options have been proposed for grid energy storage, although no EES technology is ready to fulfill the current demand due to techno and economic drawbacks. The different EES technologies with their power and discharge time is given in the Figure 1.1, which is adapted from a recent Sandia National Laboratory report.[13] The pumped hydro and compressed air technologies are shown for comparison to the current EES technologies. According to this general, battery technologies are still positioned around lower power and shorter discharge time compared to the well-known pumped hydro technology. Redox flow batteries (RFBs) show relatively better performance in terms of power and discharge time, thus, it could be a promising technology for grid-scale energy storage in the future.[14]

1.2   Redox Flow Battery: A Promising Candidate for Grid Energy Storage

A redox flow battery (RFB) is a rechargeable electrochemical device that contains separated liquid reservoirs housing solutions of negative and positive materials for charge storage. RFBs have been recognized as a promising technology for grid scale energy storage. Figure 1.2 shows a schematic of a RFB.
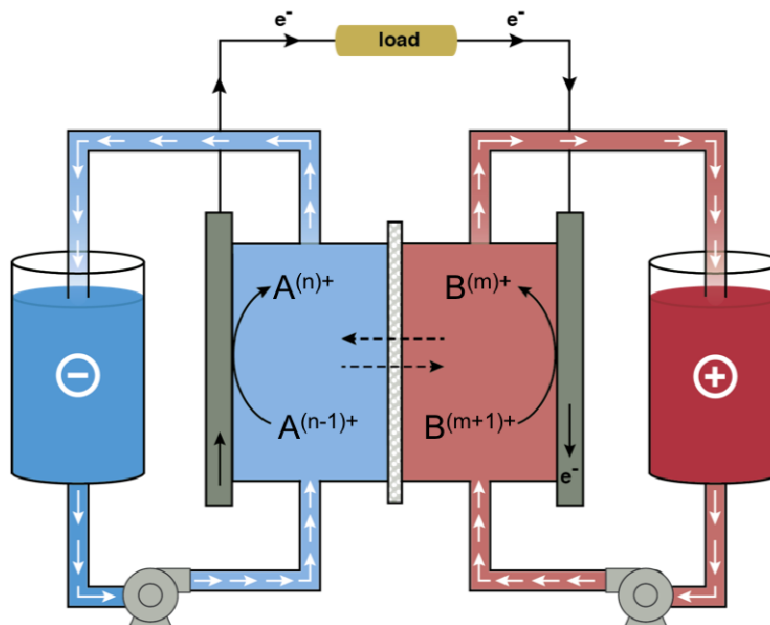
Figure 1.2. Schematic diagram of a redox flow battery in its discharge state. A: negolyte (oxidize during discharge), B: posolyte (reduce during discharge). This image was taken from the Brushett Research Group at MIT (https://www.brushettresearchgroup.org).

A flow battery system includes electrochemical cells, storage vessels, circulation pumps, and power conditioning equipment. Photographs of small volume custom flow cell components, an assembled flow cell, and an operating flow cell are shown in Figure 1.3 Unlike commercially available enclosed battery types (e.g., lithium ion, nickel-metal hydride), RFBs utilize redox active species that are dissolved in liquid electrolytes and stored in external storage vessels. The redox active positive electrolyte (high oxidation potential material) is known as the posolyte, and the negative electrolyte (low oxidation potential material) is known as the negolyte. An electrochemical cell is mainly comprised of two electrodes and an ion-selective membrane or a nano-porous separator in between flow fields (Figure 1.3). The membrane separates both electrodes and prevents mixing of positive and negative electrolytes.[14-15]
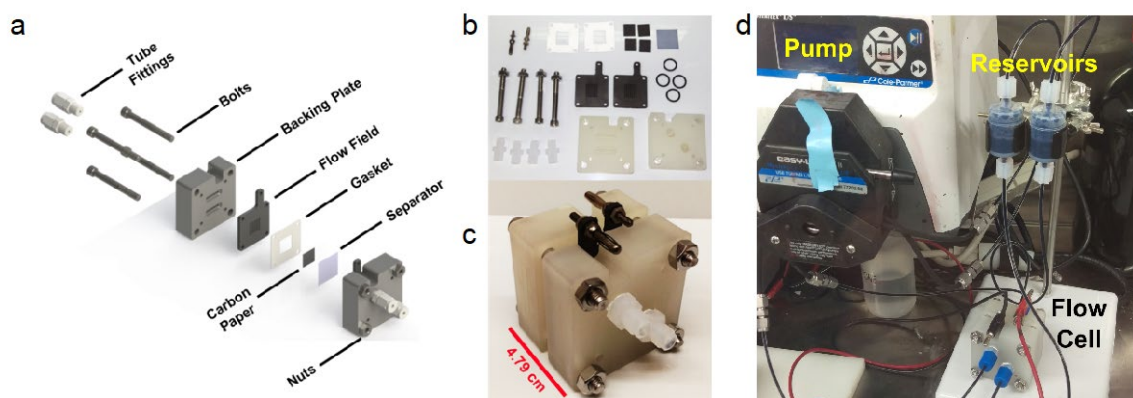
Figure 1.3. Schematic of the small volume custom flow cell parts (a), photograph of flow cell components. (c) an assembled flow cell connected to storage vessels and pump (d). Figure was taken from Ref. 14 with permission from The Royal Society of Chemistry. (J. D. Milshtein, A. P. Kaur, M. D. Casselman, J. A. Kowalski, S. Modekrutti, P. L. Zhang, N. Harsha Attanayake, C. F. Elliott, S. R. Parkin, C. Risko, F. R. Brushett and S. A. Odom, *Energy Environ. Sci.*, 2016, **9**, 353. **DOI:** 10.1039/C6EE02027E).

The electrolyte solution, stored in storage vessels, is circulated between two electrodes, upon operation of the flow cell. The posolyte is oxidized and negolyte is reduced during charging, storing energy in the liquid electrolytes housed in external reservoirs. During discharge, the opposite occurs: The posolyte is reduced and negolyte is oxidized, releasing energy. The electrochemical reactions occur at the surface of the electrodes, which are made of carbon foams, felts, or papers. In an ideal situation, an ion-selective membrane that separates the electrolytes is permeable to the ionically conductive, supporting salt and prevents redox active species from crossing. Thus, the supporting salt transfers in between positive and negative sides of the flow cell to balance the electroneutrality while charging and discharging. The unique architecture of RFBs offers compelling features towards the grid energy storage compared to the other existing battery technologies as follows,[5, 13, 16-18]

- Power and energy densities can be independently scaled up as electrochemical cells and storage vessels are separated.
- Long lifetimes with deep charge and discharge abilities are possible.
- Improved safety as active species are stored in physically separated tanks.
- Manufacturing can be simplified.

The history of RFB goes to 19th century where the first RFB-type battery was conceptualized in 1884 by Charles Renard using zinc and chlorine as the active species. The battery powered the air ship La France, and flew several trips around Paris.[19] The complexity of the battery architecture, hydrogen evolution at the negative electrode, dissolution of chlorine at the positive electrode during, and slow oxidation of graphite electrode by corrosive chlorine gas all limited the utilization of the Zn/Cl_2 RFBs.[20] In the 1970s Lawrence Thaller at The National Aeronautics and Space Administration (NASA) invented a different RFB architecture for storing solar power on a spacecraft.[21] Thaller employed a Fe/Cr redox couple in acidified electrolytes (generally aqueous HCl solutions) as the active components. The modern RFB evolved from his design. The use of this battery technology was limited due to the poor reversibility and slow kinetics of the Cr^{3+}/Cr^{2+} redox couple, and dramatic capacity decay was caused by active species crossover through the ion-exchange membrane.[19] Also, the Fe/Cr RFB showed only a modest energy density (15 Wh/L) due to low cell potential and limiting solubility.[22] About a decade later, in 1986, Skyllas-Kazacos and Robins patented a vanadium-based RFB utilizing V^{5+}/V^{4+} and V^{3+}/V^{2+} redox couples in acidic electrolytes as the energy-storing active species.[23] The all vanadium system was a huge breakthrough during that time period due to its relatively higher cell voltage (1.25 V) and lower active species crossover, as the same active species are present in the both compartments of the battery in different states of charge (SOC). The performance of vanadium redox flow batteries (VRFBs) has significantly improved over the last 40 years and to date, they are the most commonly used RFB.

Despite to the advantages of RFBs, worldwide market penetration has been limited largely due to high system cost and low energy density.[24] The energy density of commercially available VRFBs (15-45 Wh/L) is lower than the enclosed batteries in market such as lead-acid (80-90 Wh/L) and lithium-ion (75-200 Wh/kg) batteries.[25] The lower energy density can be tolerated for RFBs being used for stationary storage applications. Also, as RFBs require pumps to circulate the electrolytes, it causes a loss in round trip energy efficiency (round trip efficiency is typically 65-75%), which raises an obstacle to operate RFBs independently on the grid.

1.3   Aqueous vs. Nonaqueous Redox Flow Batteries

To date, the majority of flow battery chemistries are based on aqueous electrolytes and similarly, polar organic solvents can also be utilized to prepare electrolytes for RFBs. Because water is abundant, costs little, non-volatile, inflammable, and non-toxic, it is a desirable medium for RFB electrolytes. In addition, aqueous based electrolytes have significantly higher conductivities compared to nonaqueous counterparts, thus mitigating the overpotential losses during constant current charging process in flow batteries. For instance, a solution of 1 M tetraethylammonium tetrafluoroborate (TEABF$_4$) in acetonitrile (ACN) shows an ionic conductivity of 55.5 mS cm^{-1}, a value that is 86% less than the ionic conductivity of 1 M aqueous sulfuric acid (394.5 mS cm^{-1}), 73% less than the 1 M aqueous potassium hydroxide (209 mS cm^{-1}), and 35% less than the 1 M aqueous sodium chloride (85.7 mS cm^{-1}).[26] The major drawback of aqueous electrolytes is their relatively narrow electrochemical windows. The thermodynamic dissociation potential for water, under standard conditions, is 1.229 V (25 °C, 100 kPa) where water oxidizes to oxygen and reduces to hydrogen at this potential.[27] Gas evolution not only constrain the cell voltage of RFBs but also results in parasitic Faraday losses. This is a safety hazard, as both gases are flammable. By changing the supporting electrolyte to eliminate water and other polar protic solvents, the stable electrochemical window can be broadened via suppressing hydrogen and oxygen evolution reactions to increase the cell voltage, thus energy density of the battery.[24, 28] Further, nonaqueous electrolytes offers new pathways to design redox couples that may otherwise be incompatible with aqueous systems due to either limited solubility, stability, or redox potentials that lie outside the electrochemical window of aqueous electrolytes.

The first nonaqueous RFB concept was proposed by Singh in 1984. These early reports were limited to cell designing, and it was not a popular battery technology at the time.[29] Singh discussed how the performance of RFBs (Fe/Cr and VO$_2^+$/V^{3+}) and redox chemistry of other metal-ligand compound could be improved by moving from water to nonaqueous solvents.[30] After 2012, researchers revisited nonaqueous RFB technologies and as a viable pathway to increase the energy density of RFBs by expanding the cell voltage. Recent literature reports have demonstrated the use of polar organic solvents including carbonates, nitriles, ether, and amides, which are appealing due to their stable

electrochemical windows, broader working temperature ranges, viscosities, and relative permittivities.[26, 31] Table 1.1, was adapted from ref. 26 and 31, compares these physical properties of commonly used organic solvents to water.

Table 1.1. Freezing point and boiling point, limiting oxidation and reduction potential (using 0.65 M TEABF$_4$ as supporting salt), viscosity, and relative permittivity of water and organic solvents. (adapted from Ref. 26 and 31).

Solvent	Freezing Point (°C)	Boiling Point (°C)	Electrochemical Window			Viscosity (mPa s)	Relative Permittivity
			E_{ox} (V vs. SHE)	E_{red} (V vs. SHE)	Voltage difference (V)		
Water (H$_2$O)	0	100	0.4 (at pH 14), 1.23 (at pH 0)	-0.83 (at pH 14), 0 (at pH 0)	1.23	0.89	78.2
acetonitrile (ACN)	-44	82	3.5	-2.6	6.1	0.34	35.9
g-valerolactone (GVL)	-31	208	5.4	-2.8	8.2	2.00	42.0
propylene carbonate (PC)	-49	242	3.8	-2.8	6.6	2.53	64.9
N,N-dimethylformamide (DMF)	-60	153	1.9	-2.7	4.6	0.92	36.7
1,2-dimethoxyethane (DME)	-69	85	2.3	-3.3	5.6	0.46	7.20
dichloromethane (DCM)	-95	40	1.8	-1.8	3.6	0.39	8.93
tetrahydrofuran (THF)	-108	66	2.8	-2.9	5.7	0.46	7.58

Aqueous-based electrolytes are at risk of freezing at sufficiently low temperatures, posing a significant challenge to operating them in cold climates. Even though dissolving solutes/electrolytes may suppress the freezing point of the water and elevate the boiling point, the effect is limited. By contrast, most of the common organic solvents have considerably low freezing points (lower than water) and appreciably high boiling points, allowing nonaqueous RFBs to operate over a wider temperature range. For instance, THF and DMF have freezing points of -108 °C and -60 °C, respectively (Table 1.1) and boiling points of 66 °C and 153 °C, respectively. Thus, these and other organic solvents offer a potential solution for low temperature batteries broadening the spectrum of nonaqueous

RFB applications. The freezing points and boiling points of a few common nonaqueous solvents are given in Table 1.1.

As previously stated, narrow electrochemical window (1.23 V) of water at standard conditions (25 °C, 100 kPa) limits the fundamental cell voltage of aqueous RFBs, which prevents the possibility of achieving higher energy densities. By contrast, most of the commonly used organic solvents offer stable, wider electrochemical window (4-5 V), allowing for the design redox active species to achieve higher cell voltage without concerns of solvent breakdown during the cell's charge/discharge process. Table 1.1 shows the stable voltage windows of a few solvent in the presence of TEABF$_4$ as the supporting electrolyte. Sanford *et al.* recently reported an all organic nonaqueous RFB study using ACN as the solvent and 0.5 M TBAPF$_6$ as the supporting electrolyte in which a cell voltage of 3.2 V was reached, demonstrating the feasibility of achieving higher cell voltage with polar aprotic organic solvents.[32]

The viscosity of the solvent/electrolyte for RFB technologies needs to be taken into account as it affects the ionic conductivity of solutions (aqueous/nonaqueous) and the pumping cost of the flow cell. In general, lower solvent viscosity would lead to a higher ionic conductivity for a given supporting salt and may decrease the pumping cost at a given flow rate of electrolyte due to low fluidic resistance.[33] Further, high solvent viscosity may limit the diffusivity and mobility of the active species and supporting salt, which may raise mass transfer limitations, leading slower kinetics in electrochemical reactions. In addition to solvent viscosity, ionic conductivity and solubility of active species depends on the relative permittivity (dielectric constant) of the solvent. Also, the relative permittivity determines the solubility of ionic electrolytes/ supporting electrolytes and their dissociation constant when they dissolved. Viscosity and relative permittivity of a few organic solvents are provided in Table 1.1. Among them, ACN shows balanced physical properties to be used in nonaqueous flow batteries with a broader stable electrochemical window (6.1 V), low viscosity (0.34 mPaS), high relative permittivity (35.9), and a moderate boiling point of 82 °C (Table 1.1). In addition, DME and PC are the next most widely utilized polar aprotic organic solvents in nonaqueous RFBs due to their chemical and physical properties.

Although nonaqueous chemistries show promising features towards the growth of flow battery technologies, superior to the aqueous chemistry described above, a few major

drawbacks have impeded the utilization of nonaqueous electrolytes beyond research laboratories, as described below. For instance, although nonaqueous solvents are capable in providing stable and broader electrochemical windows, only a very few laboratory developed cells containing organic/inorganic active species have exhibited cell voltages of > 3 V.[32] The remainder of the reported nonaqueous RFBs rarely exceed the cell voltage of well-performing aqueous RFBs (1 to 2 V).[16, 34-35] Further, laboratory prototypes with high cell voltage materials have exhibited comparatively low lifetimes and reduced coulombic efficiencies compared to active materials with lower cell voltage in nonaqueous electrolytes.[32, 34] According to recently published results, it seems that battery lifetime must be compromised to achieve high cell voltages in nonaqueous electrolytes due to less chemical stability of charged species at their extreme redox potentials .[32, 36] The other major challenge of utilizing nonaqueous electrolytes is their low ionic conductivity in comparison to their aqueous counter parts, which limits power densities – a factor that is critical for the commercialization of nonaqueous RFBs. Furthermore, concerns about nonaqueous electrolytes due to their flammability and the cost of organic solvents and supporting electrolytes are hurdles for the widespread adoption of flow batteries in the market.

1.4 DOE Capital Cost Targets for an Economically Viable Energy Storage System

Current RFB prices are too expensive for widespread market penetration. The overall cost per kWh of a redox flow battery depends on the cost of the cell components and the electroactive species. In 2014, the capital cost of RFBs exceeded $500 per kWh.[37] However, recent studies have demonstrated that RFBs can meet the Department of Energy (DOE) capital cost target of $100 per kWh by appropriately decreasing the cost of RFB reactors and materials. In 2016, Dmello et al.[38] proposed a techno economic (TE) model to reduce battery prices to $100 per kWh as a comparison to a 2014 TE model by Darling et al.[24] In this new TE model, the authors considered redox active material concentration and cost, solvent and salt cost, cell voltage, area-specific resistance (ASR), and reactor cost for both families of RFBs, to reduce the battery price. According to their recommendations, the following improvements are needed to achieve desired $100 per kWh battery price target for nonaqueous RFBs: active species cost of < $7 Kg^{-1}, active material concertation

of 2-4 mol kg^{-1}, cell voltage of 2.8 V, ASR of < 5 ohm cm^2, and salt cost of < \$0.5 mol^{-1}.[24, 38]

1.5 Redox Active Organic Materials for Nonaqueous Redox Flow Batteries

Traditional RFBs utilize redox active inorganic compounds such as, $Fe^{2+/3+}$,[39-41] $Ni^{2+/3+}$,[42] $Zn^{0/2+}$,[43-44] Br_2,[45-46] $Cr^{0/3+}$,[47-48] etc. as active components in RFBs. Several classes of redox active materials have been investigated for nonaqueous RFBs, including organic molecules, metal-centered complexes,[49-50] and redox active polymers/colloids.[51-52] Even though aqueous vanadium electrolytes are state-of-the-art in RFB technologies, the high cost (ca. \$24/kg for V_2O_5) and low abundance of vanadium limit the widespread adoption of this battery technology.[53] However, redox active organic molecules are of particular interest for low-cost RFBs because they consist of earth abundant elements (e.g. carbon, oxygen, and hydrogen). Further, working with molecular species (rather than metal ions) provides an opportunity to modify physical and electrochemical properties (e.g. solubility, electrochemical stability, redox potential, and ionic conductivity) to better meet performance requirements. While recent molecular engineering efforts have focused on multi-property optimization to increase active species solubility and stability for high energy density RFBs, to date, only a few molecular cores have shown promise as potential active materials, including derivatives of benzoquinone,[54] anthraquinone,[55] nitroxyl radicals,[56] dialkoxybenzenes,[16] phenazine,[57] cyclopropeniums,[58] pyridiniums,[59] viologen,[60] and phenothiazine.[61]

With many choices of organic redox couples, it is crucial to select an appropriate molecular core that can be easily functionalized to obtain desired properties for flow battery applications. The following properties may be considered when selecting organic redox couples: low-cost starting materials that can be purchased in bulk, high-yielding and short syntheses, and potential to have multiple stable charged states (e.g. radical cation, dication). Redox active materials are the key components of RFBs, and their physicochemical properties mainly determine the performance of the battery. Thus, increasing solubility of active species across all states of charge and tuning redox potential (high oxidation potentials for posolytes and low oxidation potentials for negolytes) without

compromising their chemical stability is important to build high energy, high power and long running RFBs. Over the past decade, different molecular design strategies have been reported in literature to optimize the physicochemical properties of organic redox active materials for nonaqueous RFBs.
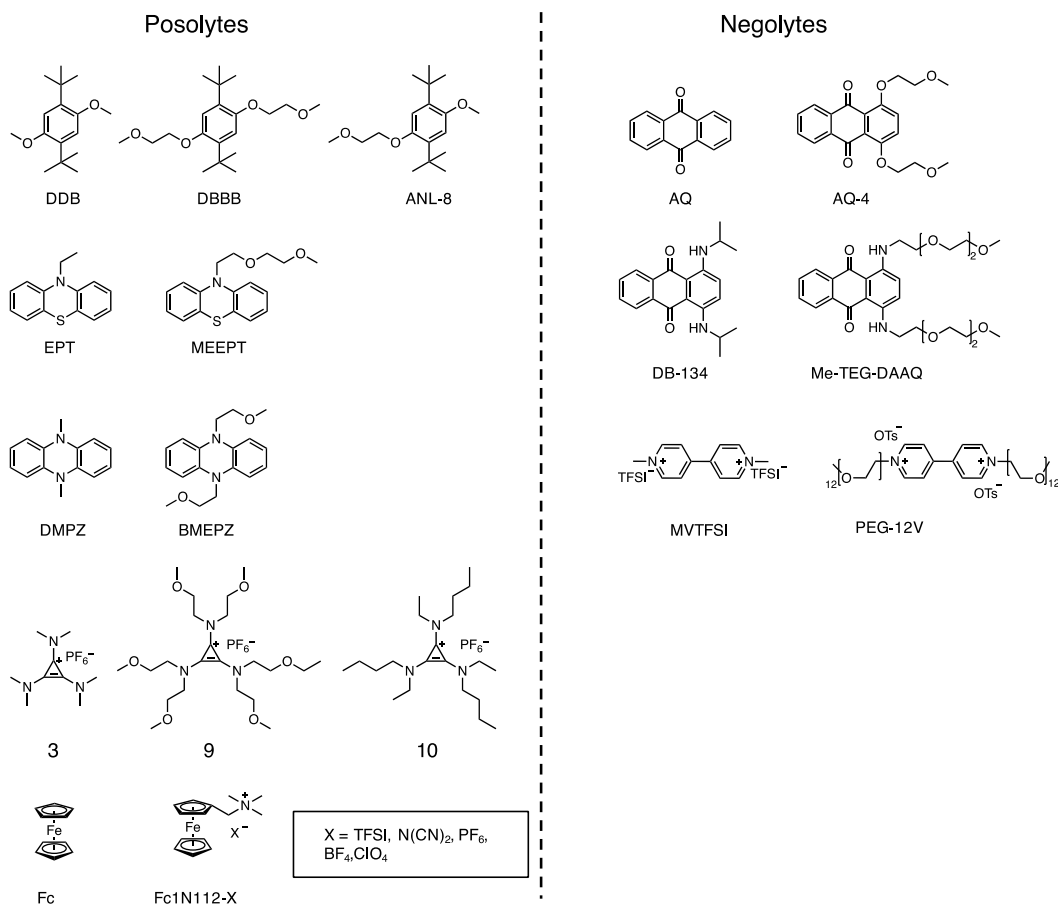
Figure 1.4. Solubility increasing approaches of posolytes and negolytes in nonaqueous RFBs. Posolytes are listed on the left side and negolytes are listed on the right side. Right side (from top to bottom); dialkoxybenzene, phenothiazine, cyclopropenium, and ferrocene derivatives. Right side (from top to bottom); anthraquinone, 1,4-diaminoanthraquinone, and viologen derivatives.

1.5.1 Solubility

The high solubility of redox active organic molecules in electrolyte solutions, not only increases the volumetric energy density of the battery, also minimizes cost of the solvent (especially for nonaqueous RFBs). When reporting solubility values, it is important to report the solubility of active species in a particular electrolyte solution under both

charged and discharged forms, as solubility could be varied from electrolyte to electrolyte and the state of the charge. However, most of the recent literature reports have included only the solubility of discharged form of the redox active organic species, either due to charged form of the organic molecules are highly unstable to isolate or synthetic challenges. High solubility can be achieved by either applying various molecular designing strategies or modifying the chemical environment (solvent and electrolyte). As shown in the Figure 1.4, the introduction of polar functional groups or charged substituents is one of the promising ways to increase the solubility of active species in polar organic solvents, across all the states of charge. Also, solubility can be increased by increasing the entropy of the molecules or decreasing the intermolecular interactions in a particular solvent (Figure 1.4).

Introducing glycol chains increases the solubility of organic active species in polar organic solvents. Jansen *et al.* prepared DBB as a soluble dialkoxybenzine derivative (0.4 M in carbonate-based electrolytes) by introducing glycol chains (Figure 1.4).[34] Compared to previously reported DDB, DBBB showed about 5-fold higher solubility in the same carbonate electrolytes. Similarly, this molecular design strategy has been utilized to increase the solubility of variety of organic posolytes. Odom *et al.* developed a highly soluble phenothiazine derivative by replacing ethyl group in EPT with a glycol chain (MEEPT), and it is miscible with most of the nonaqueous solvents. Also, its charged form (MEEPT-BF$_4$) showed 0.5 M solubility in 0.5 M TEABF$_4$/ACN electrolyte system (Figure 1.4).[14] Glycol-substituted phenazine derivative (BMEPZ) showed 0.5 M solubility in ACN,[62] which is 8 times higher than the solubility of methyl substituted DMPZ as reported by Kang *et al.*[63] Further, Sanford *et al.* synthesized a cyclopropenium derivative with glycol chains (9, Figure 1.4), to increase the solubility in its charged form.[64] Even though the methyl substituted derivative (3, Figure 1.4) was soluble to 1.5 M in ACN, its charged form solubility is incredibly low in ACN (0.08 M). They found that the introduction of glycol chains increased solubility of its both discharged and charged forms to > 1 M in ACN (1.62 M, 1.05 M respectively). The researchers actively applied this strategy to increase the solubility of negolytes as well. Anthraquinone is a commercially available negolyte compound and its solubility is low in ACN (less than 50 mM). Zhang *et al.* reported that they increased the solubility of this material by introducing glycol chains at

1,4 positions (AQ-4) to 0.47 M in ACN (Figure 1.4).[65] DB-134 is a commercially available dye (disperse blue 134) and exhibits four reversible redox events (two oxidations and two reductions), allowing for the construct of symmetric flow batteries with a 2.72 V theoretical cell voltage. However, this redox couple suffers from low solubility (0.02 M in ACN). Binnemans *et al.* introduced long polyether glycol chains to this diaminoanthraquinone derivative and developed highly soluble (miscible in ACN) Me-TEG-DAAQ.[65] Finally, Jiang *et al.* developed a redox active ionic liquid (negolyte) by introducing long polyether glycol chains to viologen (PEG 12V) that is miscible in most of the nonaqueous solvents (Figure 1.4).[66]

In addition to introducing glycol chains symmetrically to an organic molecule, Zhang *et al.* demonstrated that they can further increase the solubility of DBBB (dialkoxybenzine) and make a highly soluble liquid material at room temperature by introducing glycol chains asymmetrically (ANL-8, Figure 1.4).[67] This also proves that asymmetric substitution further increases the solubility by increasing entropy and disrupting molecular packing. Sanford *et al.* recently reported a highly soluble cyclopropenium derivative by modifying its parent structure (3, Figure 1.4) with asymmetric substituents. The newly developed derivative, 10 (Figure 1.4) is soluble to 1.94 M (in ACN) in its discharged form and 1.64 M (in ACN) in its charged form.[64]

Wang *et al.* demonstrated that introducing ionic substituents is another promising method to increase the solubility of active species. Fc1N112-TFSI (Figure 1.4) showed 20-fold higher solubility than Fc in 1.2 M LiTFSI/carbonate solvents (EC, PC, EMC) electrolyte due to intensified solvent-molecule dynamic interactions through ionic tetraalkylammonium substituent.[67] The solubility of Fc is 0.04 M in 1.2 M LiTFSI / EC, PC, EMC and the solubility of Fc1N112-TFSI is 0.85 M in the same electrolyte. Wang *et al.* further investigated the effect of counter-anions on solubility, using same tetraalkylammonium substituted ferrocene derivative (Fc1N112-X).[68] They found solubility depends on the nature of the anion and it varies as; $N(CN)_2^-$ > $TFSI^-$ > PF_6^- > BF_4^- ClO_4^- in carbonate solvents. In EC, PC, EMC (4:1:5), Fc1N112-N(CN)$_2$ showed the highest solubility of 2.08 M, followed by 1.73 M for Fc1N112-TFSI, 1.71 M for Fc1N112-PF$_6$, 0.63 M for Fc1N112-ClO$_4$, and 0.40 M for Fc1N112-BF$_4$, respectively, in their discharged forms (Figure 1.4).

1.5.2 Stability

The chemical and electrochemical stability of redox active materials determines the cycle life stability of RFBs. In general, the discharged form of redox active materials shows higher stability in most nonaqueous solvents, and their stability significantly drops at the charged form due to formation of unstable radical cations or radical anions. Thus, developing redox active compounds with highly stable charged forms is foremost important to achieve a long lifetime in RFBs. A few examples of molecular design strategies to improve the chemical stability of redox active posolytes and negolytes in nonaqueous solvents are listed in Figure 1.5.
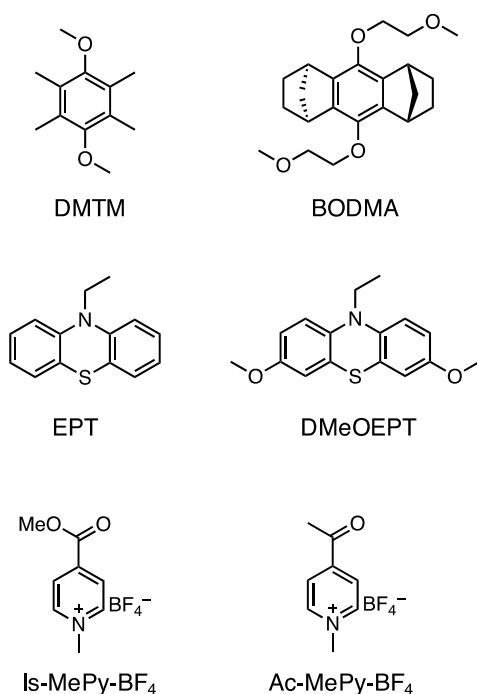
Figure 1.5. Molecular design strategies to increase the stability of redox active organic molecules. From top row to bottom row, molecular representations of; dialkoxybenzene, phenothiazine, and pyridinium.

Zhnag *et al.* developed bicyclic substituted dialkoxybenze derivative (BODMA, Figure 1.5) to improve the chemical stability in its charged state compared to other tetra-substituted dialkoxybenzenes (e.g. DMTM, Figure 1.5).[69] The substitution of arene ring

mitigates parasitic radical reactions through improved conjugation (Figure 1.5). Odom *et al.* demonstrated they can stabilize the second oxidation of *N*-substituted phenothiazines (e.g. EPT) by doing further molecular engineering.[70] Introducing methoxy groups at the 3 and 7 positions extends the delocalization of positive charge in DMeOEPT (Figure 1.5) to stabilize its dication which indeed increase the molecular capacity. Sanford *et al.* screened a series of isonicotinatepyridinium (Is-MePy-BF$_4$) and acetylpyridinium (Ac-MePy-BF$_4$) salts (Figure 1.5) to obtain a chemically stable negolyte material for nonaqueous RFB applications.[59] The long-term stability studies showed that reduced form of Is-MePy-BF$_4$ is highly sensitive to trace water present in the electrolyte system (LiBF$_4$/ACN), thus reduced form decayed in 5 minutes. To enhance the stability, they replace ester group with a ketone group (Ac-MePy-BF$_4$) as ketone enolates have less basicity compared to ester enolates.

1.5.3   Redox Potential

Redox potential determines the cell voltage of the battery, and thus its energy density. A combination of a high oxidation potential posolyte and a low oxidation potential negolyte would lead to a high cell voltage RFB. The redox potential of an organic compound is determined by either adiabatic ionization potential or adiabatic electron affinity potential of a particular compound. Thus, adjusting the free energy levels of HOMO and LUMO of organic molecules through molecular functionalization would change their oxidation potentials. A common method of modifying redox potential is substitution of electron donating or electron withdrawing groups to π-conjugated organic molecules or polymers making use of the well-known Hammett constants as predictors. In general, adding electron-withdrawing groups would lead to a positive shift in the redox potential while adding electron donating groups would result a negative shift.[67-70] This strategy has been widely utilizing in both electron donating and accepting molecules to achieve a larger cell voltage in RFBs. For instance (Figure 1.6), the oxidation potential of ethyl substituted phenothiazine (EPT, a posolyte) can be tuned by adding electron donating or accepting groups at 3,7 position of phenothiazine core. Electron donating, methyl substituted version of EPT (3,7-DMeEPT, 0.13 V vs. Cp$_2$Fe$^{0/+}$)[68] shows a lower oxidation

potential and trifluoromethyl substituted EPT (3,7-BCF$_3$EPT, 0.60 V vs. Cp$_2$Fe$^{0/+}$)[67] shows a greater oxidation potential compared to its underivatized EPT (0.27 V vs. Cp$_2$Fe$^{0/+}$). Similarly, benzothiadiazole (BzNSN, -1.59 V vs. Ag/Ag$^+$) showed more negative potential upon substitution of electron donating methoxy group (MeO-BzNSN, -1.68 V vs. Ag/Ag$^+$) while introduction of electron withdrawing groups (DCN-BzNSN -0.93 V vs. Ag/Ag$^+$) shifts its oxidation potential to more positive (Figure 1.6).[36] In addition, strain-induced disruption of the π-conjugated framework is another molecular design strategy to increase the oxidation potential. Bulky substituents at strategic positions on the π-conjugated framework, disrupt the relaxation of oxidized species, thus, increase the oxidation potential.[71-73] For instances, upon substituting methyl groups at 1,9 positions of EPT, disrupt the relaxation of charged form of 1,9-DMeEPT (Figure 1.6), resulting a positive shift in its oxidation potential (1,9-DMeEPT, 0.53 V vs. Cp$_2$Fe$^{0/+}$).[71] This phenomenon will be further discussed in Chapter 4.
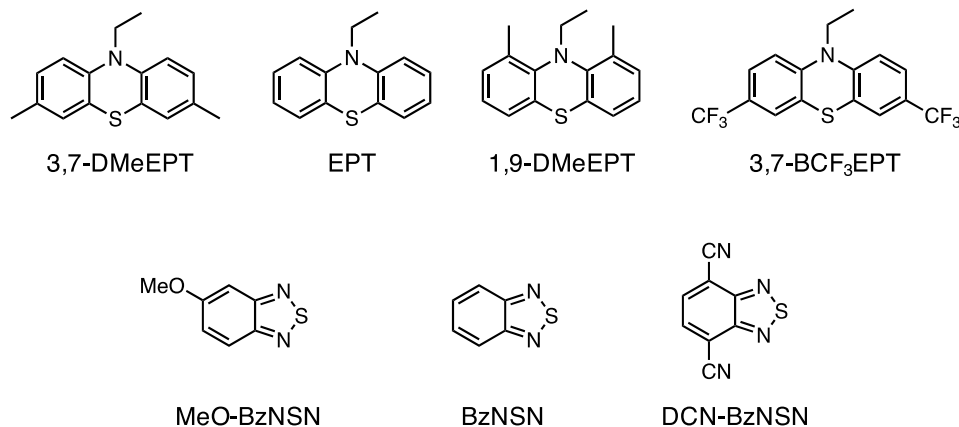
Figure 1.6. Molecular design strategies to tune the redox potential of redox active organic molecules. First row: electron donating phenothiazines, second row: electron accepting benzothiadiazoles.

1.6 Thesis Scope

This thesis aims to identify and solve a set of key challenges in the design and testing of organic electrolytes for nonaqueous RFBs. This is approached by introducing a series of novel and robust molecular engineering principles to enhance their physicochemical properties (e.g. solubility, stability, and redox potential), thus improve the battery performance.

Chapter 2 explores the feasibility of running supporting-salt-free nonaqueous RFBs after developing permanently charged, ionic redox active organic molecules. One approach to increasing the solubility of active materials is to design organic compounds that serve as both the redox active species and the supporting salt; in such a material, a permanently charged substituent would serve to keep ionic conductivity high while a conjugated organic redox moiety would store and release charge. This chapter discusses ionic conductivity changes of newly synthesized active species with the help of viscosity and diffusivity analysis. Further, extensive electrochemical characterization is done through voltammetry and electrochemical impedance spectroscopy. Finally, electrolytes are employed in a supporting-salt-free flow cell to explore their long-term stability in a flow battery environment, and post cycling analysis is performed to understand the capacity degradation.

Chapter 3 demonstrates a multi-property optimization of organic electrolytes through novel synthetic approaches to increase the solubility and stability of species as they undergo multiple electron transfer, simultaneously, utilizing two new phenothiazine derivatives. To quantify the solubility of the new molecules across all the states of charge, the phenothiazine derivatives were chemically oxidized so that their solubility in their charged forms (radical cation and dication) could be evaluated in supporting electrolytes along with their neutral forms. This dual property optimization enables the understanding of the physical and electrochemical behavior of organic redox active molecules at elevated concentrations utilizing symmetric flow battery testing.

Chapter 4 transitions from solubility to redox potential, investigating molecular designing strategies to raise the oxidation potential of phenothiazine derivatives. Designing robust, high voltage electroactive organic materials is important for redox shuttles utilized in overcharge protection in lithium-ion batteries or as posolytes in nonaqueous RFBs. The solid and solution state stability of the charged form of a high voltage material is evaluated through UV-vis spectroscopy, as long-term chemical stability of an either redox shuttle or a posolyte depends on its charged form. The isolated charged form exhibits appreciable stability over the period of experiment time (at 10 mM in anhydrous DCM over 5 h). Thus, the charged form is further evaluated as a chemical oxidant to be applied in synthetic and analytical chemistry applications.

Chapter 5 extends the discussion into chemical stability of charged forms (radical cations) of organic posolytes in different chemical environments. The stability of the charged forms of redox active species suffers at more extreme redox potentials due to either self-discharge in electrolyte solutions or molecular degradation in their charged forms, presenting a challenge in achieving high cell voltages. This study explores the change of chemical stability and cycling stability of organic posolytes by considering variably functionalized electron donating redox active organic molecules (e.g. phenothiazine, triphenylamine, carbazole, dialkoxybenzene, and cyclopropenium) with different oxidation potentials. The chemical stability of charged form was analyzed using UV-vis spectroscopy on isolated radical cation salts of organic posolytes. Their electrochemical stability was evaluated via charge-discharge experiments using bulk electrolysis.

CHAPTER 2. PERMENANTLY CHARGED ORGANIC ACTIVE MATERIALS FOR SUPPORTING-SALT-FREE NONAQUEOUS REDOX FLOW BATTERIES

This chapter is partially reproduced from "Dual Function Organic Active Materials for Nonaqueous Redox Flow Batteries" by **N. Harsha Attanayake**, Zhiming Liang, Yilin Wang, Aman Preet Kaur, Sean R. Parkin, Justin K. Mobley, Randy H. Ewoldt, James Landon, and Susan A. Odom, which was submitted to Materials Advances, September 3, 2020.

2.1   Summary

Nonaqueous electrolytes require the inclusion of supporting salts to achieve sufficient conductivity for battery applications. In redox flow batteries (RFBs) wherein solutions contain active species at molar values, the presence of supporting salts can reduce the solubility of organic active materials, limiting battery capacity. Here we sought to design materials in which permanently charged substituents keep ionic conductivity high while at the same time increasing the maximum concentration of the charge-storing redox moiety. Toward this goal, we synthesized redox-active phenothiazine and viologen derivatives bearing permanent charges. We employed these highly soluble materials as RFB electrolytes without adding supporting salts. Using an anion-selective membrane, a flow cell containing 0.25 M active species cycled stably over 100 cycles (433 h), losing an average of only 0.14% capacity per cycle and 0.75% per day, with post-cycling analysis showing no evidence of decomposition. These results show a new avenue to improve two performance aspects with one molecular modification.

2.2   Introduction

Redox Flow batteries (RFBs) containing nonaqueous solvents, the inclusion of supporting salts plays a critical role wherein polar aprotic solvents are used to dissolve the active materials that store energy in the solution phase. In general, organic solvents have low ionic conductivities compared to the electrolytes employed in RFBs. For instance, the ionic conductivities of acetonitrile (ACN) and propylene carbonate (PC) are 6×10^{-7} mS

cm^{-1} and 1×10^{-5} mS cm^{-1}, respectively,[1] whereas typical RFB supporting electrolytes have ionic conductivities ranging from approximately 3-60 mS cm^{-1} for nonaqueous and from 80-400 mScm^{-1} for aqueous systems.[1,2] Thus, RFBs based on nonaqueous electrolytes require supporting salts for sufficiently high ionic conductivity. Furthermore, supporting salts are required to balance electroneutrality while charging and discharging the cell. However, high supporting salt concentrations may suppress the solubility of the active species in one or more states of charge, reducing the volumetric capacity of the cell.[3-4] In addition, higher concentrations of supporting salt may limit the ionic conductivity of the membrane and increase area specific resistance (ASR), which prevent flow cells from operating at high current densities.[4-5] According to a recently proposed techno-economic model, future pricing for supporting salts in nonaqueous RFB electrolytes must reach a value of approximately \$5 kg^{-1} in order to reach the United States Department of Energy cost target (\$150 per kWh).[6-7] Therefore, developing multifunctional active species that serve as redox-active species as well as serving as the supporting salt in the RFB environment could eliminate the use of costly supporting salts. For this purpose, Milshtein et al. introduced metal-organic compounds containing common ions (tetrafluoroborates) to operate supporting-salt-free nonaqueous RFBs at low concentrations as a proof-of-concept demonstration.[8] In a common ion-exchange system, both redox-active species (posolyte and negolyte) contained positively charged groups, and common counter ions migrate between positive and negative sides of the cell through an ion-exchange membrane to maintain the electroneutrality of the cell. Inspired by this study, we sought to develop highly soluble, all-organic, common-ion-exchange active materials to be applied in nonaqueous RFBs in the absence of supporting salt.

Here we report the synthesis and characterization of two redox-active materials that simultaneously enhance solubility and ionic conductivity in the polar aprotic solvent ACN, as illustrated in Figure 2.1. In one case, we incorporated a branched ionic group in the alkyl substituent of a posolyte material. In the second, glycol chains at the N positions of the negative material. The phenothiazine core in EPRT-TFSI (ethylpromethazine bis(trifluoromethanesulfonyl)imide, Figure 2.1, red) is oxidized to its radical cation form (total species charge +2) during charging, while MEEV-TFSI$_2$ (Bis(2-(2-methoxyethoxy)ethyl)viologen bis(bis(trifluoromethanesulfonyl)imide), Figure 2.1, blue)

is reduced from a dication to its radical cation form (species charge +1); at the same time, the TFSI⁻ (green) migrates from the negolyte to the posolyte through an ion-exchange membrane. In both cases, the solubility and ionic conductivity of redox-active materials increased. Furthermore, both the active species and the counter ions contribute to the ionic conductivity in nonaqueous solvents. This dual property improvement allowed us to study all-organic, redox-active ionic species in a supporting-salt-free environment at high concentrations in full flow cell cycling experiments.
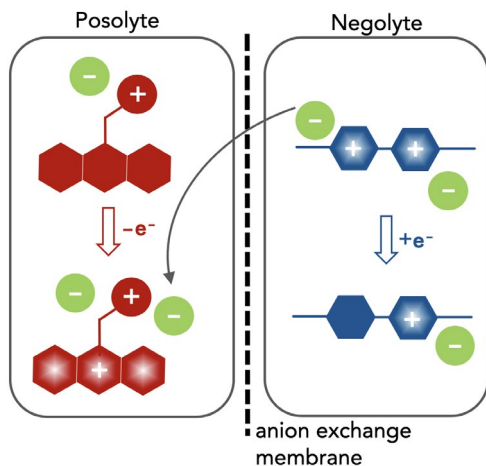
Figure 2.1. Schematic of the charging process in in redox flow cell containing dual-function active materials. During charging, the neutral conjugated core of the ionic phenothiazine (red) is oxidized to its radical cation form, and the dicationic viologen (blue) core is reduced to its radical cation form. Movement of one TFSI⁻ ion (green) from the negolyte solution to the posolyte solution serves to balance charge. Image created by Prof. Susan Odom.

2.3   Results and Discussion

2.3.1   Synthesis

EPRT-TFSI was prepared in three steps from commercially available materials. First, promethazine hydrochloride was treated with aqueous potassium carbonate to yield neutral promethazine (PRT, or 2-(N,N-dimethylamino)propylphenothiazine). An ethyl group was installed at the trialkylated N position of PRT to yield the ionic phenothiazine,

ethylpromethazine bromide (EPRT-Br). Finally, bromide was exchanged with the bis(trifluoromethanesulfonyl)imide (TFSI⁻) to yield ethylpromethazine bis(trifluoromethanesulfonyl)imide (EPRT-TFSI). Bis(2-(2-methoxyethoxy)ethyl)viologen bis(bis(trifluoromethanesulfonyl)imide) (MEEV-TFSI₂) was synthesized via the doulble alkylation of 4,4'-bipyridine and subsequent ion exchange of bromide with TFSI⁻. The reaction schemes for the synthesis of EPRT-TFSI and MEEV-TFSI₂ are shown in Figure 2.2. Also shown are the thermal ellipsoid plots from X-ray diffraction of single crystals of both products. Synthetic procedures and characterization details are reported in the Experimental section.
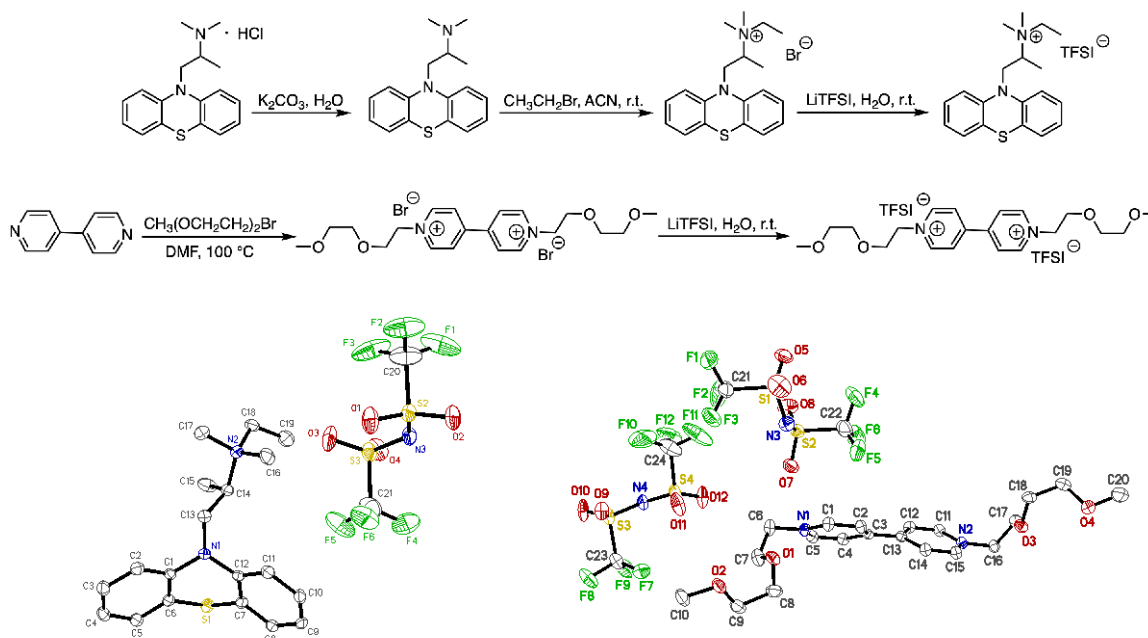
Figure 2.2. Synthesis of ethylpromethazine bis(trifluoromethanesulfonyl)imide (EPRT-TFSI) and bis(2-(2-methoxyethoxy)ethyl)viologen bis(bis(trifluoromethanesulfonyl)imide) (MEEV-TFSI₂). Thermal ellipsoid (50% probability) plots of EPRT-TFSI (bottom left) and MEEV-TFSI₂ (bottom right), obtained from single-crystal X-ray diffraction experiments. X-ray diffraction experiments performed by Dr. Sean R. Parkin.

2.3.2 Ionic Conductivity, Viscosity, and Diffusivity

To determine the viability of performing electrochemical analyses of EPRT-TFSI and MEEV-TFSI$_2$ in the absence of supporting electrolyte, the ionic conductivities of solutions containing 0.25, 0.50, 0.75, and 1.00 M in active materials were measured. For comparison, the ionic conductivity of the commercially available supporting salt tetraethylammonium bis(trifluoromethanesulfonyl)imide (TEATFSI) – selected because of the common TFSI anion and also containing a nitrogen-based cation – was measured at the same concentrations. Further, because ionic conductivity depends on the ionic strength, viscosity, and diffusivity of an active species, the viscosity and diffusivity of the active species were measured at these concentrations. Figure 2.3 shows the ionic conductivity (Figure 2.3a), viscosity (Figure 2.3b), and diffusivity (Figure 2.3c) in ACN for each electrolyte solution as a function of concentration, with a summary of data provided in Table 2.1.
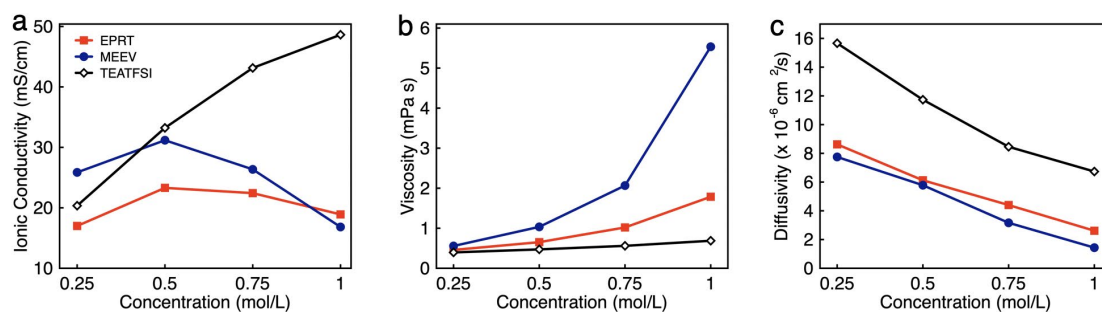
Figure 2.3. The ionic conductivity (a), viscosity (b), and diffusivity (c) of EPRT-TFSI, MEEV-TFSI$_2$, and TEATFSI at 0.25, 0.50, 0.75, and 1.00 M in ACN. The uncertainties associated with measurements are reported in the Table 2.1, as the uncertainty bars are smaller than the symbol size on the graphs. Viscosity experiments performed by Yilin Wang and diffusivity experiments performed by Dr. Justin K. Mobley.

Table 2.1. Ionic conductivity, viscosity, and diffusivity (cationic species) at 0.25, 0.50, 0.75, and 1.00 M of EPRT-TFSI, MEEV-TFSI$_2$, and TEATFSI in ACN. Viscosity experiments performed by Yilin Wang and diffusivity experiments performed by Dr. Justin K. Mobley.

Solution	Concentration (M)	Conductivity (mS cm^{-1})	Viscosity (mPa s)	Diffusivity (x 10^{-6} cm^2 s^{-1})
ACN	N/A	6 x 10^{-10} [a]	0.34 [a]	N/A
EPRT-TFSI in ACN	0.25	17.00±0.18	0.458±0.04	8.62
	0.50	23.30±0.12	0.652±0.008	6.12
	0.75	22.43±0.12	1.02±0.02	4.40
	1.00	18.91±0.21	1.78±0.01	2.62
MEEV-TFSI$_2$ in ACN	0.25	25.86±0.09	0.556±0.003	7.75
	0.50	31.18±0.32	1.03±0.01	5.78
	0.75	26.36±0.06	2.07±0.04	3.16
	1.00	16.83±0.12	5.53±0.03	1.43
TEATFSI in ACN	0.25	20.35±0.15	0.396±0.002	15.6
	0.50	33.22±0.39	0.472±0.001	11.7
	0.75	43.14±0.13	0.560±0.030	8.46
	1.00	48.63±0.42	0.687±0.040	6.73

(a) The diffusivity of cationic, EPRT$^+$, MEEV^{2+}, and TEA$^+$ were measured in CD$_3$CN. (b) Ref. (1).

Ionic conductivity measurements were carried out on EPRT-TFSI, MEEV-TFSI$_2$, and TEATFSI at 0.25, 0.50, 0.75, and 1.00 M in ACN at 25 °C using an Orian Star A212 conductivity meter (Thermo Scientific). (See Section 2.3.3 of the Experimental part for details.) At 0.25 M, MEEV-TFSI$_2$ exhibited the highest ionic conductivity, presumably due to the higher ionic strength of the divalent cation in MEEV-TFSI$_2$ compared to EPRT-TFSI and TEATFSI, which are both monovalent. The conductivity of MEEV-TFSI$_2$ is greater than the conductivity of EPRT-TFSI at all the concentrations except at 1 M. For both species, the maximum conductivity occurred at 0.5 M. For TEATFSI, the ionic

conductivity increased from 0.25 M to 1.00 M, with a more gradual increase at higher concentrations. We suspected that the trend results from the difference of cation size – with TEA being the smallest – and that the conductivities of EPRT-TFSI and MEEV-TFSI$_2$ decreased > 0.5 M due to decreased species diffusivity resulting from increased solution viscosity. To test this hypothesis, we proceed with measuring viscosities and diffusion coefficients.

The dynamic viscosities of electrolyte solutions (in ACN) were measured at 25 °C using a microfluidic pressure-driven flow viscometer (m-VROC, RheoSense, Inc.).[14-15] Each fluid sample was pushed through a microfluidic channel at a known volume flow rate, and viscosity was determined from the generated steady-state pressure drop resulting from the flow resistance. (See further details in Section 2.3.4 of the Experimental.) The viscosities of all three ionic electrolytes at 0.25 M in ACN are slightly higher than the viscosity of pure ACN (0.34 mPa·s). Viscosities increased proportional to molecular volume (and hydrodynamic radius), with MEEV-TFSI$_2$ > EPRT-TFSI > TEATFSI. Viscosity increased monotonically and non-linearly as a function of concentration for all systems. The initial linear increase (c < 0.50 M) is typically proportional to the molecule's hydrodynamic volume.[16] However, from moderate to high concentrations (0.50 M to 1.00 M), the viscosity of MEEV-TFSI$_2$ and EPRT-TFSI increased rapidly and non-linearly compared to the viscosity of TEATFSI, which implies stronger solute-solute interactions in these systems, e.g. which may lead to the formation of ion pairs or other structures at non-dilute concentrations. The local maximum in conductivity corresponds to the strong increase in viscosity, i.e. second-order non-dilute interactions and non-linear increase of the viscosity measurements. function of concentration, for all concentrations, due to viscosity increase even in the dilute limit.

In addition to the dynamic viscosity at four different concentrations, dynamic viscosity of EPRT-TFSI and MEEV-TFSI$_2$ was measured as a function of the applied shear rate (5,000 – 30,000 s^{-1}) to determine whether the electrolytes exhibit Newtonian behavior. As shown in Figure 2.4, both 1 M EPRT-TFSI and MEEV-TFSI$_2$ do not exhibit considerable shear thickening or shear thinning, even at the highest shear rate probed. This result confirms that EPRT-TFSI and MEEV-TFSI$_2$ demonstrate Newtonian constant viscosity (less than 10% variation) for this range of shear rates. This result shows that viscosity is primarily a

function of concentration, not shear rate, and therefore the fluidity of the electrolytes should not be affected by the flow rate when materials cycle in a flow cell. While decreased conductivity occurs due to non-linear viscosity increase at high concentrations, the diffusivity is expected to decrease as a function of concentration, for all concentrations, due to viscosity increase even in the dilute limit.
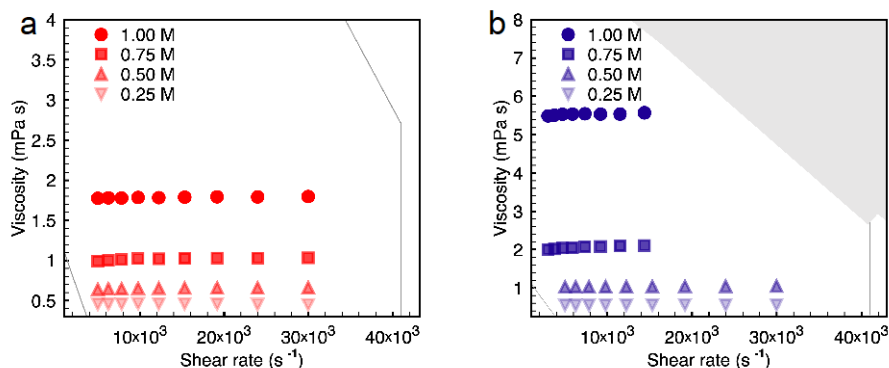
Figure 2.4. Dynamic viscosity as a function of shear rate at 0.25, 0.50, 0.75, and 1 M for EPRT-TFSI (a), MEEV-TFSI2 (b) in acetonitrile. The gray area represents the experimental limits, which comes from the maximum and minimum pressure drops the sensor can measure, and the maximum flow rate. Viscosity experiments performed by Yilin Wang.

The diffusion coefficient (or diffusivity) reflects the mobility of the ionic species. In general, diffusivity decreases with molecular size due to the larger solvated radius associated with larger molecular size.[17] However, the viscosity of the medium greatly affects the diffusivity as described in the Stokes-Einstein equation.[16] Thus, diffusion coefficients of positive counterparts of all three ionic species (EPRT$^+$, MEEV^{2+}, and TEA$^+$) were determined by a pulse gradient NMR method. EPRT-TFSI, MEEV-TFSI$_2$, and TEATFSI samples were prepared in CD$_3$CN for NMR analysis. Spectra from samples of varying concentrations were collected at 25 °C on a 500 MHz JEOL ECZr spectrometer equipped with a Royal Probe. The spectra were collected by arraying the pulse gradient. Using the JEOL Delta Software, a representative peak in the ^{1}H NMR spectrum of each sample was selected, and the diffusion coefficient was determined using diffusion analysis as the fitting algorithm. (See Section 2.3.5 of the Experimental.) As shown in Figure 2.3c, the diffusivity of ionic electrolytes varies according to the size of the molecule (TEATFSI > EPRT-TFSI > MEEV-TFSI$_2$). In addition, the diffusivity of ionic electrolytes decreases

with concentration due to the monotonic increase of viscosity as a function of concentration as we expected. Overall, EPRT-TFSI and MEEV-TFSI$_2$ were the most conductive (23.30 and 31.18 mS cm^{-1}, respectively) at 0.5 M, with values comparable to the commercially available electrolyte TEATFSI (33.22 mS cm^{-1}) at the same concentration. Finally, this conductivity analysis revealed that newly developed ionic-organic electrolytes are promising for implementation in RFBs without requiring supporting salts.

2.3.3 Cyclic voltammetry

Cyclic voltammetry (CV) was used to investigate electrochemical properties, including redox potentials, kinetics, and chemical reversibility, and to measure diffusion coefficients associated with EPRT-TFSI and MEEV-TFSI$_2$ in the presence and absence of supporting salt, allowing us to determine whether active species maintain their redox activity without a supporting salt. 100% iR correction was applied to compensate for solution resistance before performing each CV analysis. Figure 2.5 shows cyclic voltammograms of individual active species (red and blue) and as an equimolar mixture of each (black) at 10 mM, both in ACN only (solid lines) and in a 0.5 M TEATFSI / ACN solution (dashed lines). Corresponding values for half-wave potentials, peak-to-peak separations, peak-current ratios, and diffusion coefficients are reported in Table 2.2.
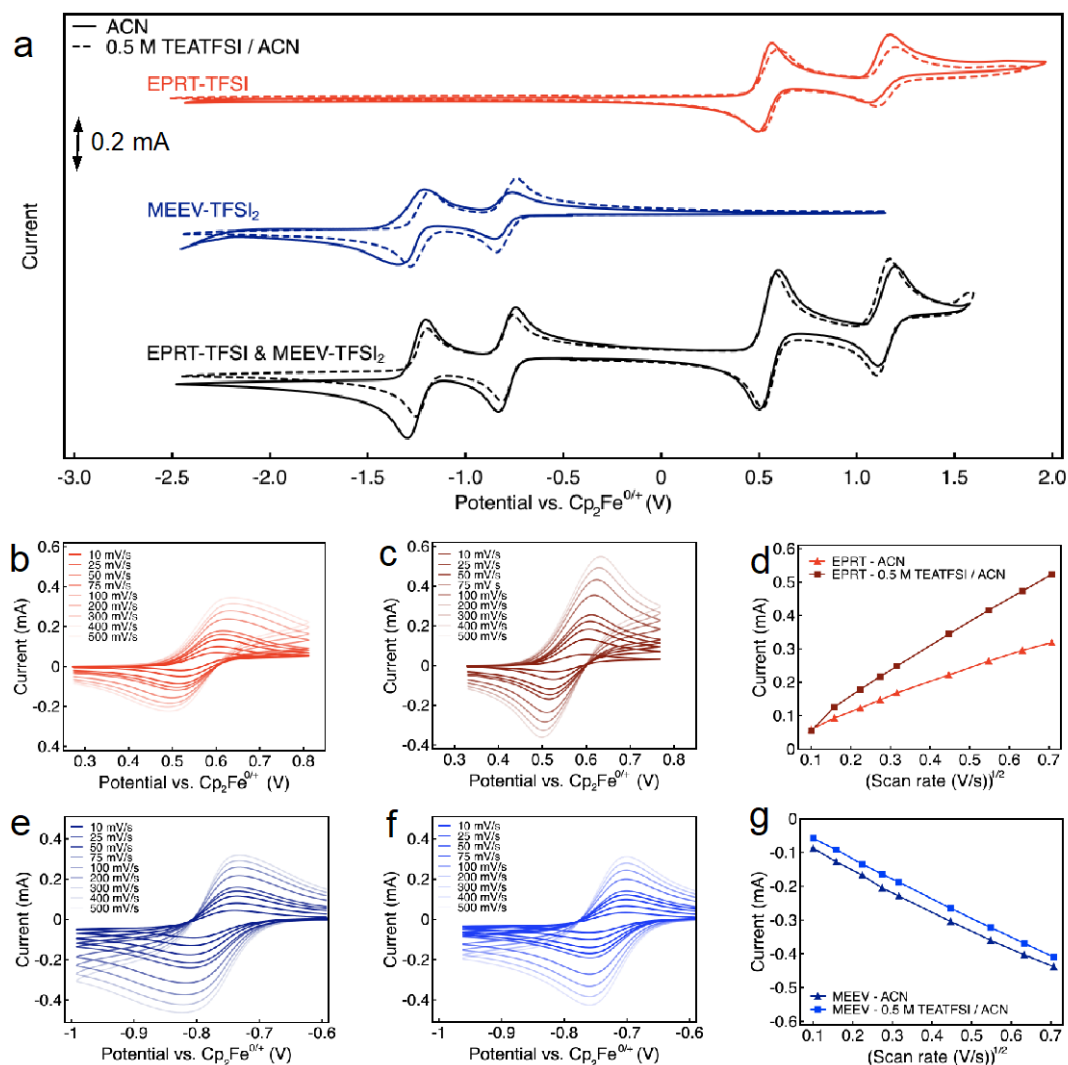
Figure 2.5. Cyclic voltammograms of ionic active species at 10 mM in ACN with no supporting salts and in ACN with 0.5 M TEATFSI. The full window of EPRT-TFSI and MEEV-TFSI$_2$, and an equimolar mixture of both EPRT-TFSI and MEEV-TFSI$_2$, respectively; CV experiments were performed at a scan rate of 100 mV s^{-1} (a). Scan rate-dependent CV study was done in both ACN and 0.5 M TEATFSI / ACN; EPRT-TFSI and MEEV-TFSI$_2$ in ACN (b,e), and in 0.5 M TEATFSI / ACN (c,f) at scan rates of 10, 25, 50, 75, 100, 200, 300, 400, and 500 mV s^{-1}. Additionally, corresponding Randles–Sevcik plots are shown for EPRT-TFSI (d) and MEEV-TFSI$_2$ (g). All cyclic voltammetry experiments were referenced to ferrocene/ferrocenium at 0 V. 100% iR correction was applied.

The first redox events of both EPRT-TFSI and MEEV-TFSI$_2$ are chemically (peak-current ratios of 1.03 and 1.02) and electrochemically (peak separations of 59 and 56 mV) reversible in 0.5 M TEATFSI / ACN. The active materials exhibited similar chemical reversibility (peak-current ratios of 1.04 and 1.10) in the absence of supporting salt.

Analysis of the peak-to-peak separations of EPRT-TFSI and MEEV-TFSI$_2$ with no supporting salt shows that their electro-kinetics are slightly slower (peak separations of 73 and 76 mV).

Table 2.2. Solubility, half-wave potentials, peak-current ratios and peak separations for the first and second redox events, and diffusion coefficients of EPRT-TFSI and MEEV-TFSI$_2$ at 10 mM in ACN and in 0.5 M TEATFSI / ACN. Except for diffusivity measurements, which were recorded at variable scan rates, data is reported from voltammograms recorded at a scan rate of 100 mV s^{-1} after applying 100% iR correction.

Solution	Solubility (M)	1st Redox Event			2nd Redox Event			Diffusivity (x 10^{-6} cm^2 s^{-1})
		E$_{1/2}$ vs. Cp$_2$Fe$^{0/+}$ (V)	Peak Current Ratio	Peak Separation (mV)	E$_{1/2}$ vs. Cp$_2$Fe$^{0/+}$ (V)	Peak Current Ratio	Peak Separation (mV)	
EPRT-TFSI in ACN	1.27	0.55	1.04	73	1.12	1.85	108	4.97
EPRT-TFSI in 0.5 M TEATFSI / ACN	1.11	0.55	1.03	59	1.12	1.20	96	15.3
MEEV-TFSI$_2$ in ACN	1.07	-0.79	1.10	76	-1.26	1.08	109	9.32
MEEV-TFSI$_2$ in 0.5 M TEATFSI / ACN	0.91	-0.79	1.02	56	-1.24	1.03	57	9.81

However, peak-to-peak separations of an equimolar mixture (10 mM each) of EPRT-TFSI and MEEV-TFSI$_2$ shows enhanced kinetics (peak separations of 66 and 57 mV), confirming that the previously observed, relatively larger peak-to-peak separations are not a result of sluggish kinetics but are instead due to lower solution conductivity for the active species at 10 mM in ACN (EPRT-TFSI: 1.21 mS cm^{-1} and MEEV-TFSI$_2$: 2.39

mS cm^{-1}). EPRT-TFSI shows only one fully reversible oxidation; two successive reduction events are observed for MEEV-TFSI$_2$. With a peak-current ratio of 1.85 and a peak-to-peak separation of 108 mV in ACN, the second oxidation of EPRT- TFSI is less chemically and electrochemically reversible than the first oxidation event. While not fully reversible, the reversibility improved in 0.5 M TEATFSI / ACN, with the second oxidation showing a peak-current ratio of 1.20 and a peak-to-peak separation of 96 mV. Overall, EPRT-TFSI showed a more reversible second oxidation in TEATFSI / ACN electrolyte system compared to the other N-substituted phenothiazines that we have reported so far in the same electrolyte; while further experimentation will need to be conducted for verification. Based on our previous CV results of an N-substituted phenothiazine in different electrolytes, we suspect that a higher concentration of TFSI$^-$ stabilizes the dication form of EPRT.[18-21] For MEEV-TFSI$_2$, in addition to a reversible first reduction, the second reduction is also chemically reversible in both the presence and absence of the supporting salt (peak current ratios of 1.08 and 1.03). Although the second reduction of MEEV-TFSI$_2$ is electrochemically reversible in 0.5 M TEATFSI / ACN (peak separation of 57 mV), it shows noticeably less electrochemical reversibility in the absence of the supporting salt (109 mV).

EPRT-TFSI and MEEV-TFSI$_2$ show similar redox potentials in 0.5 M TEATFSI / ACN and in ACN, with E$^{0/+}$ at 0.55 V versus Cp$_2$Fe$^{0/+}$ for EPRT-TFSI, and E$^{2+/+}$at -0.79 V and E$^{+/0}$ at -1.24 versus Cp$_2$Fe$^{0/+}$ for MEEV-TFSI$_2$ (Table 2.2, and Figure 2.5a). EPRT-TFSI exhibits a higher oxidation potential (0.55 V versus Cp$_2$Fe$^{0/+}$) than N-substituted phenothiazines with neutral substituents (e.g. EPT at 0.27 V and MEEPT at 0.31 V versus Cp$_2$Fe$^{0/+}$),[3] which is due to the stronger electron withdrawing character of the tetraalkylammonium substituent relative to alkyl and glycol groups.[22] Therefore, introducing a positively charged group at the N position of phenothiazine not only raises the conductivity but also the oxidation potential, which is desirable for achieving higher cell voltages. The position of the first oxidation of EPRT-TFSI and the first reduction of MEEV-TFSI$_2$ leads to a theoretical cell voltage of 1.34 V for a supporting-salt-free flow cell (Figure 2.5a). If the concentration of EPRT-TFSI were doubled the and MEEV-TFSI$_2$

were utilized as a two-electron-accepting material, a cell potential of 1.80 V could be achieved.

In addition to NMR studies, analysis of variable scan rate voltammograms (Figures 2.5b,c-2.5e,f) allows for an estimation of diffusion coefficients of the redox-active species in the presence and absence of supporting salt using Randles–Sevcik analysis[17] (Table 2.2, and Figures 2.5d, 2.5g). The diffusion coefficients measured with supporting salt show slightly higher diffusivity values (EPRT-TFSI: 15.3 x 10^{-6} cm^2 s^{-1} and MEEV-TFSI$_2$: 9.81 x 10^{-6} cm^2 s^{-1}) compared to those obtained without supporting salt (EPRT-TFSI: 4.97 x 10^{-6} cm^2 s^{-1} and MEEV-TFSI$_2$: 9.32 x 10^{-6} cm^2 s^{-1}), which may be due to the low ionic conductivity at 10 mM in active species. The diffusivity study further supports the slow kinetics observed in the absence of the supporting salt in CV conditions. EPRT-TFSI shows a higher diffusion coefficient than MEEV-TFSI$_2$ in 0.5 M TEATFSI / ACN, which agrees with the relative hydrodynamic radii of the molecules as previously discussed. Overall, the electrochemical analysis suggests that a supporting-salt-free flow cell containing EPRT-TFSI and MEEV-TFSI$_2$ is feasible.

2.3.4   Solubility

Achieving higher active material concentrations serves to increase the volumetric energy density. With that in mind, we determined the solubility of EPRT-TFSI and MEEV-TFSI$_2$ in ACN and in 0.5 M TEATFSI / ACN (Table 2.2). Both EPRT-TFSI and MEEV-TFSI$_2$ dissolved at > 1 M in ACN (EPRT-TFSI at 1.27 M and MEEV-TFSI$_2$ at 1.08 M), yet the solubility of both materials is significantly reduced (by 13% for EPRT-TFSI and 15% for MEEV-TFSI$_2$) in 0.5 M TEATFSI / ACN. This preliminary solubility analysis demonstrates that the concentration, and thus the volumetric capacity, of redox-active materials can be raised by removing supporting salts from the system.

2.3.5 Crossover
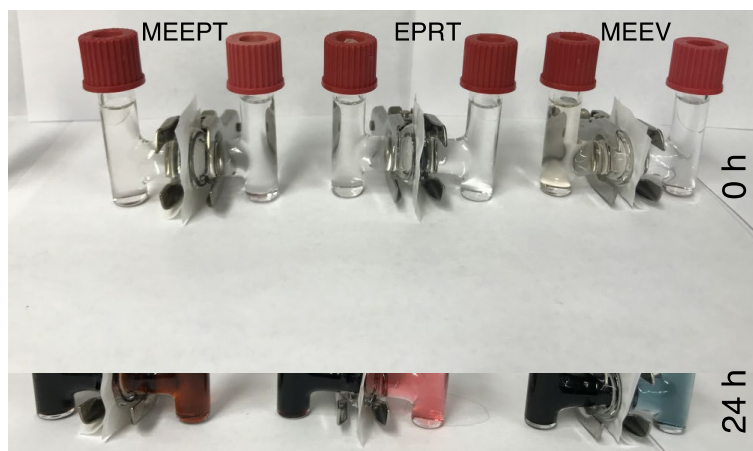
Figure 2.6. Photograph of crossover study with H cells with chambers separated by two layers of FAPQ-375-PP using MEEPT, EPRT-TFSI, and MEEV-TFSI$_2$ (from left to right) as active materials. The left side of the H cell contained 0.2 M active material in ACN, and the right side contained ACN at 0 h. The images were recorded at 0 (top row) and 24 h (bottom row). For 24 h reporting, NOBF$_4$ (for MEEPT and EPRT-TFSI) or Na metal (MEEV-TFSI$_2$) was added to the both side of each H cell, which generates colored solutions by either oxidizing (MEEPT and EPRT-TFSI) or reducing (MEEV-TFSI$_2$) each active materials.

Crossover tests were conducted with the aim of minimizing active materials crossover during cycling.[23] We evaluated crossover with the anion exchange membrane FAPQ-375-PP because the active materials both have a net charge of +1 or +2 in their relevant states of charge, giving preference for TFSI$^-$ migration over the active species. In addition to evaluating the crossover rates of EPRT-TFSI and MEEV-TFSI$_2$ N-(2-(2-methoxyethoxy)ethyl)phenothiazine (MEEPT), a non-ionic phenothiazine, was analyzed to determine whether the charged substituents mitigate crossover. Small-volume in-house glass-blown stationary H cells housed 0.2 M of active material in ACN (left side) and ACN (right side) separated by two layers of FAPQ-375-PP. Addition of a chemical oxidant (NOBF$_4$ for the MEEPT and EPRT-TFSI) or a reducing agent (sodium metal for the MEEV-TFSI$_2$) to both sides of the cell at 24 h was used to visualize the crossover (see photograph in Figures 2.6), wherein it is evident that the majority of all materials remains on the original side of the cell. For quantitative analysis, before adding the visualizing

reagents, crossover was measured by extracting aliquots of solution from each side of the H cell at 0, 1, 6, 12, and 24 h, then systematically diluting each sample and recording cyclic voltammograms (Figures 2.7b-d), the integration of which showed the relative ratios of material on each side of the cell. As expected, the results show that the rate of crossover decreased with higher net molecular weight with MEEPT < EPRT-TFSI < MEEV-TFSI$_2$, with 10.5, 4.1, and 2.1% of material having crossed over after 24 h, respectively (Figure 2.7a).
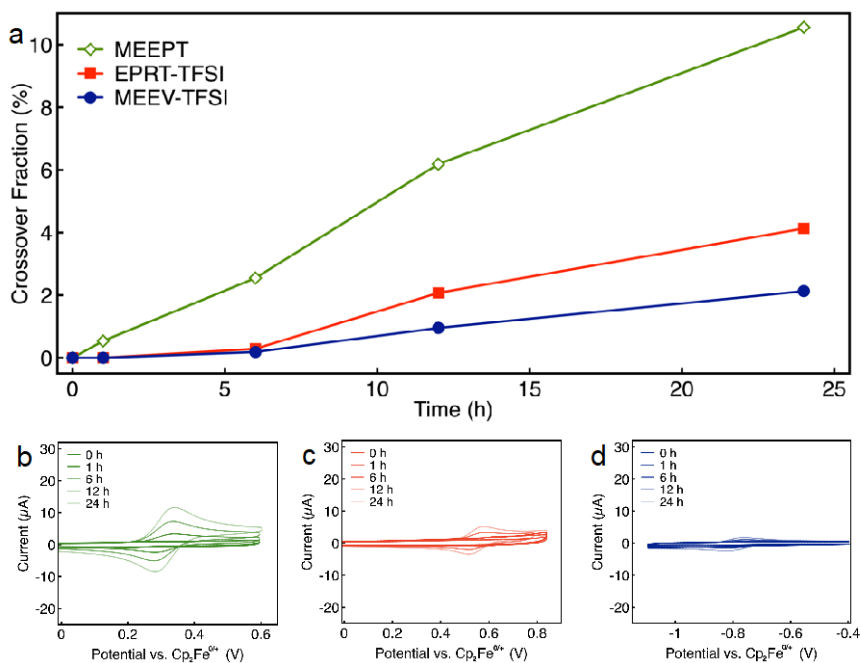
Figure 2.7. Comparison of crossover of MEEPT, EPRT-TFSI, and MEEV-TFSI$_2$ through two layers of FAPQ-375 PP. Fraction of crossover vs. time (a). Cyclic voltammograms of diluted aliquots taken from the right side of each H cell at 0, 1, 6, 12, and 24 h for MEEPT (b), EPRT-TFSI (c), and MEEV-TFSI$_2$ (d) in 0.1 M TEATFSI/ACN.

2.3.6   Flow Cell Cycling

In addition to limiting crossover, it is important that the pairing of the membrane and active materials does not lead to significant increases in ASR, which could result from chemical reactions with the membrane and/or pore blockage due to physisorption. Using a custom-built small-volume flow cell with interdigitated flow field,[24] ASR was measured using impedance spectroscopy, with cell resistance measured as the X intercept of the

Nyquist plots.[25] Comparing a cell assembled with 0.5 M active species (0.5 M EPRT-TFSI / ACN on the positive side and MEEV-TFSI$_2$ / ACN on the negative side) and to another containing 0.5 M TEATFSI / ACN (both sides), impedance analysis reveals that the EPRT-TFSI / MEEV-TFSI$_2$ / ACN system shows moderate cell resistance (20.1 Ω cm^2), similar to the TEATFSI / ACN cell (18.9 Ω cm^2) (Figure 2.8). This negligible difference may be due to differences in conductivity between the active materials and the commercial supporting salt and/or variability in the cell assembly. Importantly, the low ASR results indicate that EPRT-TFSI and MEEV-TFSI$_2$ can be cycled in a RFB using an anion exchange membrane at a high concentration without additional supporting salt.
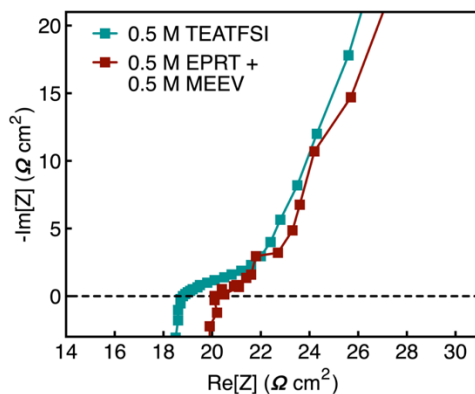
Figure 2.8. Nyquist plot of the flow cell with two stacked pieces of FAPQ-375-PP anion exchange membrane in electrolyte of 0.5 M EPRT-TFSI / ACN (positive side) and MEEV-TFSI$_2$ / ACN (negative side) and 0.5 M TEATFSI / ACN (both sides).

With ionic conductivities and electrochemical characteristics of EPRT-TFSI and MEEV-TFSI$_2$ showing promising characteristics for a supporting-salt-free nonaqueous RFB, we proceeded with further experiments to screen materials for flow cell cycling. To complete the variety of measurements including flow cell cycling at high concentrations, scalable syntheses are required. For this purpose, we scaled up the synthesis of EPRT-TFSI and MEEV-TFSI$_2$, performing reactions in batches as large as 20-40 grams. The products were purified via simple laboratory techniques such as filtration and crystallization, as reported in the Supporting Information, and did not require column chromatography.

Cycling stability is a critical factor in determining the lifetime of flow cells. The capacity losses in most RFBs are caused by either active species crossover through

membrane or separator,[26] disproportionation reactions of active molecules,[20, 27] or molecular decomposition.[28-29] However, losses due to species crossover can be restored to some extent by electrolyte remixing and hydraulic pressure regulation.[26, 30-31] We assembled two flow cells with active species concentrations of 0.5 M under two different configurations. First, 0.5 M of each active species was dissolved separately in ACN (positive side: 0.5 M EPRT-TFSI; negative side: 0.5 M MEEV-TFSI$_2$); in the second, both electrolytes contained equimolar amounts of the active species (both sides: 0.25 M EPRT-TFSI and 0.25 M MEEV-TFSI$_2$). Before conducting constant current cell cycling, we performed variable rate cycling to determine the appropriate current density in separated or mixed cells. The rate studies were performed at four different current densities (5, 10, 15, and 20 mA cm^{-2}) with five charge/discharge cycles at each current density. Then, five more cycles were recorded at the initial current density (5 mA cm^{-2}) to determine whether high current densities lead to capacity fade. The charge and discharge capacities are shown in Figures 2.9a, c (separated) and 2.9b, d (mixed) along with coulombic efficiencies. In both the separated and mixed cells, the accessed capacities decreased at higher current densities, consistent with greater cell polarization at higher current densities.[20]
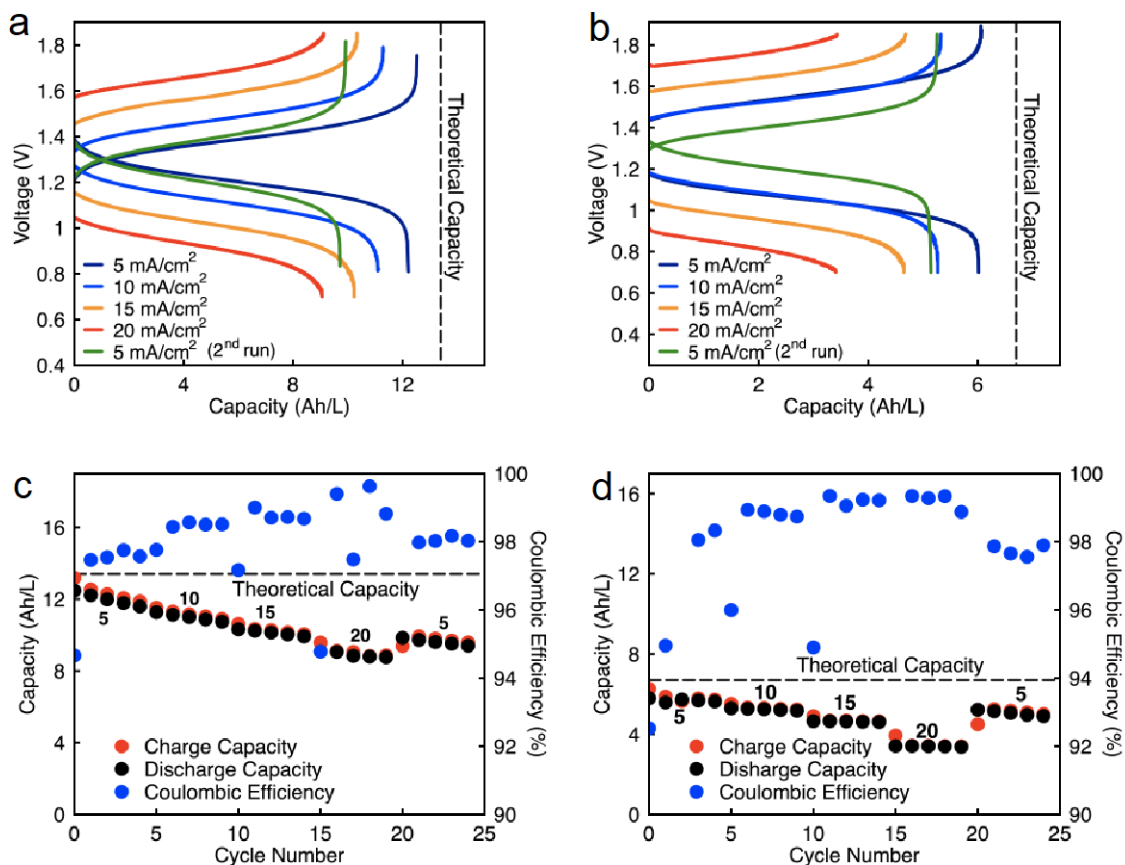
Figure 2.9. Rate study of EPRT-TFSI and MEEV-TFSI$_2$ in a separated or a mixed flow cell in ACN without supporting salt. Charge and discharge voltage vs. capacity for various current densities of 0.5 M active species in a separated flow cell (a), 0.25 M active species in a mixed flow cell (b). Potential curves are from the 2nd cycle at each current density. Capacity vs. cycle number for various current densities of 0.5 M active species in a separated flow cell (c), 0.25 M active species in a mixed flow cell (d). Potential cut-offs for each flow cell experiment were 1.85 to 0.70 V. The theoretical capacities for separated and mixed flow cells are 13.4 Ah L^{-1} (134 mAh) and 6.7 Ah L^{-1} (67 mAh), respectively. The total experiment runtimes for rate studies were 259 h (a, c) and 125 h (b, d). Rate studies performed by Dr. Zhiming Liang.

From the second cycle in the initial and final sets of 5 mA cm^{-2} cycling, 20% and 10% of capacity fade occurred in the separated and mixed cells, respectively; this loss might result from charged species crossover during the experiment (run time: 259 h for the separated electrolytes cell, 125 h for the mixed electrolytes cell). In addition, the rate studies (Figures 2.9a-d) indicate that the supporting-salt-free flow cell can operate even at current densities

36

of 20 mA cm^{-2} with > 50% of the theoretical capacity accessed in both cases (67% in the separated electrolytes cell, 51% in the mixed electrolytes cell).

Constant current flow cell cycling was conducted at 10 mA cm^{-2} to evaluate the long-term stability of active materials in a supporting-salt-free flow cell environment; 10 mA cm^{-2} was selected by balancing the fraction of capacity accessed with coulombic efficiencies and taking into account experimental run times. First, we tested active materials in a separated electrolytes flow cell at active materials concentration of 0.5 M. Figure 2.10c shows the charge capacities, discharge capacities, and coulombic efficiencies versus cycle number. Although we planned to run this cell for 100 cycles, due to complications resulting from a power outage, we stopped cell cycling after 74 cycles. Initially, 88% of theoretical capacity was accessed (11.89 Ah L^{-1}) in this cycling experiment. Over 74 cycles (605.5 h, 26 days), 42.83% of capacity fade was observed. The flow cell maintained 98.5-99.2% of coulombic efficiency (Figure 2.10c) with 71.1-75.2% of voltage efficiency and 70.1-74.7% energy efficiency (Figure 2.11a). After 74 cycles, we disassembled the cell and stored the posolyte and negolyte in glass vials in an argon-filled glove box. Post-cycling CV analysis was performed to determine whether the capacity fade was due to crossover and/or decomposition. The voltammograms of the cycled posolyte and negolyte are shown in Figure 2.10e. As evidenced by CV results, active species crossover was the cause of capacity fade. Importantly, no redox center decomposition was evident.

For the mixed electrolyte configuration, the cell was assembled with the same electrolyte on both sides of the cell (0.25 M EPRT-TFSI and 0.25 M MEEV-TFSI$_2$), cycling at rate of 10 mA cm^{-2}. Figure 2.10d shows charge and discharge capacities as well as coulombic efficiencies versus cycle number of the mixed electrolytes cell. At first, 91% of the theoretical capacity (6.01 Ah L^{-1}) was accessed. The capacity retention over 100 cycles (433 h, 19 days) was remarkable for a small molecule nonaqueous RFB (86.51%), with 99.87% capacity retention per cycle or 99.25% per day. Furthermore, the mixed electrolytes cell had coulombic efficiencies of 99.1-99.4% (Figure 2.10d), with voltage and energy efficiencies as 66.6-72.8% and 64.6-70.6% (Figure 2.11b), respectively.
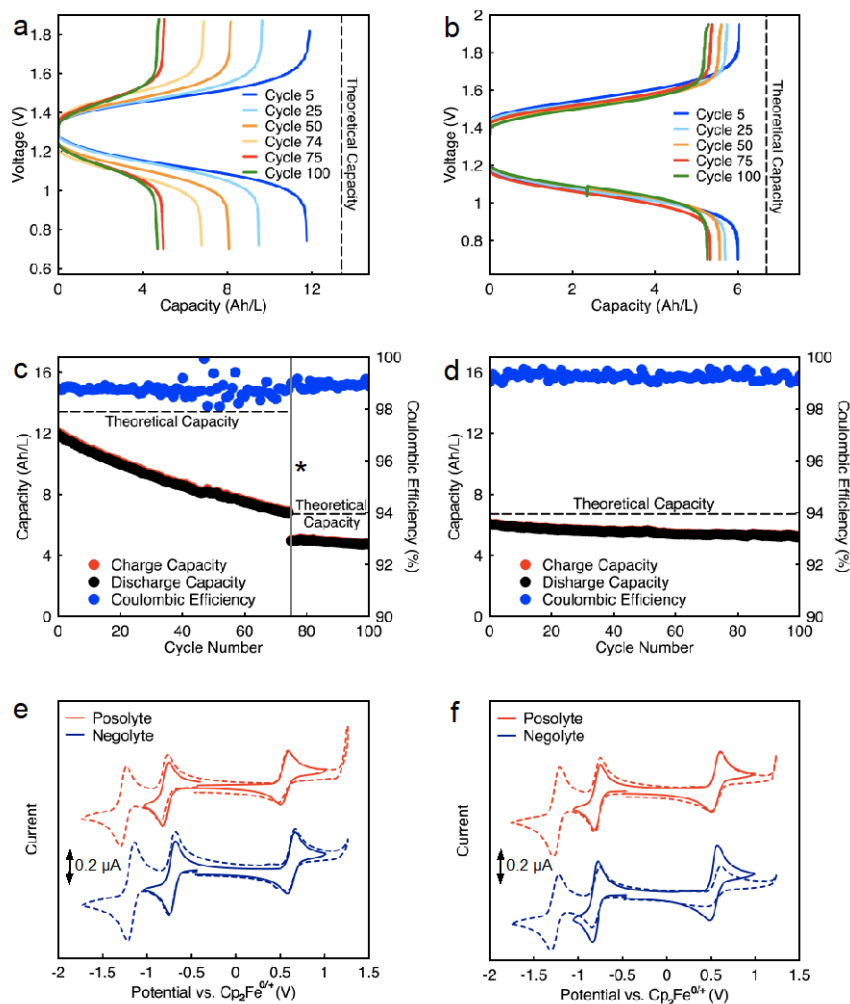
Figure 2.10. Constant current cycling of EPRT-TFSI and MEEV-TFSI$_2$ in a separated or a mixed flow cell in ACN with no supporting salts at 10 mA cm^{-2} current density. Charging and discharging voltage as a function of capacity of 0.5 M active species in a separated flow cell (a), 0.25 M active species in a mixed flow cell (b). Capacity vs. cycle number of 0.5 M active species in a separated flow cell (c), 0.25 M active species in a mixed flow cell (d). Potential cut-offs for each flow cell experiment were 1.85-0.70 V. The theoretical capacities for separated and premixed flow cells are 13.4 Ah L^{-1} (134 mAh) and 6.7 Ah L^{-1} (67 mAh), respectively. The total experiment runtimes for constant current cycling were 716 h (a, c), and 433 h (b, d). Cyclic voltammetry scans (100 mV s^{-1}) of the posolyte (red) and negolyte (blue) after constant current cycling of separated flow cell (e), or mixed flow cell (f) at approximately 10 mM in active material in ACN. Solid lines represent the first redox events while dashed lines represent the full window. 100% iR correction was applied. The asterisk (*) in plot "c" denotes that constant current cycling was stopped due to a power outage and restarted after two months. Flow cell cycling experiments performed by Dr. Zhiming Liang.

Post- cycling CV analysis (Figure 2.10f) supports that the capacity fade was not due to the active materials decomposition, as no new redox waves were observed. Therefore, it is likely that most of the capacity decay resulted from asymmetric charge species crossover rather than active species decomposition. Over the course of the experiment, the solution volumes in the two electrolyte reservoirs became more unequal, which supports our hypothesis that active species crossed over because of a concentration or pressure gradient.
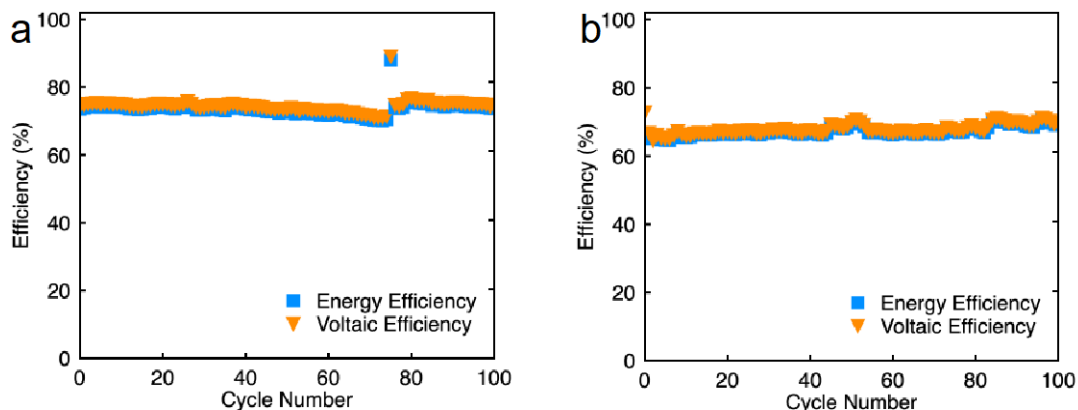
Figure 2.11. Voltaic and energy efficiencies vs. cycle number of EPRT-TFSI and MEEV-TFSI$_2$ in separated (0.50 M active species) (a) and premixed (0.25 M active species) (b) flow cell in acetonitrile with no supporting salts.

Since capacity retention increased upon pre-mixing electrolytes, we revisited the cycled electrolytes of the 0.5 M separated electrolyte cell that had stopped after 74 cycles. Two months after cycling had stopped, we mixed the solutions from both sides of the cell, divided the volume in half, putting them on each side of a flow cell with a new membrane stack. We then cycled the cell at the same current density (10 mA cm^{-2}). The cell cycling results are shown in the Figures 2.10a, c, starting from 75th cycle. The new cell showed a capacity of 4.95 Ah/L at the 75th cycle, which is 73% of the theoretical capacity of a 0.25 M mixed electrolytes cell. The lower accessed capacity might be due to active materials loss during flow cell disassembly after 74th cycle. Indeed, the increase in capacity retention (with 99.82% capacity retention per cycle) of new cell containing combined electrolytes from the originally separated electrolyte cell shows that the previous capacity fade resulted from both active species crossover and species imbalance.
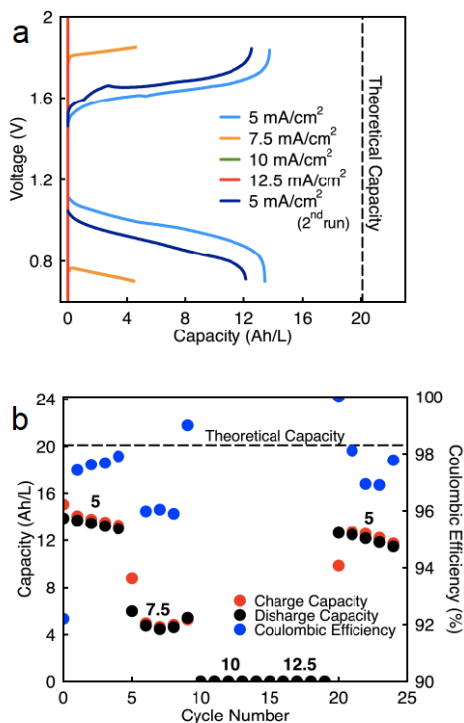
Figure 2.12. Rate study of EPRT-TFSI and MEEV-TFSI$_2$ in a premixed flow cell, showing voltage vs. capacity for various current densities (a). Potential curves are from the 2nd cycle at each current density. Capacity vs. cycle number for various current densities (b). Potential cut-off for flow cell experiment was 1.85 to 0.70 V. The theoretical capacity is 20.1 A h L^{-1} (201 mAh), and the experiment runtime was 230 h. Both sides of cell contained 0.75 M EPRT-TFSI and 0.75 M MEEV-TFSI$_2$ in ACN with no supporting salt.

Because we knew that we could not run a cell with separated electrolytes without losing capacity due to species crossover, for demonstration of cell cycling at higher concentrations of active materials, we chose to proceed with mixed electrolyte cells as membrane technology is not well developed yet to get the advantage of our highly stable new redox active species. Thus, we assembled a flow cell containing 0.75 M EPRT-TFSI and 0.75 M MEEV-TFSI$_2$ on both sides of the flow cell. We selected 0.75 M as the active species concentration since it is the highest achievable solubility after mixing an equimolar amount of EPRT-TFSI and MEEV-TFSI$_2$. As shown in Figures 2.12a-b, first, a rate study was performed to determine the appropriate current density for charge/discharge cycling. Due to the high viscosity of mixed electrolyte at near saturation condition, the flow cell cycling was done using one layer of FAPQ-375-PP membrane to minimize the cell resistance.
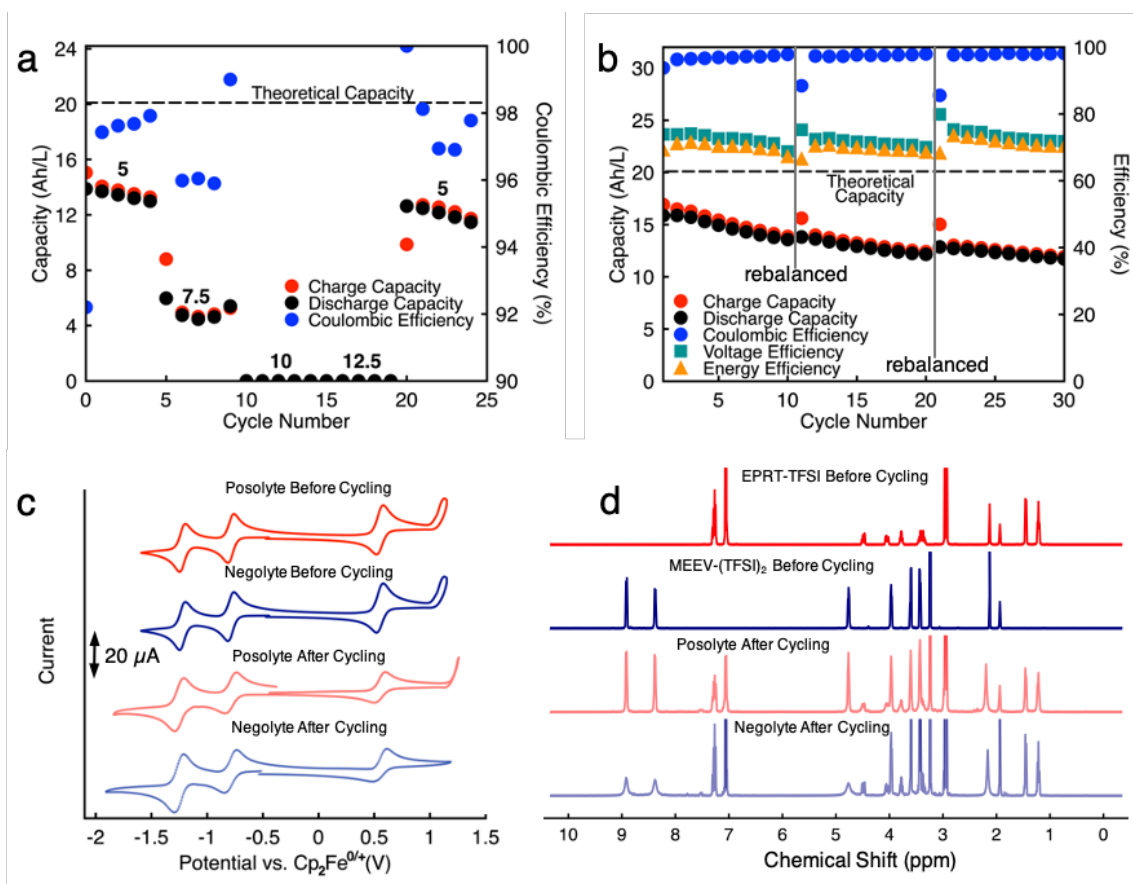
Figure 2.13. Rate study and constant current cycling of EPRT-TFSI and MEEV-TFSI₂ in a pre-mixed flow cell. Capacity vs. cycle number for various current densities (5, 7.5, 10, 12.5, and 5 mA cm^{-2}) of 0.75 M active species in a mixed flow cell (a), capacity vs. cycle number at 5 mA cm^{-2} current density of 0.75 M active species in a mixed flow cell. The potential cutoffs imposed during the flow cell experiment were 1.85 to 0.70 V. The theoretical capacity is 20.1 A h L^{-1} (201 mAh), and the total experimental runtime were 230 h (a) and 638.5 h (b). Both sides of cell contained 0.75 M EPRT-TFSI and 0.75 M BMEEV-TFSI₂ in ACN with no supporting salts. Constant current cycling (b) was stopped at cycle number 10 and 20, then rebalanced and restarted. Cyclic voltammetry scans (100 mV s^{-1}) of the posolyte (red) and negolyte (blue) before and after constant current cycling (c), at approximately 10 mM in active material in ACN. 100% iR correction was applied. ^{1}H NMR spectra of posolyte (red) and negolyte (blue) before and after constant current cycling (d).

As evidenced by the results of the variable rate study experiment (Figures 2.12a-b), the flow cell was only operated at low current densities due to the high cell resistance.

Based on the results of the variable rate study, constant current cycling was conducted at 5 mA cm^{-2} to evaluate long-term stability. Initially, the flow cell accessed 16.9 Ah L^{-1} capacity, which is 84% of the theoretical value (Figures 2.13a-b). A reduced capacity retention is observed, compared to the previously conducted 0.25 M mixed flow cell, which may have been caused by a higher rate of active species crossover due to using only one layer of FAPQ-375-PP membrane, high active species concentration, and longer charge-discharge time (~22 h per cycle). Therefore, the flow cell was rebalanced (stopped cycling, electrolytes removed from the flow cell and remixed, then reloaded) after every 10 cycles, aiming to recover the decayed capacity by rebalancing electrolytes. As we had hoped, the capacity increased after each rebalancing (Figure 2.13a, see cycles 11 and 21), but the capacity retention was continuously decreased which might be due to the steady crossover through charged-discharged species concentration gradient during the cycling. The lower coulombic efficiency (96 to 97%) further supports the active species crossover argument. In addition, 74 to 72% of voltage efficiency and 70 to 69% of energy efficiency (Figure 2.13b) are demonstrated at near saturation conditions.

To determine if active species had undergone chemical decomposition during high concentration, long term cycling (638.5 h, 27 days), we performed post cell cycling analyses on the cycled active species. As shown in Figure 2.13c, we recorded CVs of cycled electrolytes (posolyte and negolyte) and compared them with the freshly mixed electrolytes. The cycled solutions exhibited similar redox events as the initial solutions, supporting no redox center decomposition or redox center formation occurring during cycling. In addition to CVs, we acquired ^{1}H NMR of cycled electrolytes. Note that no precipitate was observed in flow fields or tanks. Before preparing samples for NMR analysis, a small portion of posolyte and negolyte was diluted with ACN determine if the contents were soluble; no solid remained in this test. An excess of sodium thiosulfate was added to electrolytes and then aerated to quench any radical species in the EPRT-TFSI and MEEV-TFSI$_2$, as they are paramagnetic and would convolute the NMR spectrum. The sodium thiosulfate was filtered, solvent (ACN) evaporated, and the remnants re-dissolved in CD$_3$CN for ^{1}H NMR analysis. Figure 2.13d shows ^{1}H NMR spectra of fresh EPRT-TFSI, MEEV-TFSI$_2$, cycled posolyte, and cycled negolyte. A comparison of cycled electrolytes with fresh electrolytes reveal that active materials did not undergo appreciable

decomposition during flow cell cycling. The ^{1}H NMR of cycled solutions show peak broadening in some peaks, which may be due to the presence of trace amounts of radicals in the sample. However, the post cell cycling analysis further supports that active species are indeed chemically stable and that observed capacity decay is not a result of the active material decomposition, but rather is a result of asymmetric charged species crossover through the anion exchange membrane.
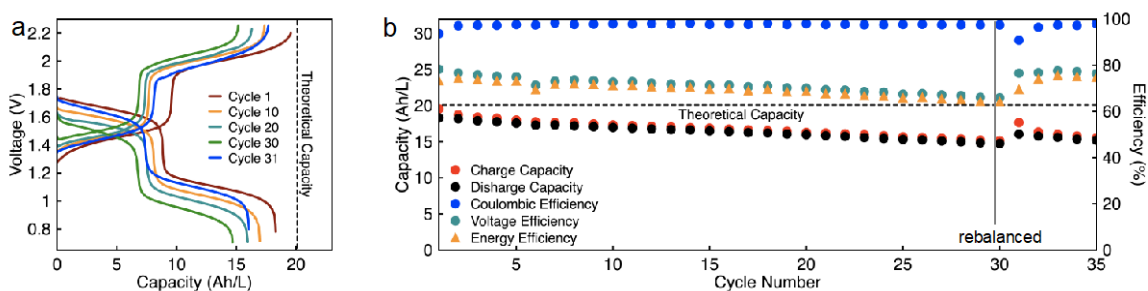
Figure 2.14. Constant current cycling of EPRT-TFSI and MEEV-TFSI$_2$ at 10 mA cm^{-2} in a mixed flow cell, charging and discharging voltage, as a function of capacity (a), capacity vs. cycle number (b). The potential cut-offs imposed during the flow cell experiment were 2.25 to 0.60 V. The theoretical capacity is 20.1 Ah L^{-1} (201 mAh), and the total experiment runtime was 454 h. Both sides of cell contain 0.750 M EPRT-TFSI and 0.375 M MEEV-TFSI$_2$ in ACN with no supporting salt.

While EPRT-TFSI is only capable of reversibly donating one electron in ACN, MEEV-TFSI$_2$ can reversibly accept two electrons, as shown Figure 2.5. Thus far, we demonstrated flow cell cycling only considering the first reversible redox event of MEEV-TFSI$_2$. However, accessing the reversible second reduction of MEEV-TFSI$_2$ during flow cell cycling would increase the theoretical cell voltage from 1.34 V to 1.80 V, which would increase the energy density by ca 34%. Besides that, less MEEV-TFSI$_2$ is necessary for flow cell cycling, which decreases the active material requirement and also lowers the viscosity of the electrolyte, potentially allowing the flow cell operation to cycle at relatively higher currents at high active species concentrations. As the EPRT-TFSI (one-electron) and MEEV-TFSI$_2$ (two-electron) combination offers notable benefits towards high concentration flow cell cycling, we assembled another premixed flow cell with 0.750 M EPRT-TFSI and 0.375 M MEEV-TFSI$_2$ on both sides of the cell. As expected, the flow cell demonstrated comparatively lower cell resistance, enabling cycling at a current density

43

of 10 mA cm^{-2}. The flow cell accessed 91% of the theoretical capacity, 18.3 Ah L^{-1}, which is the highest volumetric capacity reported for a nonaqueous RFB to date (Figures 2.14a-b). This two-electron cycling cell showed slightly improved capacity retention (81% of capacity retention over 30 cycles) compared to the 0.75 M one-electron cycling cell (74% of capacity retention), perhaps due to the lowered charge-discharge time (~13 h per cycle) and reduced rate of charged species crossover at lower concentration of MEEV-TFSI$_2$. In addition, the two-electron flow cell demonstrates 97% coulombic efficiency, 75-65% of voltage efficiency, and 73-64% of voltage efficiency over 30 cycles. Only 37.5% of discharged capacity returned form the decayed discharged capacity, after rebalancing the flow cell at 30th cycle, which further supports that capacity is mainly lost due to charged species crossover. Finally, the high volumetric capacity and raised cell voltage lead to an energy density of 10 to 12.5 Wh L^{-1}.

2.4   Conclusions

In this work we demonstrated stable, highly soluble, and ionically conductive redox-active organic molecules and their performance in a supporting-salt-free nonaqueous redox flow cell. We synthesized permanently charged redox-active materials to simultaneously enhance the solubility and ionic conductivity in acetonitrile via simple synthetic, scalable strategies. Although solutions of active species of at least 1 M could be prepared, these new materials exhibited the highest ionic conductivities 0.5 M in ACN, with a value on the same order of magnitude as the commercially available supporting electrolyte TEATFSI. The ionic conductivity dropped in ACN after 0.5 M due to the high viscosity (and low diffusivity) at near saturation points of these highly concentrated ionic active species. EPRT-TFSI and MEEV-TFSI$_2$ exhibited similar chemical and electrochemical reversibility with and without a supporting electrolyte, confirming the feasibility of operating these materials in a nonaqueous RFB in the absence of supporting salt. Preliminary flow cell cycling studies at moderate concentrations (0.5 M separated and 0.25 M mixed) demonstrated that active species crossover, not materials decomposition, is responsible for the loss of capacity with time. Thus, high concentration flow cell cycling was done in a mixed flow cell at 0.75 M active species concentration. But we found that the highest concentration achievable is not the best for performance because the increased

viscosity in highly concentrated solutions reduces the diffusion and ionic conductivity. Thus, aiming to minimize the solution viscosity and expand the cell voltage, we performed high concentration flow cell cycling utilizing the second reduction of MEEV-TFSI$_2$ and doubling the concentration of EPRT-TFSI to raise the energy density to unprecedented values. Future studies will focus on ways to modify electrolyte composition to lower viscosities at high concentrations, as well as cells that access the second oxidation of ionic phenothiazine derivative, resulting in a higher cell voltage. Still, the crossover of active species limits the volumetric capacity to half of its value, meaning suitable membranes need to be made available to prevent crossover of these permanently charged organic species. Progress in this area could double battery capacity.

2.5   Experimental

2.5.1   Synthesis

Materials

Promethazine hydrochloride (98%) was purchased from Tokyo Chemical Incorporated. Bromoethane ($\geq$ 99%), 4,4'-bipyridyl (anhydrous, 98%, stored in an argon filled glovebox), 1-bromo-2-(2-methoxyethoxy)ethane ($\geq$ 90%), and lithium bis(trifluoromethylsulfonyl)imide ($\geq$ 99%, stored in an argon filled glovebox) were purchased from Acros Organics. Acetonitrile (ACN, $\geq$ 99.9%) was purchased from J.T. Barker. *N,N* dimethylformamide (DMF, $\geq$ 99.9%), diethyl ether (anhydrous, $\geq$ 99%), and acetone ($\geq$ 99%), were purchased from VWR. ACN and DMF were stored in a solvent purification system (L.T. Technologies). Tetraethylammonium bis(trifluoromethane) sulfonamide (TEATFSI, > 99%, stored in an argon filled glovebox) was purchased from IoLiTec. Conductivity standards were purchased from Oakton (1.413, 12.9, and 80 mS cm^{-1}) and RICCA (25 and 47.6 mS cm^{-1}). FAPQ 375-PP anion exchange membrane (75 µm) was purchased from FumaTech. ^{1}H, ^{19}F, and ^{13}C NMR spectra were obtained on 400 MHz Bruker Avance NEO (equipped with a Smart Probe) in DMSO-d$_6$ from Cambridge Isotope Laboratories. For ^{19}F NMR, chemical shifts are reported vs. CFCl$_3$ at 0 ppm by adjusting the chemical shift of internal reference hexafluorobenzene to -164.9 ppm. ESI mass spectra

were obtained on a Thermo Finnigan LTQ ion trap mass spectrometer. Mass spectra were recorded in positive-ion mode. Elemental analysis was performed by Atlantic Microlab, Inc. Solubility tests, cyclic voltammetry measurements, and flow cell tests were performed in an argon-filled glovebox (MBraun, O_2 < 5 ppm, H_2O < 0.1 ppm).

Promethazine (PRT) was extracted from promethazine hydrochloride as previously reported.[9]

Ethylpromethazine bromide (EPRT-Br). To an oven-dried 500 mL round-bottomed flask containing a stir bar cooled under nitrogen atmosphere, promethazine (28.00 g, 0.0984 mol) was dissolved in anhydrous ACN (250 mL), creating a colorless solution. Then, bromoethane (11.1 mL 0.148 mol) was added to the reaction mixture and stirred for 24 h at room temperature during which a white solid was formed. The reaction flask was immersed in an ice bath to completely precipitate the product. Then, product was filtered and washed with diethyl ether to remove unreacted starting materials. Finally, the product, a white solid, was dried in a vacuum oven at 50 °C and -100 kPa (24.6 g, 64%). ^{1}H NMR (400 MHz, DMSO-d$_6$) δ 7.39 – 7.14 (m, 6H), 7.04 (td, J = 7.4, 1.4 Hz, 2H), 4.64 (dd, J = 14.6, 4.2 Hz, 1H), 4.08 (dd, J = 14.5, 8.6 Hz, 1H), 3.71 (ddt, J = 13.2, 10.8, 6.4 Hz, 1H), 3.59 – 3.37 (m, 2H), 3.04 (d, J = 7.6 Hz, 6H), 1.37 (d, J = 6.5 Hz, 3H), 1.21 (t, J = 7.1 Hz, 3H). ^{13}C NMR (100 MHz, DMSO-d$_6$) δ 143.7, 127.3, 127.1, 124.8, 122.9, 116.1, 64.5, 57.1, 46.9, 46.5, 45.3, 11.6, 7.3. ESI-MS: m/z 313 (100%), 314 (22%), 315 (4%). Anal. Calcd. for $C_{19}H_{25}BrN_2S$ C, 58.01; H, 6.41; N, 7.12; Br, 20.31. Found C, 58.13; H, 6.37; N, 7.12; Br, 20.29.

Ethylpromethazine bis(trifluoromethanesulfonyl)imide (EPRT-TFSI). In an oven-dried 1 L round-bottomed flask containing a stir bar cooled under nitrogen atmosphere, EPRT-Br (15.00 g, 0.0381 mol) was dissolved in deionized (DI) water (300 mL), creating a colorless solution. Then, in an Erlenmeyer flask, LiTFSI (13.2 g, 0.046 mol) was dissolved in DI water (100 mL), and this solution was slowly added to the round-bottomed flask over a period of about 10 min, resulting in a milky solution. The reaction mixture was stirred for 3 h, at room temperature and the product precipitated upon completion of the

reaction. The precipitated white solid was filtered and washed with DI water to remove unreacted starting materials. Finally, the isolated solid product (21.5 g, 95%) was dried in a vacuum oven at 50 °C and -100 kPa. To grow crystals of this product, a saturated solution of EPRT-TFSI in DCM was prepared in a glass vial fitted with a rubber septum. Then, the solvent was allowed to evaporate slowly under nitrogen after inserting a vent needle, and crystals formed at the bottom of glass vial. ^{1}H NMR (400 MHz, DMSO-d_6) δ 7.41 – 7.13 (m, 6H), 7.04 (t, J = 7.4 Hz, 2H), 4.63 (dd, J = 14.6, 4.2 Hz, 1H), 4.09 (dd, J = 14.6, 8.5 Hz, 1H), 3.85 – 3.60 (m, 1H), 3.60 – 3.37 (m, 2H), 3.04 (d, J = 6.9 Hz, 6H), 1.38 (d, J = 6.4 Hz, 3H), 1.21 (t, J = 7.1 Hz, 3H). ^{13}C NMR (100 MHz, DMSO-d_6) δ 143.2, 126.8, 126.5, 124.3, 122.4, 118.3 (q, J = 321.9 Hz), 115.6, 64.1, 56.6, 46.4, 45.9, 44.7, 11.1, 6.7. ^{19}F NMR (400 MHz, DMSO-d_6) δ -75.6 (vs. hexafluorobenzene). ESI-MS: m/z 313 (100%), 314 (22%), 315 (4%). Anal. Calcd. for $C_{21}H_{25}F_6N_3O_4S_3$ C, 42.29; H, 4.25; N, 7.08; F, 19.2. Found C, 42.54; H, 4.14; N, 7.07; F, 19.04.

Bis((2-(2 methoxyethoxy)ethyl))viologen bromide (MEEV-Br$_2$). To an oven-dried 1 L round-bottomed flask containing a stir bar cooled under a nitrogen atmosphere, 4,4-bipyridyl (20.00 g, 0.1284 mol) and anhydrous DMF (600 mL) were added, creating a yellow/orange solution. Then 1-bromo-2-(2-methoxyethoxy)ethane (51.7 mL 0.384 mol) was added at room temperature after which the reaction flask was immersed in an oil bath set at 100 °C and stirred for 24 h during which time a yellow precipitate formed. The reaction flask was removed from the oil bath and the reaction mixture was allowed to cool to room temperature. Then the resulting yellow solid was filtered under a blanket of nitrogen and was washed with isopropanol, acetone, and diethyl ether to remove unreacted starting materials. Finally, the product, a yellow solid, was dried in a vacuum oven at 50 °C and -100 kPa (41.5 g, 62%). ^{1}H NMR (400 MHz, DMSO-d_6) δ 9.31 (d, J = 6.4 Hz, 4H), 8.79 (d, J = 6.4 Hz, 4H), 4.88 (t, J = 4.8 Hz, 4H), 3.98 (t, J = 4.8 Hz, 4H), 3.58 (t, J = 4.2 Hz, 4H), 3.38 (t, J = 4.2 Hz, 4H), 3.17 (s, 6H). ^{13}C NMR (100 MHz, DMSO-d_6) δ 148.2, 145.6, 125.7, 70.4, 68.8, 68.0, 59.8, 57.5. ESI-MS: m/z 362 (100%), 363 (22%), 360 (14%). Anal. Calcd. for $C_{20}H_{30}Br_2N_2O_4$ C, 45.99; H, 5.79; N, 5.36; Br, 30.60. Found C, 44.87; H, 5.52; N, 5.48; Br, 30.86.

Bis((2-(2-methoxyethoxy)ethyl))viologen **bis(trifluoromethanesulfonyl)imide** **(MEEV-TFSI$_2$).** In a 1 L round-bottomed flask, MEEV-Br$_2$ (40.00 g, 0.07664 mol) was dissolved in DI water (600 mL), creating a pale orange solution. In another 250 mL round-bottomed flask, LiTFSI (49.5 g, 0.172 mol) was dissolved in DI water (100 mL), and the resultant solution was added to the flask containing MEEV-Br$_2$ over a period of about 10 min, resulting in a pale pink solution. The reaction mixture was stirred at room temperature for 3 h during which a precipitate formed. The pale pink precipitate was filtered and washed with water to remove unreacted starting materials. Finally, the solid product was dried in a vacuum oven at 50 °C and -100 kPa, yielding a pale pink solid (42.5 g, 60%). To obtain crystals of this product, the isolated solid was crystalized from water in the presence of charcoal yielding the product as white crystalline needles. ^{1}H NMR (400 MHz, DMSO-d$_6$) δ 9.30 (d, J = 6.6 Hz, 4H), 8.78 (d, J = 6.6 Hz, 4H), 4.88 (t, J = 5.0 Hz, 4H), 3.97 (t, J = 5.0 Hz, 4H), 3.57 (t, J = 4.4 Hz, 4H), 3.38 (t, J = 4.4 Hz, 4H), 3.17 (s, 6H). ^{13}C NMR (100 MHz, DMSO-d$_6$) δ 148.5, 145.7, 125.8, 119.6 (q, J = 321.9 Hz), 70.5, 69.1, 68.1, 60.1, 57.5. ^{19}F NMR (400 MHz, DMSO-d$_6$) δ -78.8 (vs. hexafluorobenzene). ESI-MS: m/z 362 (100%), 363 (23%), 360 (13%). Anal. Calcd. for C$_{24}$H$_{30}$F$_{12}$N$_2$O$_{12}$S$_4$ C, 31.24; H, 3.28; N, 6.07; F, 24.71. Found C, 30.94; H, 3.07; N, 6.05; F, 24.42.

2.5.2   X-Ray Crystallography

X-ray diffraction data were collected at 90.0 K on a Bruker D8 Venture kappa-axis diffractometer using MoK(alpha) X-rays. Raw data were integrated, scaled, merged and corrected for Lorentz-polarization effects using the APEX3 package. Corrections for absorption were applied using SADABS.[10] The structure was solved by direct methods (SHELXT)[11] and refinement was carried out against F^2 by weighted full-matrix least-squares (SHELXL).[12] Hydrogen atoms were found in difference maps, but subsequently placed at calculated positions and refined using a riding model. Non-hydrogen atoms were refined with anisotropic displacement parameters. Atomic scattering factors were taken from the International Tables for Crystallography.[13]

2.5.3 Ionic Conductivity

Ionic conductivity measurements were carried out on EPRT-TFSI, MEEV-TFSI$_2$, and TEATFSI at 0.25, 0.50, 0.75, and 1.00 M in ACN. Measurements were performed with an Orian star A212 conductivity meter (Thermo Scientific) at 25 °C. The conductivity probe was calibrated prior to the measurements using standard solutions (1.413, 12.9, 25, 47.6, 80 mS cm^{-1}, Oakton and RICCA). For each concentration, 15 mL of sample was used to measure the conductivity, and three measurements were taken; the reported conductivities are the average of the three results. Between each measurement, the probe was washed with anhydrous ethanol and dried to avoid contamination.

2.5.4 Viscosity

The dynamic viscosity of ionic electrolytes (EPRT-TFSI, MEEV-TFSI$_2$, and TEATFSI) were measured in ACN at 0.25, 0.50, 0.75, and 1.00 M. All the measurements were carried out at 25 °C. 2-3 mL of electrolyte solution was used to measure the viscosity at each concentration and measurements were triplicated to calculate the average viscosity. The dynamic viscosity of solutions was measured using a microfluidic pressure-driven flow viscometer (m-VROC, RheoSense, Inc.). The measuring chip contains a rectangular slit flow channel with uniform cross-section area (50 μm × 2 mm). The fluid sample was pushed by a syringe pump at a constant volume flow rate Q and the pressure drop Δp over a length of channel L was measured.

Four pressure sensors are flush-mounted at the boundary wall in the channel and the shear stress at the wall was calculated from the pressure drop as

$$\tau = \frac{\Delta p}{L} \frac{wh}{2w + 2h} \quad (1)$$

where Δp is the average measured pressure drop over the length L (15 mm). The known flow rate Q is related to the apparent shear rate at the wall, assuming a Newtonian fluid, by

$$\dot{\gamma}_{app} = \frac{6Q}{wh^2} \quad (2)$$

where $\dot{\gamma}_{app}$ is the apparent shear rate at the wall, w and h are the width and height of the channel respectively. For non-Newtonian fluids (non-constant viscosity), the actual shear rate at the wall $\dot{\gamma}$ is related to apparent shear rate $\dot{\gamma}_{app}$ as

$$\dot{\gamma} = \frac{\dot{\gamma}_{app}}{3}\left[2 + \frac{d\ln(\dot{\gamma}_{app})}{d\ln(\tau)}\right] \quad (3)$$

For Newtonian solutions, which were observed in this study, τ is linearly proportional to $\dot{\gamma}_{app}$, so the shear rate at wall $\dot{\gamma}$ is equal to the apparent shear rate $\dot{\gamma}_{app}$. The dynamic viscosity is defined as:

$$\eta = \frac{\tau}{\dot{\gamma}} \quad (4)$$

Experimental limits were obtained based on the maximum and minimum pressure drop that the sensors can measure and the maximum flow rate of the syringe pump, as shown in the gray lines of viscosity versus shear rate plots. For each solution, viscosity was measured within a wide shear rate range (5 000 – 30 000 s^{-1}). Newtonian behavior was observed (less than 10% variation) for this range of shear rate for all samples. The temperature was controlled at 25 °C by a Thermocube circulator.

2.5.5 Diffusivity (NMR Method)

Diffusion coefficients of cationic species of ionic electrolytes (EPRT$^+$, MEEV^{2+}, and TEA$^+$) were determined by a pulse gradient NMR method at 0.25, 0.50, 0.75, and 1.00 M in CD$_3$CN. Spectra from samples of varying concentrations were collected on a 500 MHz JEOL ECZr spectrometer (Peabody, MA, USA) equipped with a Royal Probe. In all cases, the gradients were arrayed from 6 mT/m to 280 mT/m linearly over 32 increments. The pw90 was calculated to be 8.12, 7.914, 7.892 μs for EPRT-TFSI MEEV-TFSI$_2$, and TEATFSI, respectively. The spectral width was set to 15 ppm with the offset at 5 ppm and the temperature was held at 25 °C. 8 scans, along with 4 pre-scans, were collected for each sample. A JEOL standard pulse sequence 'bpp_led_dosy_pfg' was used to collect the spectra. The peak at 7.01, 8.38, 3.13 ppm was used for curve fitting for EPRT-TFSI,

MEEV-TFSI$_2$, and TEATFSI, respectively. Diffusion times for each sample were determined via the min and max gradients (6mT/m and 280mT/m) which resulted in ca. 90% reduction in peak height of the ^{1}H NMR of the sample, using the same parameters as the arrayed spectra. JEOL Delta 5.0.3 software was used for curve fitting analysis and calculation of the diffusion constant. All experiments were done with JOEL's default gradient settings.

2.5.6 Cyclic Voltammetry

Cyclic voltammetry (CV) measurements were performed in an argon-filled glovebox (MBraun, UNIlab) using 650E potentiostat (CH Instruments, Inc.). CVs were recorded in either ACN or 0.5 M TEATFSI/ACN using a three-electrode system with 3 mm diameter glassy carbon as the working electrode (CH Instruments, Inc.), freshly anodized Ag/AgCl wire as the reference electrode (CH Instruments, Inc.), and a Pt wire as the counter electrode (CH Instruments, Inc.) at active materials concentration of 10 mM. Before each measurement, the working electrode was polished on a MicroCloth pad containing an aqueous slurry of 0.05 μm alumina powder (Buehler Ltd.), rinsed with deionized water, and dried under nitrogen. Ferrocene was used as the internal reference and redox potentials were reported with respect to the ferrocene/ferrocenium ($Cp_2Fe^{0/+}$) redox couple. The half-wave redox potential ($E_{1/2}$), peak height ratio (chemical reversibility), and peak separation (electrochemical reversibility) were calculated for each redox event at a scan rate of 100 mV s^{-1}. 100% iR correction was applied to compensate the solution resistance. The solution resistance was determined using iR compensation technique (CH Instruments 650E potentiostat). The resistance measured was from 700 (for MEEV-TFSI$_2$) to 1200 Ω (for EPRT-TFSI) for the active species in ACN and about 60 Ω for the active species in 0.5 M TEATFSI/ACN, which leads to correction of 0.16 (for MEEV-TFSI$_2$ in ACN) to 0.21 V (for EPRT-TFSI in ACN) and 0.01 V (active species in 0.5 M TEATFSI/ACN) at the highest current measured. The diffusion coefficients of the active species at 10 mM concentration were calculated using Randles–Sevcik equation,[14]

$$i_p = 0.4463 \, nFAc \left(\frac{nFD}{RT} v \right)^{0.5} (9)$$

where i_p is the peak current (A), n is the number of electrons transferred (-), F is the Faraday constant (96485 C mol^{-1}), A is the electrode area (cm^2), c is the concentration (mol cm^{-3}), D is the diffusion coefficient (cm^2 s^{-1}), R is the gas constant (8.314 J mol^{-1} K^{-1}), T is the absolute temperature (K), and v is the scan rate (V s^{-1}). The following scan rates were used for diffusion coefficient calculations: 10, 25, 50, 75, 100, 200, 300, 400, and 500 mV s^{-1}.

2.5.7 Solubility

The solubility of EPRT-TFSI and MEEV-TFSI$_2$ was determined in ACN and in 0.5 M TEATFSI / ACN. For determination of solubility, a known amount of each material (approximately 0.3-0.5 g) was added to a 3.5 mL glass vial. Then, the electrolyte solution was added slowly (in a period of 30 s), and the solution was sonicated between additions. Electrolyte addition was continued until the active species completely dissolved, as determined by visual inspection. Once completely dissolved, the weight of the solution was recorded. Then, a known volume of aliquot (100 µL) was taken using a micropipette and the weight of the aliquot was recorded to calculate the density of the solution. The total volume of the initial solution was calculated using the density, and then the molarity of the solution was determined as per the calculated volume. This measurement was performed in triplicate for each active species, and the average molar concentrations were calculated.

2.5.8 Crossover

Solutions of 0.2 M active species (MEEPT, EPRT-TFSI, and MEEV-TFSI$_2$) were prepared in ACN for crossover analysis via two layers of FAPQ 375 PP. The anion exchange membrane (doubly stacked) FAPQ-375-PP (Fumatech) was pre-soaked in ACN for 24 h prior to the crossover experiment. A solution of active material (3.8 mL) was added to the left side of the H cell and ACN (3.8 mL) was added to the right side. First, CVs of original solutions (0.2 M) were recorded at 5 mM in 0.1 M TEATFSI/ACN by taking 125 µL aliquots and diluting into 4.875 mL of electrolyte solution. Then CVs were recorded at 0, 1, 6, 12, and 24 h by taking 125 µL aliquots from the right side the H cell and following

the same dilution into 0.1 M TEATFSI/ACN. Same volume of aliquots (125 µL) were removed from the left side of the H cell to balance the volume at each time. The crossover fractions were calculated by comparing peak currents at each hour to the peak currents of the original CV (0.2 M).

2.5.9   Impedance Measurements

Impedance measurements were collected in an argon-filled glovebox (MBraun) using VSP potentiostat (BioLogic) using the same custom-built-small volume flow cell (more details in section 2.3.9) that was utilized for the flow cell experiments. The anion exchange membrane (doubly stacked) FAPQ-375-PP (Fumatech) was used as received. The electrolyte used in the impedance study contained either 0.5 M TEATFSI (both positive side and negative side) or 0.5 M EPRT-TFSI (positive side) with 0.5 M MEEV-TFSI (negative side). Impedance spectra were obtained a frequency range of 200 kHz to 10 mHz with 5 points per decade. Impedances were measured under potentiostatic control of the cell and the amplitude of the sinusoidal current was 10 mA. The electrolyte was pumped for 24 h to soak the membrane after which the impedance measurements were recorded.

2.5.10   Flow Cell Cycling

Small volume custom flow cells with interdigitated flow fields were used during redox flow cell cycling.[15] The backing plates were made from polypropylene, which has chemical compatibility with the materials used in this manuscript. 3.18 mm thick impregnated graphite was used to make the graphite flow fields (product G347B, MWI Inc., Rochester, NY). The size of carbon paper is 1.7 cm × 1.5 cm with 190 ± 30 µm thickness (SGL 29 AA, SGL group, Wiesbaden, Germany) and used as received. Two pieces of carbon paper was layered on each side of the flow cell. FAPQ-375-PP (Fuma-Tech) was used as membrane. The cells were sealed using custom gaskets cut from polytetrafluoroethylene gasket tape (Goretex) with a 2.55 cm^2 geometric area. All flow cells were assembled in the air and then kept in vacuum state for ~ 1 h before transferred into an argon-filled glovebox (MBraun, O_2 < 5 ppm, H_2O < 0.1 ppm).

10 mL perfluoroalkoxy alkane (PFA) jars (Savillex) were used as electrolyte reservoirs and a peristaltic pump (Masterflex L/S Series) was used to carry the electrolyte at a flow rate of 10 mL min^{-1}. Norprene tubing (Masterflex) was used inside the pump head. PFA tubing (Swagelok) connected the reservoirs to the flow cell. Stainless steel compression fittings (Swagelok) were used to connect the Norprene and PFA tubing. All tubing inner diameters were 1.6 mm.

Four different types of concentrated cells were assembled: i) 0.5 M EPRT-TFSI / 0.5 M MEEV-TFSI$_2$ / separated / ACN / 2FAPQ-375-PP; ii) 0.25 M EPRT-TFSI / 0.25 M MEEV-TFSI$_2$ / mixed / ACN / 2FAPQ-375-PP; iii) 0.75 M EPRT-TFSI / 0.75 M MEEV-TFSI$_2$ / mixed / ACN / FAPQ-375-PP; iv) 0.75 M EPRT-TFSI / 0.375 M MEEV-TFSI$_2$ / mixed / ACN / FAPQ-375-PP. The membranes were soaked in ACN for 24 h before loading samples. Rate and constant current stability studies were performed for each type of flow cell experiments. Data was collected using a VSP potentiostat (BioLogic).

CHAPTER 3. CHAPTER 3. IMPARTING SOLUBILITY IN A STABLE TWO ELECTRON DONOR FOR NONAQUEOUS REDOX FLOW BATTERIES

This chapter is partially reproduced with permission from "Tailoring Two-Electron Donating Phenothiazines to Enable High Concentration Redox Electrolytes for Use in Nonaqueous Redox Flow Batteries" by **N. Harsha Attanayake**, Jeffrey A. Kowalski, Katharine Greco, Matthew D. Casselman, Jarrod D. Milshtein, Steven J. Chapman, Sean R. Parkin, Fikile R. Brushett, and Susan A. Odom, which published in Chemistry of Materials. **2019**, 31(12), 4353-4363. Reproduced by permission of The American Chemical Society (ACS).

3.1   Summary

This study aims to advance our understanding of the physical and electrochemical behavior of nonaqueous redox electrolytes at elevated concentrations and to develop experimentally informed structure-property relationships that may ultimately enable deterministic design of soluble multi-electron-transfer organic redox couples for use in redox flow batteries (RFBs). To this end, we functionalized a phenothiazine core to simultaneously impart two desired properties: high solubility and multiple electron transfer. Specifically, we report the synthesis, solubility, and electrochemical analysis of two new phenothiazine derivatives, 3,7-dimethoxy-*N*-(2-(2-methoxyethoxy)ethyl)phenothiazine and *N*-ethyl-3,7-bis(2-(2-methoxyethoxy)ethoxy)phenothiazine, both of which are two-electron donors that are miscible with nonaqueous electrolytes. This dual-property improvement compared to previous phenothiazine derivatives allows for extended symmetric flow cell experiments for 460 h of cycling of a multi-electron transfer system at high concentrations (0.3 M active material, 0.6 M faradaic concentration), better representing practical devices.

3.2 Introduction

Advancing the science and engineering of organics for use in RFBs requires improvements in our understanding of the physical and electrochemical behavior of nonaqueous electrolytes containing elevated concentrations of organic redox couples. In this study, our specific focus is the performance and longevity of highly soluble multi-electron redox couples. As illustrated in Figure 3.1, we seek to combine previous independent efforts to impart greater molecular solubility with an overarching goal of increasing the volumetric charge-storage capacity of the resultant electrolytes. Initially, we showed improvement of N-ethylphenothaizine (EPT, Figure 3.1) by increasing its solubility through the incorporation of an oligoglycol chain at the N position, leading to N-(2-(2-methoxyethoxy)-ethyl)phenothiazine (MEEPT, Figure 3.1).[1] This functionalization increased solubility across all states of charge such that the neutral species was a liquid that is miscible in polar aprotic solvents common to battery electrolytes, and further, the solubility of the charged species increased five-fold as compared to that of the parent compound. More recently, in an attempt to increase the intrinsic capacity of the parent EPT, we reported that introducing methoxy groups positioned para to nitrogen (3 and 7 positions) resulted in a marked improvement in stability of the dication of N-ethyl-3,7-dimethoxyphenothiazine (DMeOEPT, Figure 3.1).[2] DMeOEPT was insufficiently soluble (< 0.1 M in all states of charge) to enable meaningful flow cell experiments, highlighting the need for further modification of this two-electron-donating core to achieve the high concentrations necessary for flow cell analysis.

Here, we report the synthesis, solubility, and electrochemical analysis of two new phenothiazine derivatives that simultaneously enhance solubility and support multiple electron transfer. The first, 3,7-dimethoxy-N-(2-(2-methoxyethoxy)ethyl)phenothiazine (DMeOMEEPT, Figure 3.1, red), combines the results from our previous work by installing an oligoglycol chain at the N position of the DMeOEPT structure. The second extends the methoxy groups at the 3 and 7 positions with oligoglycol chains, yielding N-ethyl-3,7-bis(2-(2-methoxyethoxy)ethoxy)phenothiazine (B(MEEO)EPT, Figure 3.1, blue). Compared to two-electron-donating DMeOEPT, both derivatives exhibit greater solubility. This dual-property improvement allows for the evaluation of a multi-electron transfer system at high concentrations via symmetric flow cell cycling experiments and

begins to lay the foundation for studying multi-property structure-function relationships under conditions relevant to RFBs.
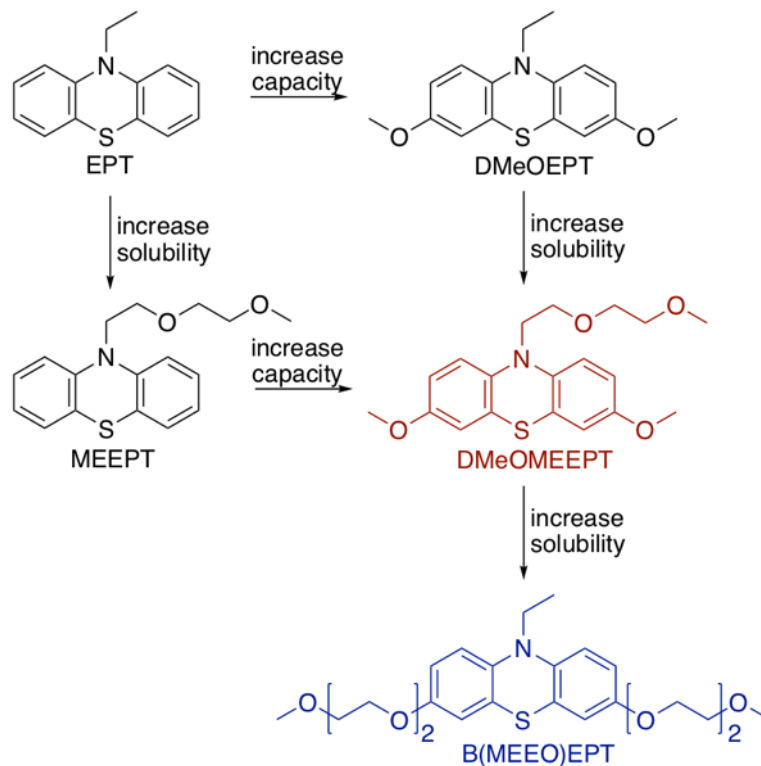
Figure 3.1. Representations of the chemical structures of N-ethylphenothiazine (EPT), *N*-(2-(2-methoxyethoxy)-ethyl)phenothiazine (MEEPT), *N*-ethyl-3,7-dimethoxyphenothiazine (DMeOEPT), 3,7-dimethoxy-*N*-(2-(2-methoxyethoxy)ethyl)phenothiazine (DMeOMEEPT, red), and *N*-ethyl-3,7-bis(2-(2-methoxyethoxy)ethoxy)phenothiazine (B(MEEO)EPT, blue). The molecules are vertically arranged to show an increase in the relative solubility from top to bottom and are horizontally arranged to show an increase in dication stability from left to right. Image created by Prof. Susan Odom.

3.3   Results and Discussion

3.3.1   Synthesis

DMeOMEEPT and B(MEEO)EPT were both prepared in three steps from commercially available materials. To synthesize DMeOMEEPT, phenothiazine was alkylated at the N position to append the 2-(2-methoxyethoxy)ethyl group. The alkylated product, MEEPT, was then brominated at the 3 and 7 positions after which methoxy groups were introduced, replacing the bromine atoms. By accessing two electrons per molecule

the gravimetric capacity increased from 89 mAh g^{-1} to 148 mAh g^{-1} compared to MEEPT. Similarly, to synthesize B(MEEO)EPT, an alkyl group (ethyl) was first installed at the N position of phenothiazine to yield EPT, which was brominated at the 3 and 7 positions, and then treated with the deprotonated oligoglycol to replace the bromine atoms with 2-(2-methoxyethoxy)ethoxy groups, which leads to a gravimetric capacity of 116 mAh g^{-1} assuming two electron transfer events. Detailed synthetic procedures, characterization, and the yield for each synthesis step can be found in the Experimental section.

3.3.2   Materials Screening

Cyclic voltammetry was performed to analyze fundamental, short-term electrochemical behavior, including redox potentials, diffusion coefficients, and both the chemical (stability) and electrochemical (kinetic) reversibilities. Cyclic voltammograms of 1 mM EPT, MEEPT, DMeOEPT, DMeOMEEPT, and B(MEEO)EPT in 0.5 M TEATFSI/ACN are shown in Figure 3.2, with corresponding values for peak potentials, peak separations, and peak-current ratios reported in Table 3.1. Based on the peak separation and peak-current ratios, the first oxidation events of both new materials, DMeOMEEPT and B(MEEO)EPT, are chemically (peak-current ratio of 0.98 – 1.02) and electrochemically (peak separation of 60 – 61 mV) reversible on the CV timescale (~ minutes). However, only for B(MEEO)EPT is the second oxidation event both chemically and electrochemically reversible.
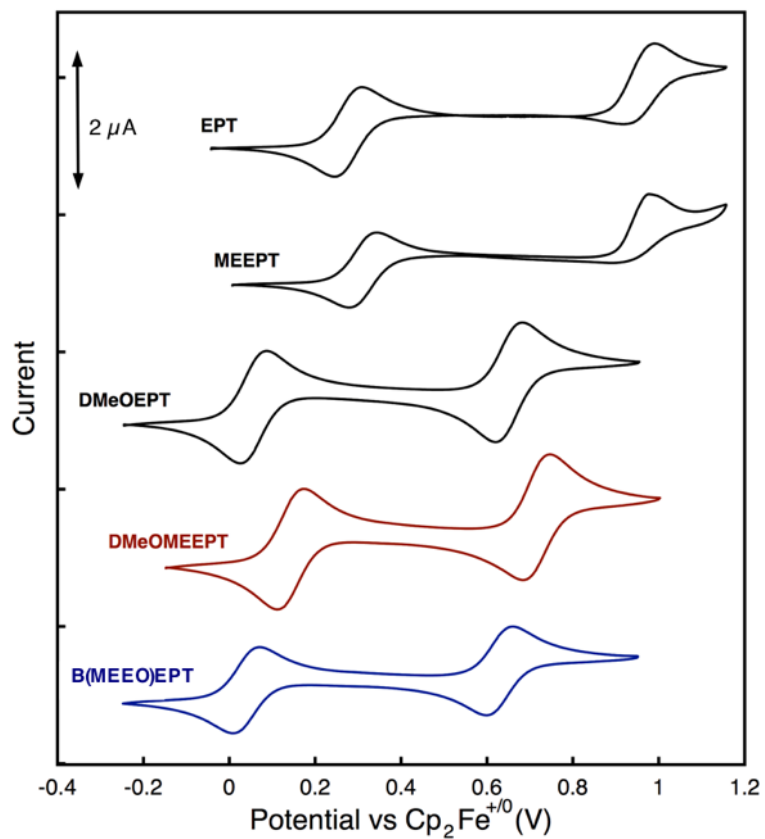
Figure 3.2. Cyclic voltammograms showing the first and second oxidation events of EPT, MEEPT, DMeOEPT, DMeOMEEPT, and B(MEEO)EPT at 1 mM in 0.5 M TEATFSI in ACN at a scan rate of 10 mV s-1, referenced to ferrocenium/ferrocene at 0 V. Cyclic voltammetry experiments performed by Dr. Jeffrey A. Kowalski.

Table 3.1. Measured redox potentials, peak separations, and peak-current ratios for the first and second oxidations, and diffusion coefficients of neutral EPT, MEEPT, DMeOEPT, DMeOMEEPT, and B(MEEO)EPT. All cyclic voltammetry experiments were performed at 1 mM active material concentration. The peak separations and peak-current ratios were calculated at a scan rate of 10 mV s^{-1}. All measurements were performed in triplicate. Cyclic voltammetry experiments performed by Dr. Jeffrey A. Kowalski.

Compound	First Oxidation			Second Oxidation			Diffusion Coefficient ($\times 10^{-6}$ cm^2 s^{-1})
	Potential (V vs. Cp$_2$Fe$^{0/+}$)	Peak Separation (mV)	Peak Current Ratio ($i_{p,ox}/i_{p,red}$)	Potential (V vs. Cp$_2$Fe$^{0/+}$)	Peak Separation (mV)	Peak Current Ratio ($i_{p,ox}/i_{p,red}$)	
EPT	0.278 ± 0.001	61 ± 1	1.00 ± 0.01	0.956 ± 0.002	68 ± 6	0.57 ± 0.09	2.3 ± 0.1
MEEPT	0.311 ± 0.001	61 ± 1	1.00 ± 0.01	0.937 ± 0.002	79 ± 2	0.26 ± 0.02	1.6 ± 0.1
DMeOEPT	0.056 ± 0.001	60 ± 1	0.99 ± 0.01	0.655 ± 0.001	60 ± 1	1.01 ± 0.01	1.8 ± 0.1
DMeOMEEPT	0.093 ± 0.001	60 ± 1	0.99 ± 0.02	0.666 ± 0.001	60 ± 1	0.90 ± 0.05	1.6 ± 0.1
B(MEEO)EPT	0.064 ± 0.001	61 ± 1	1.02 ± 0.04	0.654 ± 0.001	61 ± 1	1.01 ± 0.01	0.8 ± 0.1

The potentials of the first and second oxidation events are similar for both CDMeOMEEPT (0.093, 0.666 V vs. Cp$_2$Fe$^{0/+}$) and B(MEEO)EPT (0.025, 0.625 V vs. Cp$_2$Fe$^{0/+}$), with DMeOMEEPT exhibiting slightly higher (more positive) potentials than B(MEEO)EPT due to the inductive effect of the oxygen atoms in the 2-(2-methoxyethoxy)ethoxy group at the N position in DMeOMEEPT, which is more electron-withdrawing than the ethyl group at the equivalent (N) position in B(MEEO)EPT. An equivalent trend with a difference of similar magnitude is also observed for the first oxidation potentials of EPT and MEEPT, which contain the same functional groups (ethyl and 2-(2-methoxyethoxy)ethoxy, respectively) at their N positions.[1] The oxidation potentials of DMeOMEEPT and B(MEEO)EPT are reduced by ca. 0.2 V compared to their N-alkylated equivalents MEEPT and EPT, respectively, due to the resonance contribution of the O atoms to the phenothiazine π system. A difference of similar magnitude was observed in EPT and DMeOEPT.[39] While the first redox event is less positive than derivatives lacking alkoxy groups at the 3 and 7 positions, the average redox potential increases due to the ability to access the second redox event.
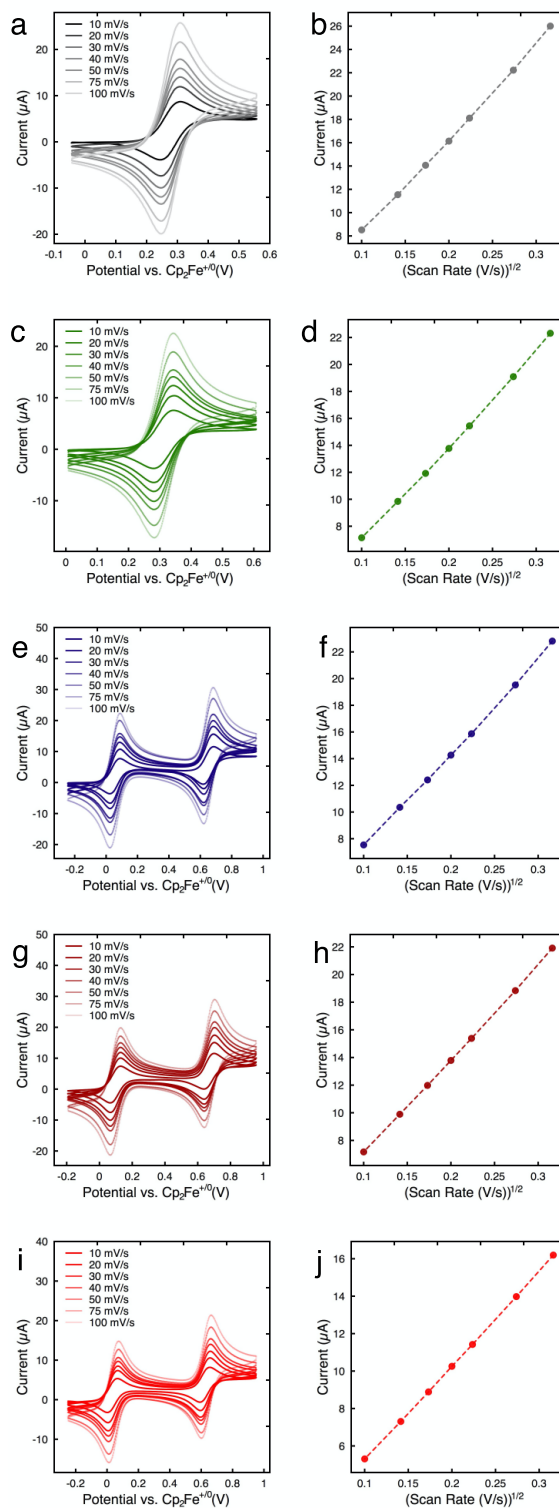
Figure 3.3. Cyclic voltammograms of EPT (a), MEEPT (c), DMeOEPT (e), DMeOMEEPT (g), and B(MEEO)EPT (i) at 0.001 M in 0.5 M TEATFSI/ACN at scan rates of 10, 20, 30, 40, 50, 75, and 100 mV s^{-1}. Additionally, the corresponding Randles-Sevcik plots are shown for EPT (b), MEEPT (d), DMeOEPT (f), DMeOMEEPT (h), and D(MEEO)EPT (j).

The volumetric capacity of a flow cell is limited by the solubility of the least soluble species. To determine this upper bound, the solubility of each relevant state of charge (neutral, radical cation, and dication) was measured. To perform this measurement radical cation and dication salts of DMeOMEEPT and B(MEEO)EPT were prepared and isolated as solids via chemical oxidation. Chemical oxidation with one or two equivalents of NOBF$_4$ results in electron transfer from the phenothiazine core to the nitrosonium (NO$^+$) cation, forming one or two equivalents of the neutral NO gas and either the tetrafluoroborate salt of the radical cation or the bis(tetrafluoroborate) salt of the dication, respectively. UV-vis spectra of the oxidized species verify that unique products form, as evidenced by features distinctive both from each other and from the neutral starting material, as shown for B(MEEO)EPT in Figure 3.4. Key features include a peak at 318 nm for the neutral compound; an intense peak at 629 nm and two sharp, less intense peaks at 354 and 394 nm for the radical cation; and peaks at 593 and 922 nm for the dication. These spectra are nearly identical to those of previously reported DMeOEPT,[39] which was expected due to the similarities in electronic structure.
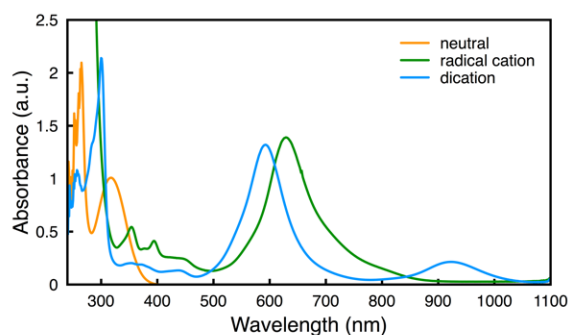
Figure 3.4. UV-vis absorption spectra of the neutral, radical cation, and dication forms of B(MEEO)EPT in ACN.

The solubilities of the neutral, radical cation, and dication forms of DMeOMEEPT and B(MEEO)EPT were compared in 0.5 M TEABF$_4$/ACN and in 0.5 M TEATFSI/ACN (Table 3.2). We selected 0.5 M TEATFSI/ACN for flow cell experiments due to the higher solubility of the neutral and charged states with the TFSI$^-$ salt. While DMeOEPT is a solid at room temperature, the oligoglycol groups in the new materials lower their melting points and impart greater solubility. Both neutral compounds are liquids at room temperature and are miscible in nonaqueous electrolytes. The radical cation and dication salts of both compounds are solids, with lower solubilities than the miscible neutral forms. With two glycol chains, the solubility of the radical cation and dication forms of B(MEEO)EPT (0.55 and 0.54 M) is higher than those of the charged forms of DMeOMEEPT (0.11 and 0.10 M) (Table 3.2). Due to the combination of higher solubility in both oxidized forms as well as greater reversibility of the first and second oxidation events, we elected to use B(MEEO)EPT in flow cell experiments.

Table 3.2. Solubilities of the neutral molecules, their tetrafluoroborate radical cation salts, and their bis(tetrafluoroborate) dication salts of DMeOEPT, DMeOMEEPT, and B(MEEO)EPT in 0.5 M TEATFSI/ACN, and for the neutral molecules and radical cations of EPT and MEEPT. The radical cation salts and the dication salts had tetrafluoroborate (BF$_4$) as a counter ion. Solubility values are reported in molarity (M).

Compound	Neutral Species (M)	Radical Cation (M)	Dication (M)
EPT	0.10 ± 0.01	0.28 ± 0.01	– *
MEEPT	miscible	0.40 ± 0.01	– *
DMeOEPT	0.05 ± 0.01	0.06 ± 0.01	0.05 ± 0.01
DMeOMEEPT	miscible	0.11 ± 0.01	0.10 ± 0.01
B(MEEO)EPT	miscible	0.55 ± 0.01	0.54 ± 0.01

*Dication data is not included for EPT and MEEPT, as they were not stable enough to isolate.

With B(MEEO)EPT selected for flow cell cycling studies, it was necessary to scale up the synthesis of this material, in its radical cation form, as the starting point on both sides of the symmetric flow cell. Thus, we scaled up the synthesis of the tetrafluoroborate radical cation salt of B(MEEO)EPT, performing reactions in batches as large as 8 g (mass of isolated material), again using NOBF$_4$ as the chemical oxidant. To confirm the identity

of the radical cation salt, we crystallized the expected product, B(MEEO)EPT-BF$_4$, and analyzed resultant crystals using X-ray diffraction. The thermal ellipsoid plot obtained from X-ray experiments is shown in Figure 3.5. Notably, the isolation of this salt as X-ray quality single crystals not only provides proof of structural assignment but also demonstrates the stability of this organic radical cation.
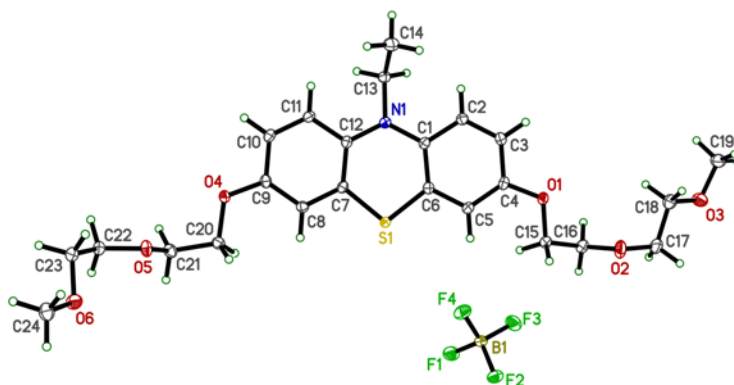
Figure 3.5. Thermal ellipsoid plot of B(MEEO)EPT-BF$_4$ obtained from single-crystal X-ray diffraction experiments from the scaled-up synthesis. X-ray diffraction experiments performed by Dr. Sean R. Parkin.

3.3.3 Flow Cell Cycling

Symmetric flow cells offer many benefits when evaluating soluble redox active materials under flow battery relevant conditions.[1, 11-12] All states of charge of a single redox couple can be accessed, the possibility of contamination from a counter electrode is removed, and the flowing electrolyte increases mass transfer through the porous electrodes, allowing for higher active material concentrations and current densities to be employed. Here, we used a symmetric cell configuration to investigate rate capabilities and cycle stability of B(MEEO)EPT across all three oxidation states. In the case of symmetric cells utilizing one-electron donors, two different states of charge are accessed in each chamber: the neutral species, P, and the radical cation, P$^{+\bullet}$. However, when two-electron donating active species are studied, three different states of charge are accessible, so in addition to the neutral species and the radical cation, the dication, P^{++}, is also present (Figure 3.6a). In an ideal constant current cycling experiment for a two-electron donor, two unique potential plateaus occur at voltages of equal magnitude and opposite sign, with each plateau

corresponding to 50% of the total charge capacity (Figure 3.6b). Therefore, at 50% state of charge, a sharp increase (charging) or decrease (discharging) in the potential occurs. When charging begins, P is oxidized to $P^{+\bullet}$ on one side of the cell, and P^{++} is simultaneously reduced to $P^{+\bullet}$ on the other side, leading to the first voltage plateau. Once P and P^{++} are depleted, both tanks contain only $P^{+\bullet}$. At this point, $P^{+\bullet}$ is oxidized to P^{++} on one side of the cell and is reduced to P on the other side, leading to the second plateau. During discharge, the reverse reactions occur, again leading to two distinct voltage plateaus.
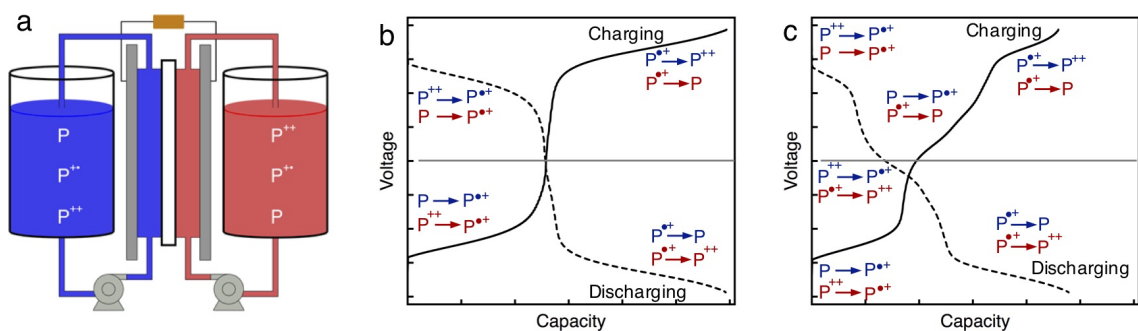
Figure 3.6. Schematic of a symmetric flow cell showing the states of charged accessed for a given molecule, P, with three stable oxidation states (a), and the corresponding charging (dotted line) and discharging (solid line) potential profiles for constant current cycling labeled with the electrochemical reactions corresponding to each voltage plateau in a balanced cell (b) and an imbalanced cell (c). Image created by Prof. Susan Odom.

An imbalanced cell can result from a mismatch in electrolyte volume on each side of the cell (e.g., from crossover) and/or from a mismatch in respective active species concentrations. This phenomenon may be a result of cell polarization and species crossover that is exacerbated by the use of a non-selective separator. Specifically, as the current density increases, the cell will reach the prescribed voltage cutoff before all of the molecules have been oxidized or reduced leaving mixtures of $P/P^{+\bullet}$ and $P^{+\bullet}/P^{++}$ on either side of the cell, which, in turn, will present as a third voltage plateau on subsequent charge and discharge cycles (Figure 3.6c). This behavior is further complicated and compounded by active species crossover between the two electrolytes. If the amount of P on one side of the cell is less than the amount of P^{++} on the other side, upon complete oxidation of P to $P^{+\bullet}$, an excess of P^{++} will remain unreduced on the opposite side (Figure 3.6c). An example of a voltage profile in this scenario is shown in Figure 3.6c during both charge and

discharge. The expected cell voltage is 0 V because the reaction is cycling against itself.[11] The capacity of this middle plateau is dependent on the amount of excess active material (whether P or P^{++}) present on one side of the cell. Note that a third plateau also forms if the reduction of P^{++} to $P^{+\bullet}$ was the limiting reaction. The formation of this new voltage plateau emphasizes a challenge with two-electron transfer molecules and the importance of preventing crossover during cell operation because a mismatch in active species concentration not only reduces the accessed capacity, but also alters the voltage profile observed during cell cycling.

Several approaches can allow for the configuration a balanced symmetric cell before starting charge/discharge cycling. These include (i) loading equal volumes of two separate, equimolar of solutions of P and P^{++}, (ii) premixing P and P^{++} in a 1:1 ratio, dividing the resulting solution into two equivalent volumes, and then pre-charging the cell to reduce $P^{+\bullet}$ to P on one side and oxidize $P^{+\bullet}$ to P^{++} on the other side, or (iii) dividing a solution of only $P^{+\bullet}$ into two equivalent volumes and then pre-charging the cell to reduce and oxidize to P and P^{++} respectively. Here, we employ the third approach for the convenience of a single starting material and due to the challenges of preventing electrolyte mixing across the non-selective separator during cell start-up.

We first performed a variable rate experiment to determine the tradeoff between applied current density, overpotential, and accessed capacity with a secondary goal of identifying an appropriate current density for analyzing B(MEEO)EPT stability in symmetric cells. Thus, we conducted a rate study, cycling cells containing B(MEEO)EPT for five cycles each at current densities of 10, 20, 30, 40, and 50 mA cm^{-2}, followed by five more cycles at 10 mA cm^{-2}, the last of which was performed to determine whether accessing the higher current densities adversely impacts cell components (e.g., electrode degradation) and/or active material. The voltage vs. capacity profiles for the fifth cycle at each current density are shown in Figure 3.7a, and the charge and discharge capacities with the coulombic efficiencies are shown in Figure 3.7b. As expected, the accessed capacities decreased as current densities increase, which is due to the larger cell polarization present at high current densities. As evidenced by a comparison the 5th cycle in the first and last sets of 10 mA cm^{-2} cycles, the capacity faded by about 8% over the course of the 145 h

experiment which we tentatively attribute to the emergence of a third voltage plateau centered around 0 V (Table 3.3).
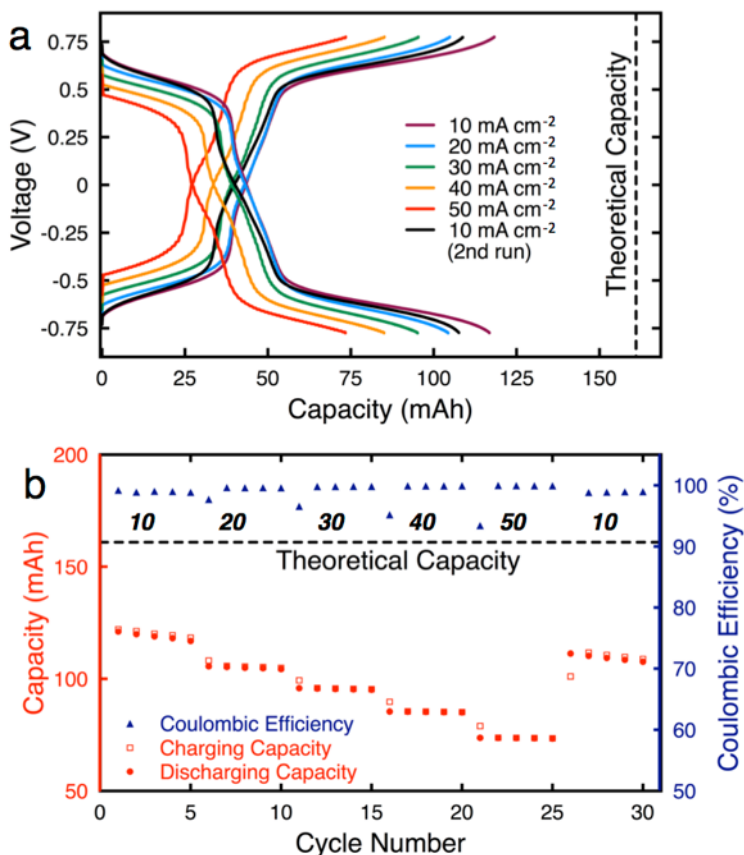
Figure 3.7. Rate study of B(MEEO)EPT cycling in a symmetric flow cell, showing the potential vs. capacity (a) and the capacity vs. cycling number (b) at various applied current densities. The numerical values below each coulombic efficiency segment represent the applied current densities in mA cm^{-2}. The potential cut-offs for each flow cell experiment were ± 0.775 V. In both figures, a dashed black line is drawn to represent the theoretical capacity (161 mAh). The total experimental run time was 145 h. Rate study performed by Katharine Greco.

Table 3.3 highlights the additional tradeoff between the current density and the charging/discharging efficiency. The difference in accessed capacity of the two voltage plateaus observed in the voltage vs. capacity profiles in Figure 3.7a and Table 3.3 show a deviation from the idealized behavior illustrated in Figure 3.6b. The percent of charging and discharging capacity accessed at each plateau is calculated by identifying the maximum (charging) or minimum (discharging) in the derivative of the voltage profile as

each extreme represents the transition from one redox plateau to another.[60] For reference, in the ideal case, the capacity would be split evenly between the low and high voltage plateaus with no intermediate voltage plateaus.

Table 3.3. Percent of the charging and discharging capacity accessed on each potential plateau during charging and discharging and the corresponding accessed capacity and coulombic efficiency for each of the current densities examined, obtained from the variable-rate cycling data shown in 3.7. The data corresponds to the average of each charging/discharging cycle.

Current Density (mA cm^{-2})	Charging			Discharging			Accessed Capacity (%)	Coulombic Efficiency (%)
	Lower Plateau (%)	Middle Plateau (%)	Upper Plateau (%)	Lower Plateau (%)	Middle Plateau (%)	Upper Plateau (%)		
10	33.3 ± 0.2	9.6 ± 0.2	57.1 ± 0.4	56.5 ± 0.2	9.4 ± 0.3	34.1 ± 0.1	73.5	98.8
20	37.5 ± 0.3	10.7 ± 0.3	51.8 ± 0.1	51.7 ± 0.1	10.6 ± 0.1	37.7 ± 0.1	65.1	99.5
30	37.8 ± 0.4	11.9 ± 0.1	50.3 ± 0.3	50.2 ± 0.1	11.8 ± 0.1	38.0 ± 0.1	59.2	99.8
40	36.9 ± 0.7	13.6 ± 0.1	49.5 ± 0.4	49.7 ± 0.1	13.1 ± 0.1	37.2 ± 0.1	52.9	99.9
50	35.5 ± 0.8	14.0 ± 0.4	51 ± 1	51.5 ± 0.2	14.9 ± 0.5	33.6 ± 0.6	45.6	99.9
10	30 ± 2	14.9 ± 0.4	55 ± 2	52.9 ± 0.2	14.6 ± 0.4	32.5 ± 0.1	67.6	98.9

Two notable trends are observed in Table 3.3. First, as anticipated, the lower current densities – thus longest cycles – showed the lower coulombic efficiencies, albeit only 1.0 to 1.1% lower than the shortest cycle. We attribute this minor inefficiency to in-cycle active species crossover and self-discharge through the non-selective separator. Second, in general, the active materials appear to spend more time in the extreme voltage plateaus. A similar but simpler case (i.e., no convection) of this behavior would be voltage profiles associated with Sand's time measurements for different oxidation states of multiple electron transfer materials.[60] If translated to full redox flow cell operation (e.g., second redox couple at a disparate voltage), this observation suggests lower voltage efficiencies and consequently reduced energy efficiencies. Indeed, similar observations were made by Laramie et al. when studying two electron transfer molecules in a full cell.[61] We note that there does not appear to be a current density dependence of this trend over the relatively narrow range of current densities explored which is also in agreement with Sand's time analysis.[60] More broadly, this inefficiency is intrinsic to materials with multiple, independent electron transfer events, suggesting that, in principle, greater volumetric

capacities are achievable but with a concomitant penalty in voltaic efficiency. A quantitative description of this trade-off is beyond the scope of the present work but will be addressed in the future.

Constant current symmetric cell cycling was then performed to evaluate the long-term stability of B(MEEO)EPT. Here, a symmetric cell was assembled with each half cell containing 10 mL of solution containing 0.3 M B(MEEO)EPT (0.6 M faradaic concentration) in 0.5 M TEATFSI in ACN, and cycling was performed at 25 mA cm^{-2}. This current density was chosen to balance experimental runtime (roughly 2 h for each half cycle) and fraction of the capacity accessed per cycle. Figure 3.8a shows the voltage vs. capacity profiles for the charge and discharge of select cycles. The charge and discharge capacities and coulombic efficiencies for each cycle are shown in Figure 3.8b.
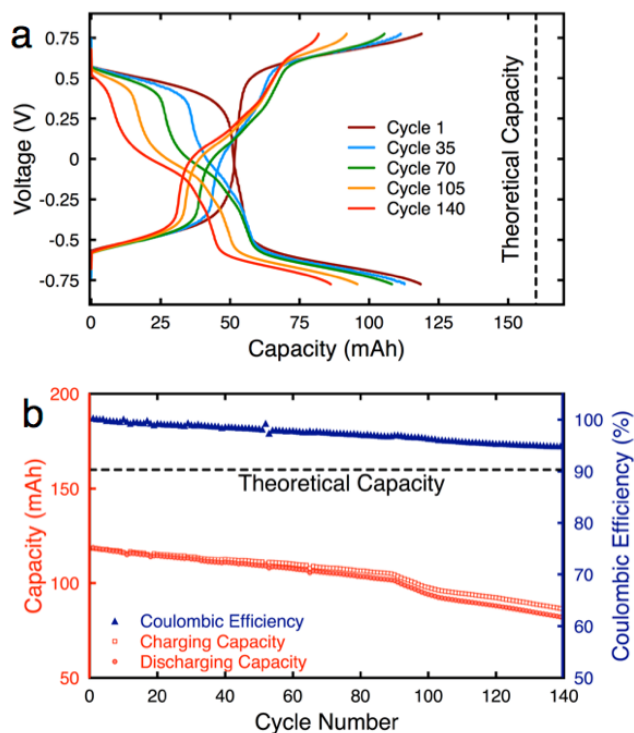
Figure 3.8. Constant current cycling of B(MEEO)EPT in a symmetric flow cell at 25 mA cm^{-2} accessing both electron transfer events: capacity vs. potential (a), charging (red, square) and discharging (red, circle), as well as the coulombic efficiencies (blue, triangle) as a function of cycle number (b). The potential cut-offs imposed during the flow cell experiment were $\pm$ 0.775 V. The theoretical capacity (dashed black line) is 16.1 Ah L^{-1} (161 mAh) and the total experimental runtime was 460 h. Flow cell cycling experiment performed by Dr. Jeffrey A. Kowalski.

In this cycling experiment, about 80% of the theoretical capacity was accessed initially, which is larger than expected based on the rate study and tentatively attributed to variability in the cell build (i.e., slightly lower area specific resistance) and the initial symmetry of the cell (i.e., no start-up or operation-induced electrolyte misbalance). Over the course of the

experiment (460 h), a 27% capacity fade was observed. For the first 85 cycles (300 h), the capacity faded at a rate of ca. 0.1% per cycle, while for cycles 86-140 the average fade rate increased to ca. 0.4% per cycle. We hypothesize that the majority of this performance decay is due to the combination of cell polarization and active species crossover, rather than material degradation, and thus may ultimately be reversible. This hypothesis is supported by the appearance and growth of a new voltage plateau around 0 V over the course of the experiment (Figure 3.6b). Indeed, by cycle 140, the capacity accessed on this middle plateau was near equal to that accessed on the lower plateau and greater than that of the upper potential plateau. As the new plateau continued to increase, the accessed capacity decreased because more B(MEEO)EPT$^{+\bullet}$ remains either unoxidized or unreduced on one side of the cell. In addition, at the end of the experiment, unequal solution volumes were observed in the two electrolyte chambers which is evidence of a capacity-limiting electrolyte imbalance.

3.3.4 Post-test analyses

To determine whether the observed capacity loss was due to limitations in cell assembly and operation as opposed to active species decomposition, we analyzed the cycled positive and negative electrolyte solutions using microelectrode voltammetry (Figure 3.9a) and UV-vis absorption spectroscopy (Figure 3.9b). Microelectrode voltammetry was employed because it enables direct electrolyte analysis without dilution. Moreover, the presence (or absence) of individual species as well as their relative concentrations in the electrolyte solutions can be extracted from the steady-state voltammetric response.[60] Three current plateaus were present in each microelectrode voltammogram where the lowest voltage (most negative) plateau corresponds to the neutral form of B(MEEO)EPT, the middle plateau to the radical cation, and the highest plateau to the dication. The plateau closest to a y-axis value of zero represents the highest concentration species in the solution. The cell was stopped and disassembled in the charged state; therefore, the positive electrolyte as defined by the electrolyte connected to the working electrode should ideally contain only P++, whereas the negative electrolyte (counter electrode) ideally would only contain P.
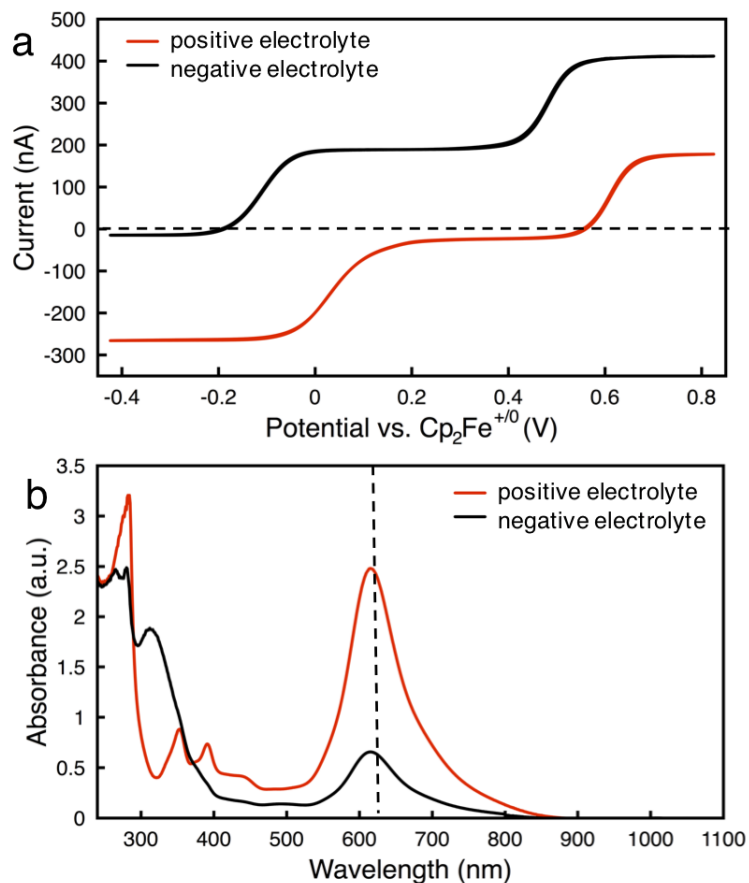
Figure 3.9. Carbon fiber microelectrode cyclic voltammetry scans (10 mV/s) of the positive electrolyte (red) and negative electrolyte (black) after symmetric cell cycling at 0.3 M in active material (a), and corresponding UV-vis absorption spectra (b). For UV-vis measurements, the working solutions were diluted 1000× to reach an estimated total species concentration of 0.3 mM, assuming equal species distribution across the negative electrolyte and positive electrolyte and no decomposition of B(MEEO)EPT into a new molecular species. Post-test analysis experiments performed by Dr. Jeffrey A. Kowalski.

From the microelectrode, the dominant species in the positive electrolyte and negative electrolyte are the radical cation and the neutral compound, respectively. Further, for the negative electrolyte, there is a slight reducing current at the lowest potentials used (i.e., on the plateau corresponding to the neutral species) indicating that there is either radical cation or dication or both present. However, it is likely that any dication in solution would react with the excess neutral species, only leaving the radical cation and neutral species. Similarly, for the positive electrolyte, there is a slight negative current at the intermediate potentials (i.e., on the plateau corresponding to the radical cation) implying that there is some dication in solution that can be reduced. In both cases, based on the

relative current magnitudes, we can deduce that the majority species in each solution are at least an order of magnitude greater concentration than the minority species, but quantitative assessment of minority species concentrations required knowledge of species-specific diffusion coefficients. Thus, we can conclude that there is at least radical cation and dication in the positive electrolyte and at least neutral species and one oxidized species in the negative electrolyte, and it is possible that more species are also present (neutral in the positive electrolyte and dication in the negative electrolyte). In Figure 3.9b, the UV-vis spectra show the presence of radical cation in the positive electrolyte and a combination of neutral compound and radical cation in the negative electrolyte. We see no evidence of active species decomposition in the UV-Vis spectra, suggesting that this is not the source of capacity fade. Further, we do not see any signature of the dication in the UV-vis absorption spectra, which were obtained about a week after microelectrode voltammetry experiments. We hypothesize that homogeneous disproportionation reactions, between the dication and neutral compound to produce two radical cations, occurs continuously post-mortem which would explain the lower dication concentration in Figure 3.9a and the lack of dication in Figure 3.9b.

3.4   Conclusions

In summary, we report two new two-electron-donating phenothiazine derivatives in which solubility and stability of the neutral, radical cation, and dication forms in a nonaqueous electrolyte are significantly increased compared to previous phenothiazine derivatives. By introducing one or two oligoglycol chains on the periphery of a less soluble two-electron donating core, the solubility of the new derivatives is improved to a point similar to that of the previously-reported one-electron donor (MEEPT), miscible with 0.5 M TEATFSI/ACN in its neutral form. In particular, for B(MEEO)EPT, the increase in molecular weight by a factor of 1.5 compared to one-electron-donating MEEPT is offset by a doubling in electron storage capacity per phenothiazine unit without compromising solubility. However, a 0.6 V gap still exists between the electron transfer events leading to additional charging/discharging inefficiencies, which will need to be reduced to limit operation losses. B(MEEO)EPT is sufficiently soluble in all three states of charge as to allow for symmetric flow cell cycling experiments at concentrations of 0.3 M (0.6 M

72

faradaic concentration). During long term symmetric cell cycling, B(MEEO)EPT cycled for 460 h with ca. 30% capacity fade.

Importantly, although capacity fade is observed, our experimental results indicate that this is due to limitations in our experimental apparatus, specifically the use of a non-selective separator, rather than decomposition of the redox couple. The evolution of the cell polarization observed during cycling is consistent with active species crossover as evidenced by both the appearance of a new potential plateau at around 0 V and the imbalanced electrolytes at the end of the experiment. Moreover, the results from combined microelectrode and UV-vis analyses of cycled electrolytes suggest that the coulombic inefficiencies are mostly due to self-discharge of the dication form of B(MEEO)EPT through electron-transfer reactions, potentially disproportionation with the neutral species. As such, if suitable conductive and selective separators were employed, we anticipate that more extensive cycling could be realized with B(MEEO)EPT. More broadly, though further improvements in the phenothiazine derivatives to increase redox potentials and reduce the voltage gap between electron transfer events will ultimately be necessary to realize high voltage nonaqueous RFBs, this study represents an important example of multi-property tuning of organic molecules for charge storage. While the functionalization strategies reported here are targeted to phenothiazine derivatives in electrolytes based on polar aprotic solvents, the design ethos and approach outlined are generalizable and can be applied to other organic redox materials for use in electrochemical technologies.

3.5   Experimental

3.5.1   Synthesis

Materials

Phenothiazine (≥99%), sodium hydride (60% dispersion in mineral oil), and copper(I)   iodide   (≥98%)   were   purchased   from   Acros Organics. Diethylene glycol monomethyl ether (99%) and methyl formate (98%) were purchased from Tokyo Chemical Incorporated. Nitrosonium tetrafluoroborate (98%) was

purchased from Alfa Aesar and was stored and weighed in an argon-filled glovebox (MBraun, $O_2 < 0.1$ ppm, $H_2O < 0.5$ ppm). Anhydrous pyridine (99.8%), *N*-bromosuccinimide (NBS) (99%), anhydrous methanol (99.8%), and sodium (99.9%) were purchased from Sigma-Aldrich. Other solvents were purchased from VWR. Silica gel (65 × 250 mesh) was purchased from Sorbent Technologies. ^1H and ^{13}C NMR spectra were obtained on 400 MHz Varian spectrometers in DMSO-d_6 from Cambridge Isotope Laboratories. Mass spectra were obtained on an Agilent 5973 Network mass selective detector attached to Agilent 6890N Network GC system. Elemental analyses were performed by Atlantic Microlab, Inc. Solubility tests and cyclic voltammetry measurements were performed in an argon-filled glove box (MBraun Labmaster, $O_2 < 0.1$ ppm, $H_2O < 5$ ppm).

   N-ethylphenothiazine (EPT),[3] *N*-((2-methoxy)ethoxy)ethylphenothiazine (MEEPT),[1] N-ethyl-3,7-dibromophenothiazine (DBrEPT),[4] N-ethyl-3,7-dimethoxyphenothiazine (DMeOEPT) and *N*-ethyl-3,7-dimethoxyphenothiazine tetrafluoroborate (DMeOEPT-BF$_4$),[2] were synthesized as previously reported. Synthetic procedures and spectroscopic analysis for DMeOMEEPT, B(MEEO)EPT, their precursors, and radical cation salts are included in the Supporting Information, as are their representative NMR and EPR spectra.
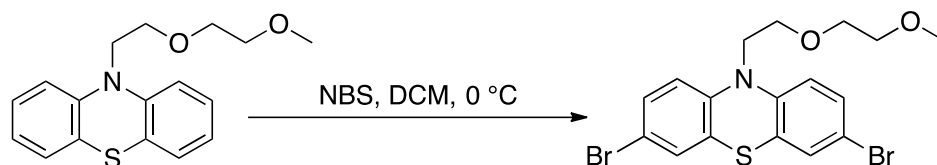
3,7-Dibromo-*N*-((2-methoxy)ethoxy)ethylphenothiazine (DBrMEEPT). N-((2-methoxy)ethoxy)ethylphenothiazine (1.12 g, 3.73 mmol) was dissolved in anhydrous DCM (11 mL) in a 50 mL round-bottomed flask. The reaction flask was immersed in an ice water bath, and *N*-bromosuccinimide (2.0 g, 11 mmol) was added in small portions over 10 min. The reaction was stirred at 0 °C for 30 min. Upon completion of the reaction, the reaction mixture was quenched with sodium thiosulfate, diluted with dichloromethane, and then the organic layer washed with water and brine. The organic extracts were dried over magnesium sulfate, filtered and concentrated by rotary evaporation. The organic residue was purified by silica gel chromatography using 40% ethyl acetate in hexanes as eluent to

afford the product as a pale red oil (1.03 g, 60%). ^{1}H NMR (DMSO-d$_6$, 400 MHz, ppm) δ 7.35 (m, 4H), 7.00 (dd, J = 6.8, 2.8 Hz, 2H), 4.00 (t, J = 5.6 Hz, 2H), 3.69 (t, J = 5.6 Hz, 2H), 3.51 (m, 2H), 3.40 (m, 2H), 3.19 (s, 3H). ^{13}C NMR (DMSO-d$_6$, 100 MHz, ppm) δ 143.7, 130.5, 129.1, 125.4, 117.7, 114.31, 71.4, 69.8, 67.2, 58.2, 47.5. GCMS: m/z 457/459/461 (~1:2:1, 63%), 368/370/372 (~1:2:1, 100%), 354/356/358 (~1:2:1, 25%), 336/338/340 (~1:2:1, 16%), 289/291 (~1:1, 31%), 207 (18%), 196 (26%). Anal. calcd. for C$_{17}$H$_{17}$Br$_2$NO$_2$S C, 44.47; H, 3.73; N, 3.05. Found C, 44.61; H, 3.74; N, 3.05.
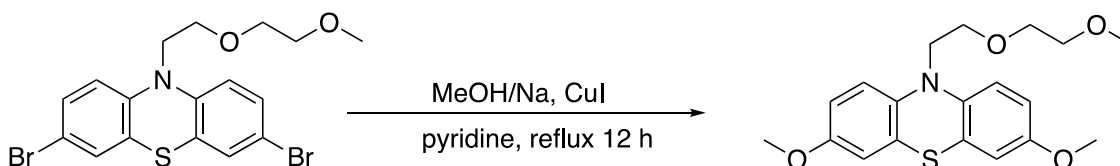
3,7-Dimethoxy-*N*-((2-methoxy)ethoxy)ethylphenothiazine (DMeOMEEPT). Sodium methoxide solution was prepared by dissolving sodium (0.50 g, 22 mmol) in 7 mL methanol. To the methoxide solution, copper(I) iodide (1.65 g, 8.68 mmol), DBrMEEPT (1.00 g, 2.17 mmol) and pyridine (10.8 mL) were added. The reaction mixture was purged with nitrogen for 15 min. A reflux condenser was attached and the reaction was refluxed for 12 h. Upon completion of the reaction, the reaction mixture was diluted with diethyl ether and washed with brine. The organic extracts were dried over magnesium sulfate, filtered and concentrated by rotary evaporation. The organic residue was purified by silica gel chromatography using 40% ethyl acetate in hexanes as the eluent to afford the product as a colorless oil (0.35 g, 45%). ^{1}H NMR (DMSO-d$_6$, 400 MHz, ppm) δ 6.95 – 6.90 (m, 2H), 6.78 – 6.72 (m, 4H), 3.92 (t, J = 5.9 Hz, 2H), 3.68 (s, 6H), 3.66 (d, J = 5.9 Hz, 2H), 3.54 – 3.48 (m, 2H), 3.43 – 3.37 (m, 2H), 3.20 (s, 3H). ^{13}C NMR (DMSO-d$_6$, 100 MHz, ppm) δ 154.7, 138.5, 124.6, 116.1, 112.9, 112.4, 71.3, 69.7, 67.5, 58.04, 55.4, 47.3. GCMS: m/z 361 (77%), 272 (100%), 258 (78%), 240 (60%), 215 (26%), 172 (12%). Anal. calcd. for C$_{19}$H$_{23}$NO$_4$S C, 63.14; H, 6.41; N, 3.88. Found C, 63.16; H, 6.55; N, 3.90.
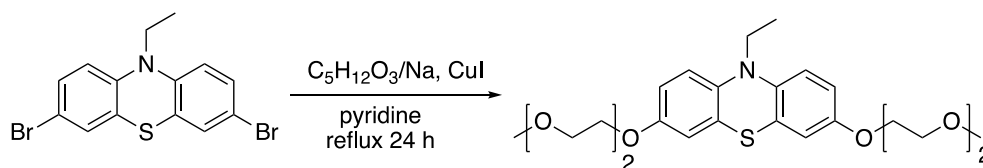
***N*-ethyl-3,7-bis(2-(2-methoxyethoxy)ethoxy)phenothiazine (B(MEEO)EPT)**, **Method I**. An oven-dried 1 L round-bottomed flask was transferred to an argon filled glove box, then diethylene glycol monomethyl ether (390 mL, 3.41 mol) was added into the round-bottomed flask, which was capped and removed from the glove box. Freshly cut sodium metal (9.56 g, 416 mmol) was dissolved in diethylene glycol monomethyl ether under nitrogen atmosphere. Then, copper(I) iodide (31.65 g, 168.2 mmol), DBrEPT (16.00 g, 41.55 mmol) and anhydrous pyridine (320 mL) were added to the resulting solution. Afterward, the reaction mixture was sparged with nitrogen about 15 min while stirring. The round-bottomed flask was immersed in an oil bath and the reaction mixture was refluxed for overnight. Upon completion of the reaction, the reaction mixture was concentrated by rotary evaporation. Then reaction mixture was diluted with ethyl acetate and washed with 1 M aq. HCl, water and brine. The combined organic extracts were dried over magnesium sulfate and concentrated by using rotary evaporation. Finally, organic residue was purified on a silica gel column using 20-50% ethyl acetate in hexanes. The silica gel was neutralized with trimethylamine (2 -3 mL) during packing the column. The product was yellow/light red viscous liquid (14.8 g, 77%). ^{1}H NMR (DMSO-d$_6$, 400 MHz, ppm) δ 6.90 – 6.85 (m, 2H), 6.79 – 6.75 (m, 4H), 4.05 – 3.98 (m, 4H), 3.79 (q, J = 6.9 Hz, 2H), 3.71 – 3.65 (m, 4H), 3.58 – 3.52 (m, 4H), 3.47 – 3.41 (m, 4H), 3.23 (s, 6H), 1.23 (t, J = 6.9 Hz, 3H). ^{13}C NMR (DMSO-d$_6$, 100 MHz, ppm) δ 153.9, 138.7, 124.5, 116.0, 113.8, 113.3, 71.5, 69.9, 69.1, 67.8, 58.3, 41.3, 12.9. GCMS: m/z 463 (100%), 434 (30%), 360 (11%), 230 (14%), 103(18%), 59 (47%). Anal. calcd. for C$_{24}$H$_{33}$NO$_6$S C, 62.18; H, 7.18; N, 3.02. Found C, 62.40; H, 7.22; N, 3.03.
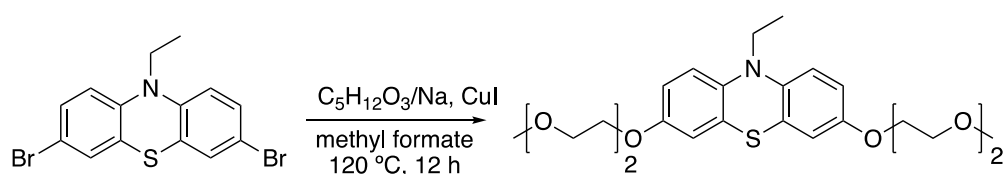
***N*-ethyl-3,7-bis(2-(2-methoxyethoxy)ethoxy)phenothiazine (B(MEEO)EPT)**, **Method II**. An oven-dried 350 mL pressure vessel was transferred to an argon-filled glove box. Diethylene glycol monomethyl ether (195 mL, 1.71 mol) was added into the pressure vessel, which was capped and removed from the glove box. Freshly cut sodium metal (4.78 g, 201 mmol) was dissolved in diethylene glycol monomethyl ether under nitrogen

atmosphere. Then, copper(I) iodide (15.8 g, 166 mmol), DBrEPT (8.00 g, 20.8 mmol) and methyl formate (3.1 mL, 33 mmol) were added to the resultant solution. After that reaction mixture was sparged with nitrogen for 15 min while stirring. The pressure vessel was tightly capped and immersed in an oil bath and heated to 120 °C for 12 h. Upon completion of the reaction, the reaction mixture was diluted with ethyl acetate and washed with 1.6 M aq. HCl (150 mL), water, and brine. The combined organic extracts were dried over magnesium sulfate and concentrated by rotary evaporation. Finally, organic residue was purified on a silica gel column, eluting with a gradient of 20-50% ethyl acetate in hexanes. The silica gel was neutralized with trimethylamine (2 -3 mL) during packing the column. The product was light yellowish red viscous liquid (6.8 g, 71%). ^{1}H NMR (DMSO-d$_6$, 400 MHz, ppm) δ 6.88 (d, J = 9.7 Hz, 2H), 6.79 – 6.75 (m, 4H), 4.05 – 3.98 (m, 4H), 3.79 (q, J = 6.9 Hz, 2H), 3.71 – 3.65 (m, 4H), 3.60 – 3.53 (m, 4H), 3.48 – 3.42 (m, 4H), 3.24 (s, 6H), 1.24 (t, J = 6.8 Hz, 3H). Anal. calcd. for C$_{24}$H$_{33}$NO$_6$S C, 62.18; H, 7.18; N, 3.02 Found C, 62.03; H, 6.96; N, 3.09.
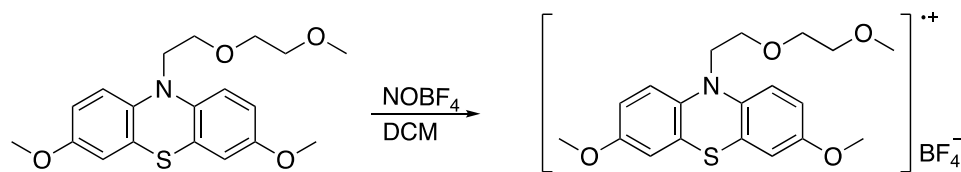
3,7-Dimethoxy-*N*-((2-methoxy)ethoxy)ethylphenothiazine **tetrafluoroborate** **(DMeOMEEPT-BF$_4$).** DMeOMEEPT (0.530 g, 1.38 mmol) was dissolved in anhydrous dichloromethane (15 mL) in an oven-dried 50 mL round-bottomed flask fitted with a rubber septum under nitrogen atmosphere. Then round-bottomed flask was placed in an ice water bath for 10 min after which nitrosonium tetrafluroborate (0.178 g, 1.52 mmol) was added into resultant reaction mixture and stirred 1 h. Upon completion of the reaction, anhydrous diethyl ether (25 mL) was added gradually with continued stirring, resulting in a blue precipitate. The precipitate was filtered under nitrogen, then it was redissolved in anhydrous dichloromethane (10 mL) and precipitated with anhydrous diethyl ether (20 mL). This process was repeated once more to remove unreacted starting material. The solid blue product (0.42 g, 65%) was dried under nitrogen and stored in a glove box.
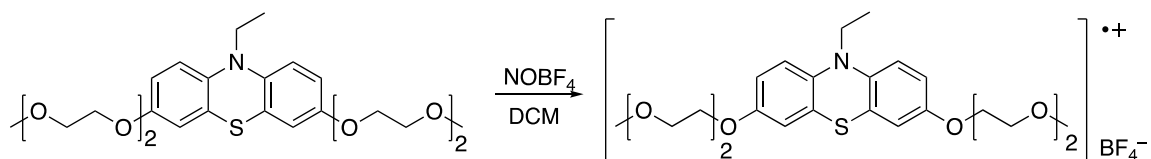
N-ethyl-3,7-bis(2-(2-methoxyethoxy)ethoxy)phenothiazine **tetrafluoroborate (B(MEEO)EPT-BF₄).** B(MEEO)EPT (8.0 g, 17 mmol) was dissolved in anhydrous dichloromethane (175 mL) in an oven-dried 500 mL round-bottomed flask fitted with a rubber septum under nitrogen atmosphere. Then reaction flask was placed in an ice water bath for 10 min after which nitrosonium tetrafluroborate (2.32 g, 19.9 mmol) was added to the reaction mixture, which was stirred for 1 h. Upon completion of the reaction, anhydrous diethyl ether (260 mL) was added gradually with continued stirring, which produced a blue precipitate. The precipitate was filtered under nitrogen, then redissolved in anhydrous dichloromethane (85 mL) and precipitated with the addition of anhydrous diethyl ether (120 mL). The redissolution/reprecipitation process was repeated once more to remove unreacted starting material. Finally, the solid blue product (4.9 g, 51%) was dried under nitrogen and stored in a glove box. To grow crystals of this product, a saturated solution of D(MEEO)EPT-BF₄ salt in DCM was prepared. A small volume was transferred in a NMR tube and layered it with toluene to form two distinct layers. Finally, the NMR tube was capped and placed in a freezer set at 4 ºC, and crystals formed at the interface of the solvents.
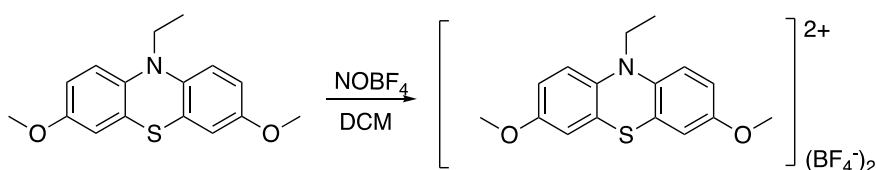
N-ethyl-3,7-dimethoxyphenothiazine **bis(tetrafluoroborate)** **(DMeOEPT(BF₄)₂).** DMeOEPT (0.30 g, 1.0 mmol) was dissolved in anhydrous dichloromethane (10 mL) in an oven-dried 50 mL round-bottomed flask fitted with a rubber septum under nitrogen atmosphere. Then round-bottomed flask was placed in an ice water bath for 10 min after which nitrosonium tetrafluroborate (0.32 g, 2.7 mmol) was added into resultant reaction mixture and stirred 1 h. Upon completion of the reaction, anhydrous diethyl ether (20 mL) was added gradually with continued stirring which produced a dark blue precipitate. The

precipitate was filtered under nitrogen, then it was redissolved in anhydrous dichloromethane (10 mL) and precipitated with anhydrous diethyl ether (20 mL). This process was repeated once more to remove unreacted starting material. The solid dark blue product (0.34 g, 72%) was dried under nitrogen and stored in a glove box.
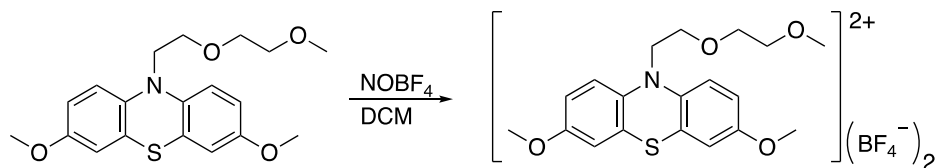
3,7-Dimethoxy-*N*-((2-methoxy)ethoxy)ethylphenothiazine bis(tetrafluoroborate) (DMeOMEEPT(BF₄)₂). DMeOMEEPT (0.40 g, 1.1 mmol) was dissolved in anhydrous dichloromethane (15 mL) in an oven-dried 50 mL round-bottomed flask fitted with a rubber septum under nitrogen atmosphere. Then a round-bottomed flask was placed in an ice water bath for 10 min after which nitrosonium tetrafluroborate (0.344 g, 2.95 mmol) was added into resultant reaction mixture and stirred 1 h. Upon completion of the reaction, anhydrous diethyl ether (25 mL) was added gradually with continued stirring, producing a dark blue precipitate. The precipitate was filtered under nitrogen, then it was redissolved in anhydrous dichloromethane (10 mL) and precipitated with anhydrous diethyl ether (20 mL). This process was repeated once more to remove unreacted starting material. The solid dark blue product (0.47 g, 79%) was dried under nitrogen and stored in a glove box.
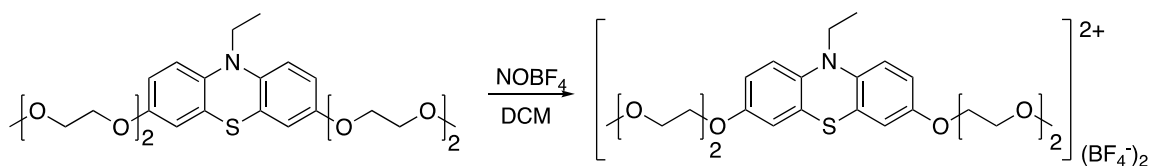
***N*-ethyl-3,7-bis(2-(2-methoxyethoxy)ethoxy)phenothiazine bis(tetrafluoroborate) (B(MEEO)EPT-(BF₄)₂).** B(MEEO)EPT (0.40 g, 0.90 mmol) was dissolved in anhydrous dichloromethane (10 mL) in an oven-dried 50 mL round-bottomed flask fitted with a rubber septum under nitrogen atmosphere. Then reaction flask was placed in an ice water bath for 10 min after which nitrosonium tetrafluroborate (0.28 g, 2.4 mmol) was added to the reaction mixture, which was then stirred for 1 h. Anhydrous diethyl ether (20 mL) was added gradually with continued stirring, producing a dark blue precipitate. The precipitate was filtered under nitrogen, then redissolved in anhydrous dichloromethane (10 mL) and

precipitated with anhydrous diethyl ether (20 mL). This process was repeated once more to ensure removal of unreacted starting material. Finally, the solid dark blue product (0.48 g, 83%) was dried under nitrogen and stored in a glove box.

3.5.2   UV-vis Spectroscopy

UV-vis of the three relevant states of oxidation of B(MEEO)EPT was recoded in ACN using optical glass cuvettes (Starna) with 10 mm path length on an Agilent 8453 diode array spectrophotometer. The radical cation/ dication solutions were prepared in anhydrous ACN and transferred into cuvettes inside an argon filled glovebox. The capped cuvettes were taken out from the glove box for spectral analysis.

3.5.3   X-Ray Crystallography

X-ray diffraction data were collected at 90.0 K on a Bruker D8 Venture kappa-axis diffractometer using MoK(alpha) X-rays. Raw data were integrated, scaled, merged and corrected for Lorentz-polarization effects using the APEX3 package.[5] Corrections for absorption were applied using SADABS.[6] The structure was solved by direct methods (SHELXT)[7] and refinement was carried out against F^2 by weighted full-matrix least-squares (SHELXL).[8] Hydrogen atoms were found in difference maps, but subsequently placed at calculated positions and refined using a riding model. Non-hydrogen atoms were refined with anisotropic displacement parameters. Atomic scattering factors were taken from the International Tables for Crystallography.[9]

3.5.4   Solubility

The solubilities of neutral molecules, their radical cation salts, and the dication salts of DMeOMEEPT and B(MEEO)EPT were determined in two different electrolyte solutions containing either 0.5 M tetraethylammonium tetrafluoroborate (TEABF$_4$, BASF, > 99%) or 0.5 M tetraethylammonium bis(trifluoromethane)sulfonamide (TEATFSI, IoliTec, > 99%), both dissolved in acetonitrile (ACN, BASF, 99.98%). As a result of the chemical oxidant used, the radical cation and dication salts contained a tetrafluoroborate

anion. A known amount of active material was added to a glass vial. Then, the electrolyte solution was added slowly, and the solution was stirred between additions. Electrolyte addition was continued until the active species was completely dissolved, as determined by visual inspection. This process was performed in triplicate for each active species, and the average molar concentrations were calculated.

3.5.5   Cyclic Voltammetry

All cyclic voltammetry (CV) measurements were performed in an argon-filled glovebox at 26 °C (ambient glovebox temperature) using a VSP-300 potentiostat (Bio-Logic). CV measurements were performed in 0.5 M TEATFSI/ACN with either a 3 mm diameter glassy carbon macroelectrode (CH Instruments, Inc.) or an 11 μm diameter carbon fiber microelectrode (CH Instruments, Inc.). Before each measurement, both working electrodes were polished on a MicroCloth pad containing an aqueous slurry of 0.05 μm alumina powder (Buehler Ltd.), rinsed with deionized water (Millipore), and wiped with lens paper. For all experiments, the counter electrode was a gold coil (CH Instruments, Inc), and a fritted Ag/Ag^+ electrode (fill solution: 0.1 M $AgBF_4$ [Alfa Aesar, 99%], 0.5 M TEATFSI, propylene carbonate [BASF, 99.98%]) was used as the pseudo reference electrode. To reference to the measured redox potentials to the ferrocenium/ferrocene redox couple, before each measurement, an additional CV was taken in the electrolyte containing 5 mM ferrocene (Sigma-Aldrich, 98%).

The macroelectrode was used to determine the redox potential (average of anodic and cathodic peak potentials), chemical reversibility (peak height ratio), and electrochemical reversibility (peak separation) of each redox event. Additionally, the diffusion coefficient of the bulk species was obtained using Randles-Sevcik analysis. Active materials were studied at 1 mM in the electrolyte, and 100% iR correction was applied. The cell resistance was determined using the ZIR technique (Biologic software package), which takes impedance measurements at a frequency of 200 kHz. The resistance measured was ca. 50 Ω, which leads to a correction of less than 0.1 mV for the largest measured currents. The diffusion coefficients were analyzed using the Randles-Sevcik equation with background current corrections, according to a published procedure:

$$i_p = 0.4463 \, nFAc \left(\frac{nFD}{RT} v \right)^{0.5}$$

where i_p is the peak current (A), n is the number of electrons transferred (-), F is the Faraday constant (96485 C mol^{-1}), A is the electrode area (cm^2), c is the concentration (mol cm^{-3}), D is the diffusion coefficient (cm^2 s^{-1}), R is the gas constant (8.314 J mol^{-1} K^{-1}), T is the absolute temperature (K), and v is the scan rate (V s^{-1}).[10] Data obtained from voltammograms at scan rates of 10, 20, 30, 40, 50, 75, and 100 mV s^{-1} were used for diffusion coefficient calculations.

The microelectrode was used to probe the electrolyte solutions before and after the symmetric flow cell cycling experiments to identify the species present (neutral, radical cation, dication). In these analyses the dominant species in the solution presents as the current plateau is closest to zero. The magnitude of the current plateau for a microdisc electrode is given by:

$$i_{ss} = 4nFrDc$$

where i_{ss} is the steady state plateau current (A) and r is the radius of the electrode (cm).[10] For all microelectrode experiments, the scan rate was 10 mV s^{-1}.

3.5.6 Symmetric Flow Cell Cycling

In this work, a custom-built small-volume flow cell with interdigitated flow fields was employed.[11] The backing plates were machined from polypropylene, which was chosen for its chemical compatibility with the materials used in this study. The flow fields were machined in-house from 3.18 mm thick impregnated graphite (product G347B, MWI Inc., Rochester, NY). The electrodes were cut to 1.7 cm × 1.5 cm dimensions from 190 ± 30 μm thick carbon paper (SGL 29 AA, SGL group, Wiesbaden, Germany) and used as received. On each side of the flow cell, two pieces of carbon paper were layered and compressed by ~20% during cell assembly. Daramic 175 was used as-received as the separator (Daramic LLC, Charlotte, NC). The cell was sealed using custom gaskets cut from polytetrafluoroethylene gasket tape (Goretex Tape, Gallagher Fluid Seals Inc., King of Prussia, PA). The geometric area of the cell was 2.55 cm^2. All flow cells were assembled

on the laboratory bench and then immediately transferred into an argon-filled glovebox (Innovative Technologies, O_2 < 10 ppm, H_2O < 0.1 ppm).

Perfluoroalkoxy alkane (PFA) jars (10 mL, Savillex) were used as electrolyte reservoirs and a peristaltic pump (Masterflex L/S Series) was used to recirculate the electrolyte at a constant volumetric flow rate of 10 mL min^{-1}. Norprene tubing (Masterflex) was used inside the pump head, and PFA tubing (Swagelok) connected the reservoirs to the flow cell. The Norprene tubing was attached to the PFA tubing with stainless steel compression fittings (Swagelok). The inner diameter of all tubing used was 1.6 mm. The electrolyte used in the flow cell studies consisted of 0.3 M B(MEEO)EPT-BF$_4$ and 0.5 M TEATFSI in ACN. This electrolyte has a theoretical capacity of 16.1 Ah L^{-1} (161 mAh), assuming two electron transfer events and 10 mL of electrolyte per side (20 mL total). Prior to cycling the symmetric flow cell, a constant current was applied to oxidize or reduce the B(MEEO)EPT-BF$_4$ (radical cation), such that the negative electrolyte was oxidized to B(MEEO)EPT-(BF$_4$)$_2$ (dication) and the positive electrolyte was reduced to B(MEEO)EPT (neutral). All cycling experiments were performed by applying a constant current density, which was determined from the geometric electrode area (2.55 cm^2). Data was collected using a VSP-300 potentiostat (BioLogic). Rate and stability studies were performed in the flow cell. For the rate study, which provides insight into the tradeoff between current density and accessed capacity, the current density was varied from 10 to 50 mA cm^{-2}, in increments of 10 mA cm^{-2}, for 5 cycles at each current density, and potential cutoffs of $\pm$ 0.775 V were imposed. The cell was then returned to its initial current density of 10 mA cm^{-2} for 5 additional cycles. This rate study was completed in a total time of 145 h. For the stability study, which provides information about species cyclability, the flow cell underwent constant current cycling for 140 cycles (460 h) at a current density of 25 mA cm^{-2}, with potential cutoffs of $\pm$ 0.775 V.

CHAPTER 4. A HIGH VOLTAGE PHENOTHIAZINE WITH STRATEGIC SUBSTITUENTS

This chapter is partially reproduced from "A Stable, Highly Oxidizing Radical Cation" by N. Harsha Attanayake, Aman Preet Kaur, T. Malsha Suduwella, Sean R. Parkin, and Susan A. Odom, which was published in New journal of Chemistry October 8, 2020. doi. 10.1039/D0NJ04434B. Reproduced by permission of The Royal Society of Chemistry (RSC) on behalf of the Centre National de la Recherche Scientfique (CNRS) and the RSC.

4.1   Summary

Highly reducing radical cation salts can be used as chemical oxidants in wide variety of applications. While some are commercial and others can be made, stability has been a problem with many of these organic-based reagents. We sought a method to increase the redox potentials of organic compounds to yield highly reducing radical cation salts that do not suffer the same instability as their triarylamine counterparts. Using phenothiazines, we (i) blocked the positions *para* to nitrogen with a substituent containing strong covalent bonds, using an electron-withdrawing group to increase oxidation potential, while at the same time (ii) introduced strain at the positions *ortho* to nitrogen to further raise the oxidation potential by preventing geometric relaxation of the oxidized state. Here we synthesized the phenothiazine derivative, *N*-ethyl-1,9-dimethyl-3,7-bis(trifluoromethyl)phenothiazine to test this hypothesis. Indeed, oxidation potentials reflect additive substituent effects, yielding a high-potential redox couple with a stable radical cation. Stability tests in solution and the solid state show that the radical cation form of this phenothiazine (SbCl$_6$ salt) is stable in inert conditions and can be used to oxidize other organic compounds in solution.

4.2   Introduction

The introduction of substituents on a redox-active core is a common method used to tailor oxidation and reduction potentials.[1-3] The degree of change vs. an original core can often be reliably predicted using Hammett constants, which quantify the degree of

electron donation or withdrawal.[3-4] A desire to create high oxidation potential redox couples for electronic and energetic applications has resulted in the synthesis of new materials that contain strongly electron-withdrawing groups.[1, 5] For example, in developing redox mediators for applications in electrochemical energy storage, our group and others have reported dialkoxybenzene,[5-8] TEMPO,[9-11] phenothiazine,[12-14] and triarylamine derivatives[15-17] that contain electron withdrawing groups as high potential materials for overcharge protection in lithium-ion batteries (LIBs), posolytes for redox flow batteries, and redox mediators for lithium-air batteries.

While the incorporation of electron-withdrawing groups can be used to reach high oxidation potentials, problems in stability can arise if these redox couples are employed in reducing environments.[5, 18] Otherwise stable redox couples often decompose if reduced to their radical anion forms.[18-19] For example, dialkoxybenzenes containing phosphonate substituents have oxidation potentials higher than 4 V vs. $Li^{0/+}$ (this corresponds to about 0.8 V vs. ferrocene/ferrocenium) were designed for overcharge protection of LIBs containing high voltage cathodes. Compared to their lower potential counterparts, their lifetimes in this application were dramatically reduced when employed in electrochemical cells containing highly reducing graphitic anodes.[19-20] However, in some cases, less reducing lithium titanate anodes resulted in prolonged lifetimes.[21] We suspected that reduction to the radical anion form in graphitic anode-containing cells was the cause of the limited lifetimes. Cyclic voltammetry of these derivatives shows that irreversible reduction events are accessible in the electrolyte window, whereas without the electron-withdrawing groups, reduction events were too low in potential to be observed. Our group has observed similar results in the development of high-potential phenothiazine derivatives that oxidize at or above 4 V vs. $Li^{0/+}$ (ca 0.8 V vs. $Cp_2Fe^{0/+}$).[1, 18] Clearly, a different strategy must be employed for the development of high potential redox couples that exhibit reductive stability. Apart from the applications in energy storage, the charged forms of stable, high-potential materials are of interest as chemical oxidants and as initiators in organic synthesis.[22-23] To be useful as a chemical oxidant, the neutral form of the aromatic compound should have a high oxidation potential and its charged species (radical cation) should have a high chemical stability in the solid phase (for storage purposes) as well as in solution phase (to perform redox reactions).[24-26]

An alternative method to modulating redox potentials is to vary conjugation in electronic materials.[27-28] This approach has been employed by altering dihedral angles between conjugated pi systems, such as polyphenylenes and polythiophenes, as well as twisting or bending a planar pi system, such as in twistacenes and fullerenes.[29-31] Often these changes are designed in neutral forms of the redox cores and are retained in their oxidized or reduced states. Recently, we found that a new approach could be used to tune oxidation potentials in a class of molecules called phenothiazines.[32] These heterocyclic fused-ring systems exhibit a bent geometry in their neutral form, and planarize upon oxidation. We found that preventing planarization of the oxidized form, without significantly altering the molecular geometry of the neutral form, resulted in an increase in oxidation potential, offering a route to high potential couples without requiring electron withdrawing groups.[32] In fact, even the use of electron-donating methyl groups, which usually lower oxidation potentials of conjugated molecules, raise the oxidation potentials of phenothiazines if placed appropriately.

Compared to a parent compound, N-ethylphenothiazine (EPT, Figure 4.1), a derivative containing methyl groups para to nitrogen, N-ethyl-3,7-dimethylphenothiazine (3,7-DMeEPT, Figure 4.1) has a lower oxidation potential, which is expected based on the electron-donating nature of methyl substituents. However, when the methyl groups are placed ortho to nitrogen, as with N-ethyl-1,9-dimethylphenothiazine (1,9-DMeEPT, Figure 4.1), the effect on oxidation potential is not only the opposite but is larger in magnitude. The impact is nearly as significant as the introduction of two trifluoromethyl groups para to nitrogen, as with N-ethyl-3,7-bis(trifluoromethyl)phenothiazine (3,7-BCF$_3$EPT, Figure 4.1). Oxidation potentials are provided in Table 4.2.

Seeking even higher redox potentials, we wondered whether the effects of electron-withdrawing groups (as in 3,7-BCF$_3$EPT)[33] and sterically hindering groups (as in 1,9-DMeEPT)[32] could be combined constructively to achieve this goal. It was unclear, for example, if the electron-withdrawing effect of the trifluoromethyl groups would be disrupted by the sterically hindering groups preventing relaxation, or would the effect be combined? To answer this question, we targeted a new compound, N-ethyl-1,9-dimethyl-3,7-bis(trifluoromethyl)phenothiazine (1,9-DMe-3,7-BCF$_3$EPT, Figure 4.1), incorporating methyl groups at the ortho positions for the steric effect and trifluoromethyl groups at the

para positions to harness their electron-withdrawing effect. Here we report the synthesis and characterization of this new derivative in comparison to the related compounds shown in Figure 4.1. Here we present the synthesis of this compound and comparisons to related structures and demonstrate its use as a shelf-stable chemical oxidant.
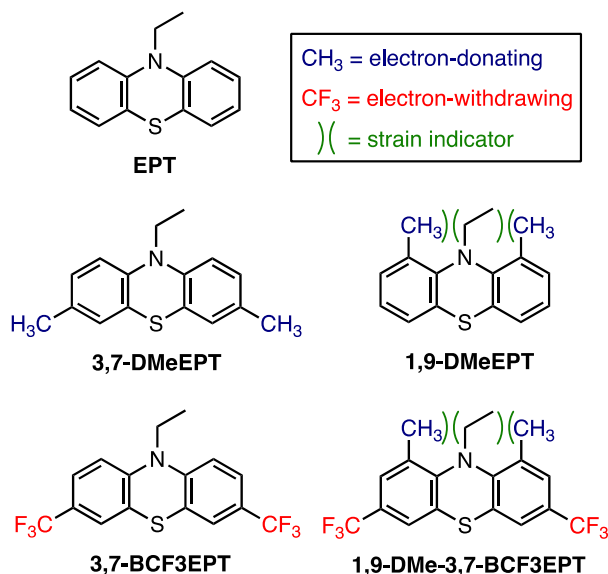
Figure 4.1. Representations of the chemical structures of *N*-ethylphenothiazine (EPT), *N*-ethyl-3,7-dimethylphenothiazine (3,7-DMeEPT), *N*-ethyl-1,9-dimethylphenothiazine (1,9-DMeEPT), *N*-ethyl-3,7-bis(trifluoromethyl)phenothiazine (3,7-BCF3EPT), and *N*-ethyl-1,9-dimethyl-3,7-bis(trifluoromethyl)phenothiazine (1,9-DMe-3,7-BCF3EPT). Image created by Prof. Susan Odom.

4.3   Results and Discussion

4.3.1   Synthesis

The synthesis of 1,9-DMe-3,7-BCF3EPT (Figure 4.2) was accomplished in three steps starting from 1,9-DMePT, which was synthesized following a previously reported procedure for the same compound.[32] Bromination of 1,9-DMePT produced intermediate 1,9-DMe-3,7-DBrPT, which was then alkylated to obtain 1,9-DMe-3,7-DBrEPT. Finally, 1,9-DMe-3,7-BCF3EPT was synthesized by treating 1,9-DMe-3,7-DBrEPT with a combination of potassium trifluoroacetate, copper (I) iodide, and cesium fluoride.
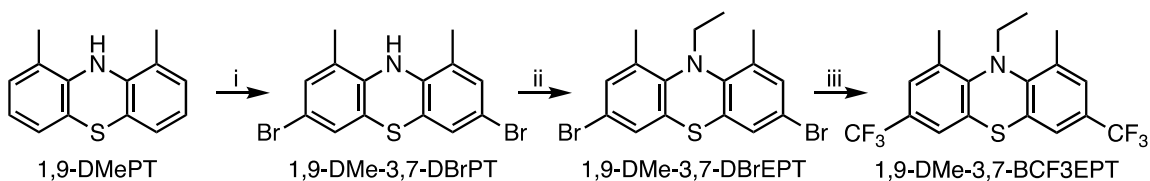
Figure 4.2. Synthetic route used to obtain 1,9-DMe-3,7-BCF₃EPT. i. Br₂, CH₃COOH, 24-36 h, r.t. (2.78 g, 51%), ii. a). NaH, DMF/THF, r.t., 30 min, b). CH₃CH₂Br, 80 °C, o/n, (2.15 g, 66%), iii. CF₃CO₂K, CuI, CsF, NMP/DMI, 180 °C, 48 h (0.62 g, 48%).

4.3.2   Crystal Structure Analysis

In addition to standard spectroscopic techniques, X-ray diffraction of single-crystals of 1,9-DMe-3,7-BCF₃EPT (Figure 4.3) provide further support of this product's identity. The thermal ellipsoid plot shows that this derivative is bent through the N and S atoms, with a butterfly angle of 140.5º. This angle is nearly identical to that of 1,9-DMeEPT (146.5º), which does not deviate significantly from derivatives containing para substituents, 3,7-DMeEPT (149.3º), and 3,7-BCF₃EPT (144.5-152.1º). All compounds are less bent than the unsubstituted parent EPT (136.8º), (Table 4.1, Figure 4.3). The main difference in geometries of the 1,9-dimethylated derivatives is in their radical cation forms.
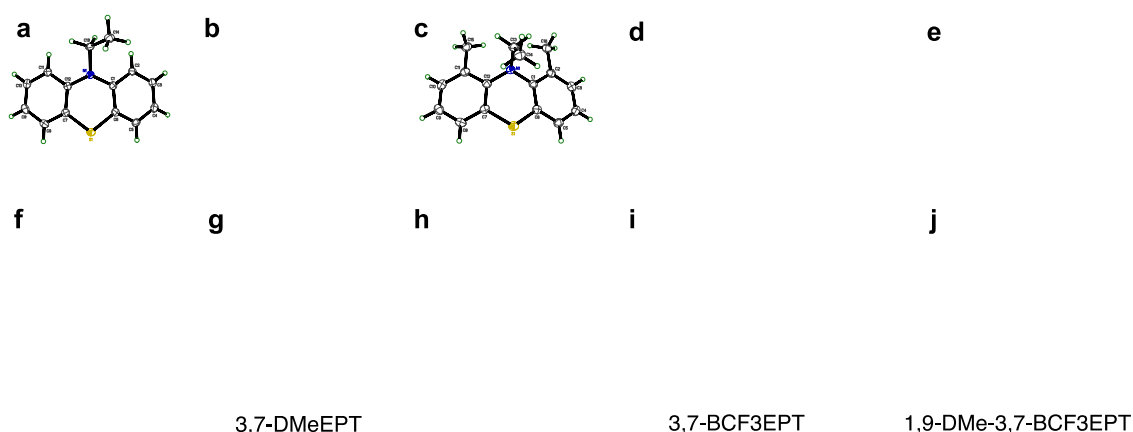
Figure 4.3. Thermal ellipsoid plot of neutral EPT (a), 3,7-DMeEPT (b), 1,9-DMeEPT (c), 3,7-BCF3EPT (d), and 1,9-DMe-3,7-BCF3EPT (e). Radical cation forms of EPT-SbCl6 (f), 3,7-DMeEPT-SbCl6 (g), 1,9-DMeEPT-SbCl6 (h), 3,7-BCF3EPT-SbCl6 (i), and 1,9-

DMe-3,7-BCF3EPT-SbCl6. Obtained by single crystal X-ray diffraction. Note: The unit cell for BCF3EPT contains two molecules and 3,7-DMeEPT-SbCl6 contains two SbCl6 anions; only one is displayed here. X-ray diffraction experiments performed by Dr. Sean R. Parkin.

To compare the geometries of radical cations with their neutral forms, we synthesized and isolated the radical cation salts of all EPT derivatives through chemical oxidation with antimony pentachloride ($SbCl_5$). The radical cation salts had antimony hexachloride ($SbCl_6^-$) as a counter ion. To confirm identity, we grew crystals of radical cation salts conducted analysis using X-ray diffraction. The thermal ellipsoid plots of radical cation salts are shown in Figure 4.3. In addition, we compared butterfly angles in these systems to results from density functional theory (DFT), as we know they are a reliable predictor of molecular geometries in this class of molecules. DFT calculations predict the radical cation butterfly angle for 1,9-DMe-3,7-BCF$_3$EPT to be 156.9º, which is similar to the computed value for the radical cation of 1,9-DMeEPT (156.6º). The isolated single-crystals of 1,9-DMe-3,7-BCF$_3$EPT and 1,9-DMeEPT radical cations show butterfly angles of 162.8º and 164.9º respectively, confirming that charged forms of strained phenothiazines remain bent. By contrast, the calculated butterfly angles of the radical cations of unstrained derivatives EPT, 3,7-DMeEPT, and 3,7-BCF$_3$EPT are significantly more planar; all lie between 171 and 172º, which are close to experimentally obtained values (174º to 175º). These results suggest that, like 1,9-DMeEPT, the geometric relaxation of the radical cation of 1,9-DMe-3,7-BCF$_3$EPT will be limited. The experimental and calculated butterfly angles are given in Table 4.1. The calculated adiabatic ionization potential (AIP) of 1,9-DMe-3,7-BCF$_3$EPT is consistent with this trend (Figure 4.4, Table 4.2). In fact, the AIP for 1,9-DMe-3,7-BCF$_3$EPT (7.22 eV, +0.74 eV vs. EPT at 6.48 eV) is almost the sum of the effect of the substituents on their simpler counterparts, 1,9-DMeEPT (6.68 eV, +0.20 eV vs. EPT) and 3,7-BCF$_3$EPT (7.06 eV, +0.58 eV vs. EPT). See Table 4.2 for AIP values.

Table 4.1. Comparing butterfly angles from DFT calculations and X-ray crystallography for all compounds in their neutral and radical cation forms. DFT calculations were performed at the B3LYP/6-311G(d,p) level of theory. The radical cations salts were grown with hexachloroantimonate ($SbCl_6^-$) as the counter ion. X-ray diffraction results from Dr. Sean Parkin. DFT calculations were performed by Corrine F. Elliott.

Compound	Butterfly angles [°] (neutral)		Butterfly angles [°] (radical cation)	
	DFT	experimental	DFT	experimental
EPT	138.7[a]	136.8[a]	171.4[a]	174.8[a]
3,7-DMeEPT	138.8[a]	149.3[a]	171.1[a]	174.9
1,9-DMeEPT	143.1[a]	146.5[a]	156.6[a]	164.9
3,7-BCF$_3$EPT	139.7[a]	144.5-152.1[a,b]	171.1[a]	164.5[a]
1,9-DMe-3,7-BCF$_3$EPT	142.8	140.5	156.9	162.8

[a] Ref. 32, [b] Multiple molecules in asymmetric unit.
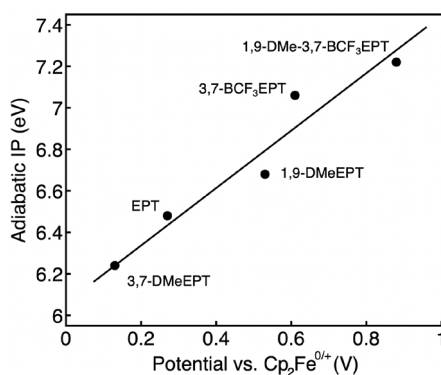
Figure 4.4. Plot of calculated AIPs vs. half-wave oxidation potentials. The equation for the line of best fit, $y = 0.7039x - 4.257$, has an R^2 value of 0.94. DFT calculations were performed by Corrine F. Elliott.

4.3.3 Electrochemical Analysis

Cyclic voltammetry (CV) was performed to determine the half-wave oxidation potential and chemical reversibility of 1,9-DMe-3,7-BCF$_3$EPT. This experiment was done in 0.1 M tetrabutylammonium hexafluorophosphate (nBu$_4$NPF$_6$) in DCM. A cyclic voltammogram of 1,9-DMe-3,7-BCF$_3$EPT is shown in Figure 4.5. It shows a first reversible oxidation and a second irreversible oxidation (Figures 4.5a-b). No reduction event was observed. The first oxidation, at 0.88 V vs. Cp$_2$Fe$^{0/+}$ at 0 V, is the highest in the series of compounds studied. Compared to EPT ($E_{1/2}^{0/+} = 0.27$ V vs. Cp$_2$Fe$^{0/+}$), the oxidation potential of 1,9-DMeEPT ($E_{1/2}^{0/+} = 0.53$ V vs. Cp$_2$Fe$^{0/+}$) is 0.26 V higher, and that of 3,7-BCF$_3$EPT ($E_{1/2}^{0/+} = 0.61$ V vs. Cp$_2$Fe$^{0/+}$) is 0.34 V higher. The oxidation potential of 1,9-DMe-3,7-BCF$_3$EPT is nearly identical to what would be predicted by simply combining the effects of the ortho methyl substituents and para trifluoromethyl substituents (0.87 V vs. Cp$_2$Fe$^{0/+}$), supporting the proposition that the effect of the substituents is indeed additive. These values are in good agreement with the calculated

AIPs, as shown in a plot of AIP vs. $E_{1/2}^{0/+}$ (Figure 4.4), for which a line of best fit has an R^2 value of 0.94.
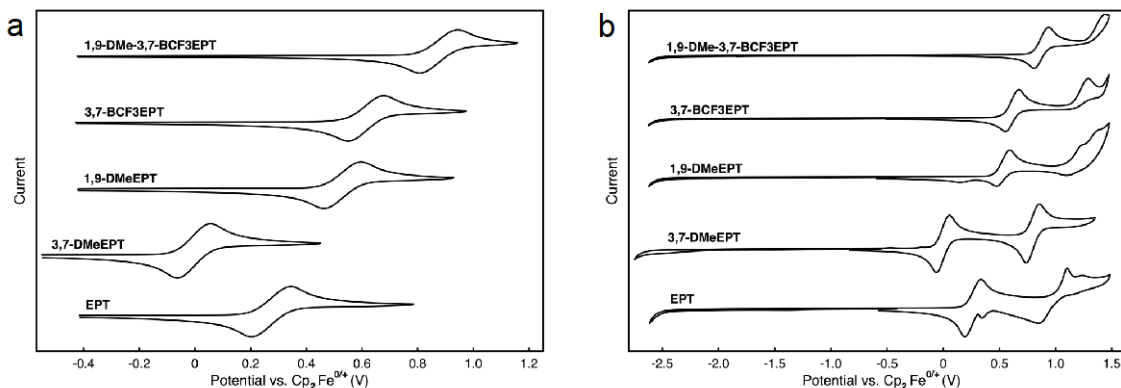
Figure 4.5. Cyclic voltammograms of the first oxidation event (a), and full window (b) of EPT, 3,7-DMeEPT, 1,9-DMeEPT, 3,7-BCF3EPT, and 1,9-DMe-3,7-BCF3EPT at 1 mM in 0.1 M nBu4NPF6 in DCM, recorded at a scan rate of 100 mV/s. Voltammograms were calibrated to $Cp_2Fe^{+/0}$ at 0 V, using ferrocene (Cp_2Fe) or decamethylferrocene (Cp^*_2Fe) as an internal reference. Cyclic voltammetry experiments performed by Dr. Aman Preet Kaur.

The first oxidation is chemically reversible in this electrolyte, as evidenced by the ratio of forward to reverse current (Ipa/Ipc) of 1.05 (Table 4.2). Variable scan rate voltammograms (Figure 4.6) were performed to determine values of the diffusion coefficients of the neutral and radical cations, determined from Randles-Sevcik plots (Figure 4.6). The diffusion coefficient for neutral 3,7-DMeEPT, 3,7-BCF$_3$EPT, and 1,9-DMe-3,7-BCF$_3$EPT are nearly the same, and are all slower than derivatives without para substituents. However, the case of the radical cations is more variable, with rates increasing as follows: 1,9-DMe-3,7-BCF$_3$EPT < 3,7-DMeEPT < 3,7-BCF$_3$EPT < 1,9-DMeEPT < EPT. While the derivatives without para substituents again have the highest diffusion coefficients, the substituent positions are not enough to explain the trend. Perhaps two trends are competing, such as molecular shape and charge distribution, both of which could affect the solvation spheres.
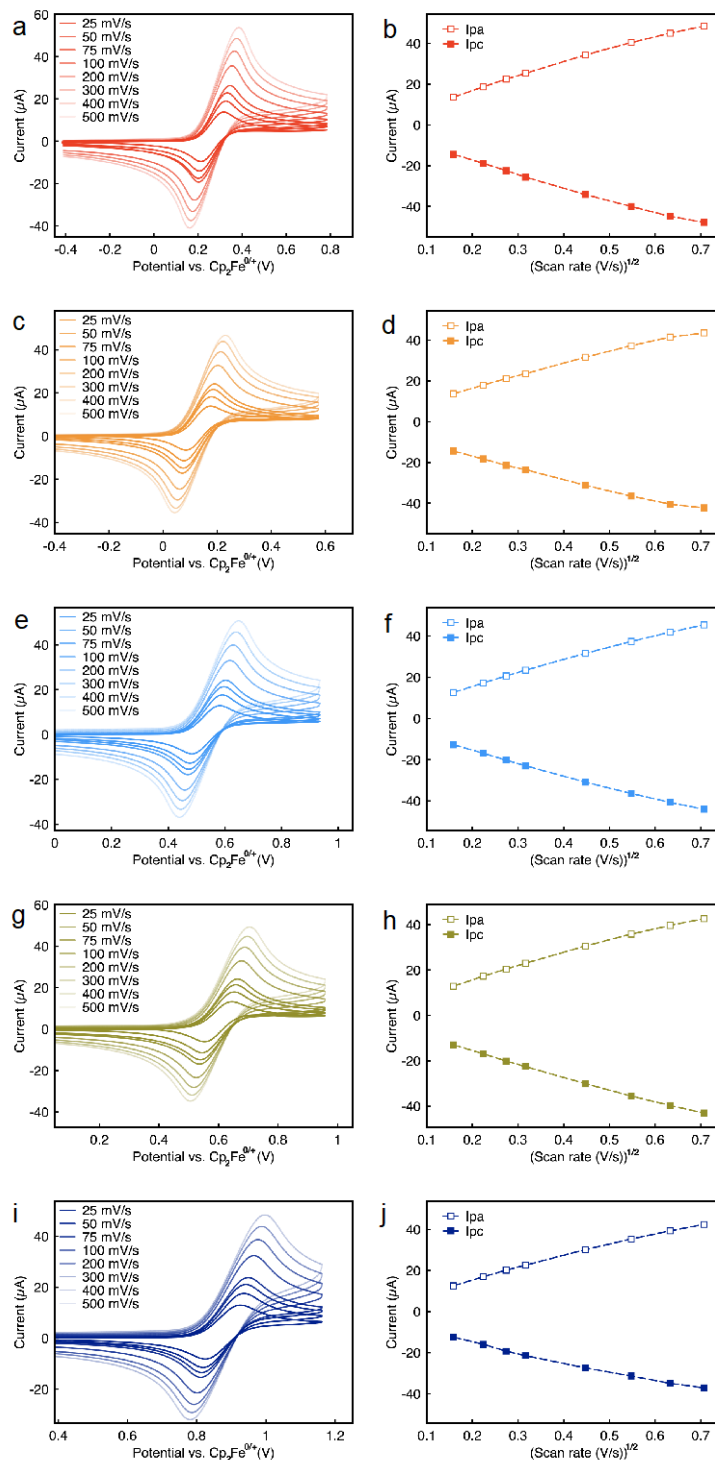
Figure 4.6. Cyclic voltammograms of 3,7-DMeEPT (a), EPT (c), 1,9-DMeEPT (e), and 3,7-BCF₃EPT (g) at 1 mM in 0.1 M nBu₄NPF₆/DCM at scan rates of 25, 50, 75, 100, 200, 300, 400 and 500 mV s⁻¹. Additionally, the corresponding Randles-Sevcik plots are shown for 3,7-DMeEPT (b), EPT (d), 1,9-DMeEPT (f), and 3,7-BCF₃EPT (h).

4.3.4 Solution Phase Stability

Given that the first oxidation event was reversible on the CV time scale, at scan rates 25 mV/s, we wanted to further evaluate the stability of the radical cation form of 1,9-DMe-3,7-BCF$_3$EPT, as radical cations are generally the more reactive form of a neutral/radical cation couple. For this purpose, we used the chemically synthesized and isolated radical cation salts of all EPT derivatives to examine the stability of the charged species. The thermal ellipsoid plots of isolated crystals of the radical cation salts are shown in Figure 4.3. The isolation of X-ray quality crystals of radical cations confirms the substantial stability of the charged forms, especially the strained 1,9-dimethylated strained phenothiazine derivatives. To further evaluate the chemical stability of the radical cation forms in solution phase, we analyzed samples using UV-vis spectroscopy. We began with a solution of radical cation salts in 0.2 mM concentration in anhydrous DCM using 10 mm path length cuvettes (Figures 4.7b-c). The absorption spectra of the neutral compounds (Figure 4.7a) do not overlap with the regions of interest for the radical cations (Figure 4.7b), where distinctive features are observed. In the neutral forms, the absorption spectra of the derivatives containing ortho substituents to N are blue shifted compared those that do not. Likewise, differences in the radical cation spectra are observed based on whether compounds contained ortho substituents. Specifically, the unstrained compounds exhibit features in close proximity and intensity in the region from 400-600 nm. However, the radical cations of strained 1,9-DMeEPT and 1,9-DMe-3,7-BCF$_3$EPT lack the finer structure in the lower energy region and instead show a broad absorption, and each exhibits a similarly shaped, more intense absorption feature between 500 and 600 nm that lacks the definition observed in the unstrained equivalents (Figure 4.7b).

Table 4.2. Adiabatic ionization potentials (AIP) from density functional theory calculations performed with the B3LYP functional at the 6-311g(d,p) level of theory, half-wave first oxidation potentials ($E_{1/2}^{0/+}$) vs. $Cp_2Fe^{0/+}$, peak current ratios for $E_{1/2}^{0/+}$, and diffusion coefficients of neutral and radical cation forms of EPT, 3,7-DMeEPT, 1,9-DMeEPT, 3,7-BCF$_3$EPT, 1,9-DMe-3,7-BCF$_3$EPT, from electrochemical measurements performed at 1 mM in 0.1 M nBu$_4$NPF$_6$ in DCM. Absorption maxima for the neutral and radical cation forms in DCM. DFT calculations were performed by Corrine F. Elliott.

Compound	AIP (eV)	$E_{1/2}^{0/+}$ (V) vs. $Cp_2Fe^{0/+}$	Peak Current Ratio (Ipa/Ipc)	Diffusion Coefficient ($\times 10^{-5}$ cm^2/s) neutral	radical cation	Absorption maxima (nm)* neutral	radical cation
EPT	6.48[a]	0.27	0.99	1.12	1.05	312	**516,** 692, 774, 865
3,7-DMeEPT	6.24[a]	0.13	1.00	0.86	0.75	316	**552,** 695 760, 852
3,7-BCF$_3$EPT	7.06[a]	0.61	1.02	0.81	0.83	319	**446,** 499, 695 760, 847
1,9-DMeEPT	6.68[a]	0.53	1.02	0.98	0.91	298	394, **574,** 965
1,9-DMe-3,7-BCF$_3$EPT	7.22	0.88	1.05	0.81	0.52	308	392, **545,** 945

[a] Ref. 32, *The most intense peak is bolded.

We monitored the shape and intensity changes of radical cation absorption spectra for 5 h after dissolving the isolated salts in anhydrous DCM at 0.2 mM (Figures 4.8a-e). Plotted in Figure 4.8f are the values for absorption intensity at maximum absorbance vs. time. For the unstrained derivatives as well as strained 1,9-DMeEPT, negligible loss in intensity was observed. However, for strained 1,9-DMe-3,7-BCF$_3$EPT, the intensity decreased by ca. two thirds over 5 h. Notably, in all cases, the shapes of the absorption spectra remained similar regardless of retention or loss in intensity (Figures 4.8a-e). We pondered the reason for the decay in absorbance intensity for 1,9-DMe-3,7-BCF$_3$EPT. No precipitate was observed in the cuvette, which led us to conclude that the compound was either being transformed into a new species via covalent bond cleavage/formation or underwent an electron-transfer reaction/self-discharge with the solvent and returned to its neutral form.
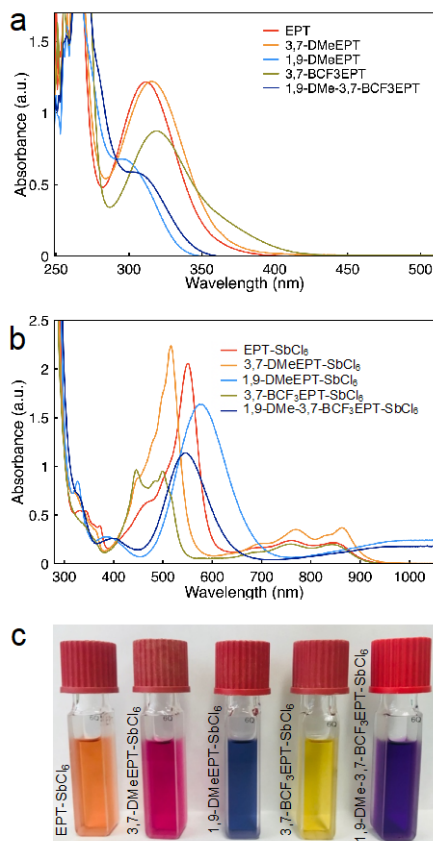
Figure 4.7. UV-vis absorption spectra of EPT, 3,7-DMeEPT, 1,9-DMeEPT, 3,7-BCF$_3$EPT and 1,9-DMe-3,7-BCF$_3$EPT in their neutral (a), and radical cation form (b) at 0.20 mM (a), and a photograph of cuvettes containing solutions of the radical cations dissolved in DCM and filled in 10 mm path length cuvettes (c). The radical cation salts had antimony hexachloride (SbCl$_6^-$) as a counter ion. UV-vis absorption spectra were recorded using 10 mm path length quartz cuvettes.

To determine whether the radical cation decomposed and/or underwent electron transfer more rapidly the low (0.2 mM) concentration employed due to trace impurities present in the solvent, we performed another UV-vis experiment at three elevated concentrations. Figures 4.9a-c show the absorption spectra vs. time for three concentrations of radical cation form of 1,9-DMe-3,7-BCF$_3$EPT at 1, 5, and 1 mM in anhydrous DCM. We analyzed the radical cation salt at these elevated concentrations by using a shorter path length cuvette (2 mm) and by accepting that the absorption spectra of the 5 and 1 mM solution would saturate the detector at the most intense absorption region of radical cation (450-650 nm).

Therefore, we monitored the absorption intensity changes in the low energy region (951 nm) for all concentrations. If trace impurities are responsible for an electron-transfer

95

reaction that causes the radical cation of 1,9-DMe-3,7-BCF$_3$EPT to transform into its neutral form more rapidly at lower concentrations, and if impurities are acting as reagents rather than catalysts, then at a sufficiently high concentration, the rate of radical cation loss over time should be much lower.[44] As shown in Figure 4.9d, radical cations decayed at a faster rate during the first hour compared to rest of 4 hours, which might indicate that radical cations react with most of the trace solvent impurities just after dissolution. It appears that (Figure 4.9d) radical cations are more persistent in the solution when moving from 1 mM to 10 mM concentration and the rate of decay is inversely proportional to the concentration. This result offers promise for higher stability and less material decomposition at elevated concentrations in solution phase, as we speculated.
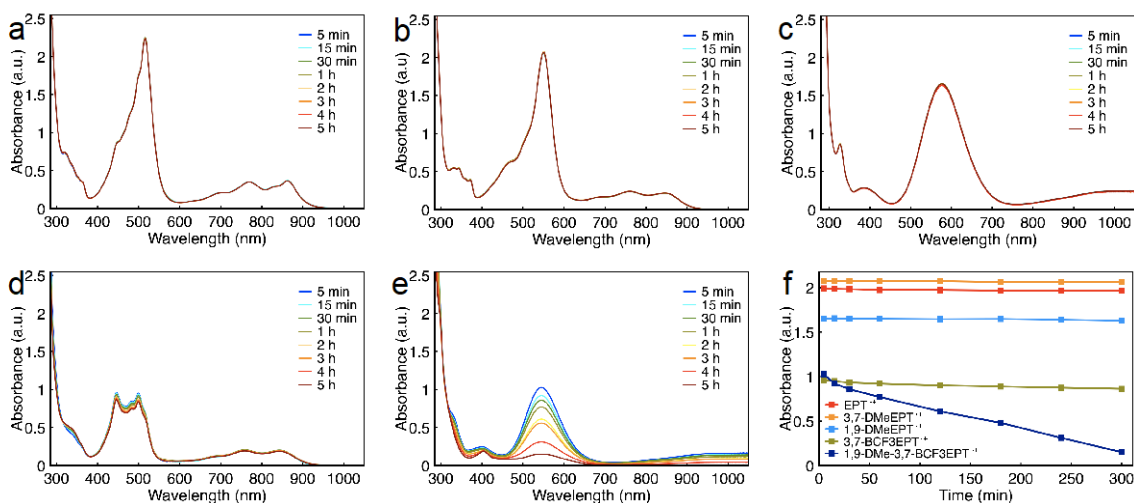
Figure 4.8. UV-vis absorption spectra of EPT-SbCl$_6$ (a), 3,7-DMeEPT-SbCl$_6$ (b), 1,9-DMeEPT-SbCl$_6$ (c), 3,7-BCF$_3$EPT-SbCl$_6$ (d), and 1,9-DMe-3,7-BCF$_3$EPT-SbCl$_6$ (e), radical cations at 0.2 mM in DCM, and a plot of absorbance vs. time for radical cations in DCM (f), collected at 5,15, 30, 60, 120, 180, 240, and 300 min. The absorption intensity was monitored at absorption maxima of each radical cation (provided in Table 4.2). UV-vis absorption spectra were recorded using 10 mm path length quartz cuvettes. UV-vis experiments performed by Thilini Malsha Suduwella.
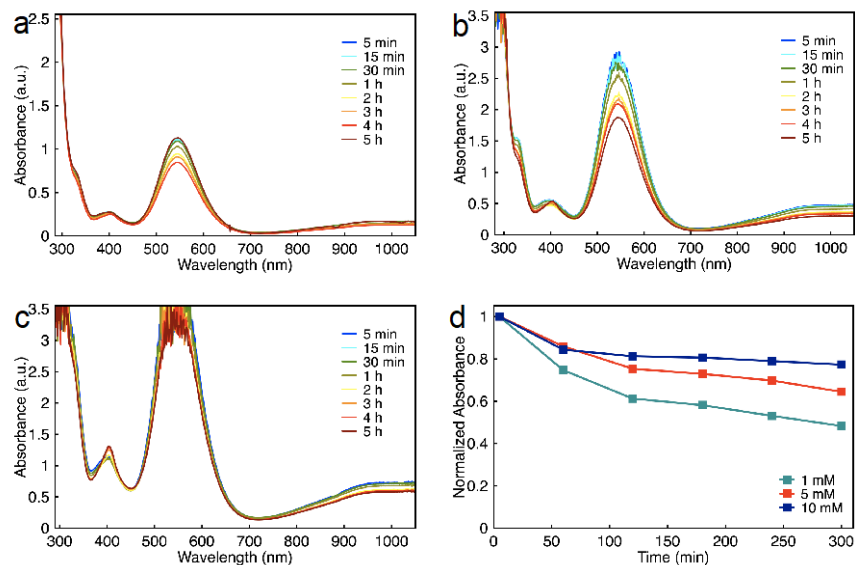
Figure 4.9. UV-vis absorption spectra of 1,9-DMe-3,7-BCF$_3$EPT-SbCl$_6$ radical cation salts at 1 mM (a), 5 mM (b), 10 mM (c), in DCM, and a plot of normalized absorbance (at 951 nm) vs. time for radical cations at each concentration (d), collected at 5,15, 30, 60, 120, 180, 240, and 300 min. UV-vis absorption spectra were recorded using 2 mm path length quartz cuvettes.

4.3.5 Solid Phase Stability

As the radical cation form of 1,9-DMe-3,7-BCF$_3$EPT shows a significant chemical stability at a higher concentration (10 mM) in solution, we sought to analyze the radical cation stability in the solid state to evaluate this material as a stable chemical oxidant. In general, radical cations can be generated using a few different techniques including bulk electrolysis, irradiation with gamma rays, and reaction with a chemical oxidant.[24, 45-46] Of these methods, chemical oxidants is quite simple. The chemical radical cation generation process is an electron transfer reaction where the oxidant accepts an electron from the neutral compound, thereby generating the radical cation form. For a compound to serve as a chemical oxidant, it is necessary that the oxidation potential of neutral form of the chemical oxidant be than the neutral form of molecule to be oxidized. As 1,9-DMe-3,7-BCF$_3$EPT shows the highest oxidation potential ($E_{1/2}^{0/+}$ = 0.88 V vs. Cp$_2$Fe$^{0/+}$) among molecules in this study, its radical cation form should be able to chemically oxidize all phenothiazine derivatives, ranging from the lowest oxidation potential 3,7-DMeEPT

($E_{1/2}^{0/+}$ = 0.13 V vs. $Cp_2Fe^{0/+}$) to the next highest oxidation potential 3,7-BCF₃EPT ($E_{1/2}^{0/+}$ = 0.61 V vs. $Cp_2Fe^{0/+}$).

For this purpose, 1,9-DMe-3,7-BCF₃EPT-SbCl₆ was freshly synthesized and stored under two different conditions to examine its shelf life stability in the solid state for three weeks: (i) stored in a glass vial inside an argon filled glove box, and (ii) stored in a glass vial on the bench top. In addition to the radical cations of 1,9-DMe-3,7-BCF₃EPT, we analyzed the shelf life stability of freshly synthesized EPT-SbCl₆ as a control. As shown in Figures 4.10b, e-f (1,9-DMe-3,7-BCF₃EPT-SbCl₆) and Figures 4.10a, c-d (EPT-SbCl₆), the UV-vis spectra of radical cation samples were recorded on days 0, 7, 14, and 21 after freshly preparing radical cation solutions in anhydrous DCM. We analyzed 1,9-DMe-3,7-BCF₃EPT radical cation at 1 mM in 2 mm pathlength cuvettes.
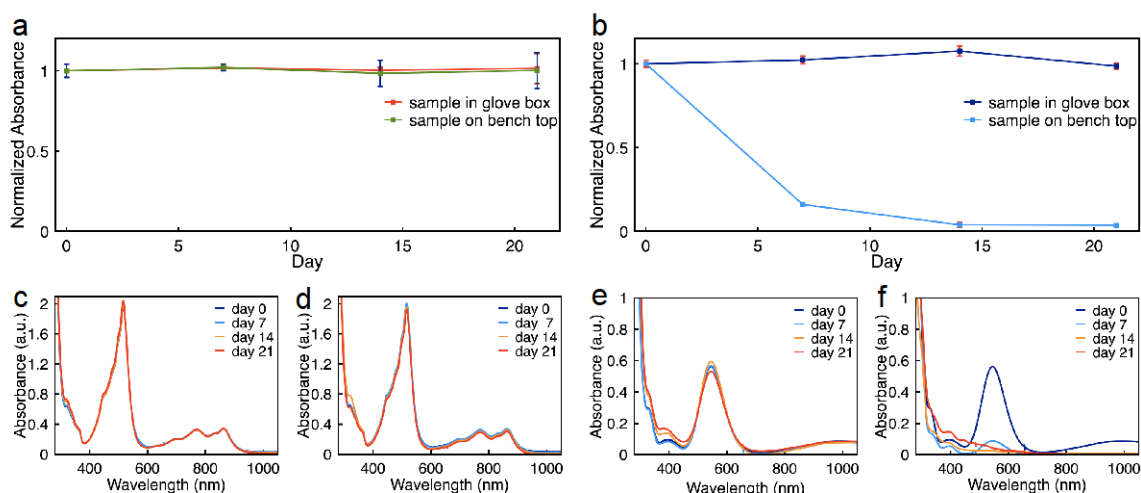
Figure 4.10. Solid state stability of EPT-SbCl₆ and 1,9-DMe-3,7-BCF3EPT-SbCl₆ on day 0, 7, 14, and 21 following storage in glass vials, placed in an argon filled glove box in light and on a bench top in light. Normalized absorbance intensity at 516 nm vs. time for EPT-SbCl₆ (a) and normalized absorbance intensity at 545 nm vs. time for 1,9-DMe-3,7-BCF3EPT-SbCl₆ (b). UV-vis absorption spectra of EPT-SbCl₆ stored in an argon filled glove box (c), on a bench top (d) at 0.2 mM in DCM and 1,9-DMe-3,7-BCF3EPT-SbCl₆ stored in the glove box (e), on bench top (f) at 1 mM in DCM. UV-vis absorption spectra of EPT-SbCl₆ was recorded using 10 mm path length quartz cuvettes and 1,9-DMe-3,7-BCF3EPT-SbCl₆ was recorded using 2 mm path length quartz cuvettes.

EPT-SbCl₆ stored in the glove box and on the benchtop remained stable over three weeks without showing new peaks or without losing absorption intensity on UV-vis spectra (Figures 4.10c-d). The plot of normalized absorbance intensity at maximum absorbance vs. time of the EPT radical cation (Figure 4.10a) shows, it is stable in solid state for three

weeks, regardless of the exclusion of water and oxygen or not. 1,9-DMe-3,7-BCF₃EPT-SbCl₆ showed environment-dependent stability. Although, the sample stored in the glove box remained similarly stable to EPT-SbCl₆ (Figure 4.10e), the one kept on the benchtop decomposed significantly in the solid state (Figure 4.10f). The loss of absorbance intensity is evident in the spectrum shown in Figure 4.10f; the change in spectral shape indicates that 1,9-DMe-3,7-BCF₃EPT-SbCl₆ is sensitive to atmospheric moisture and/or air. However, its stability is greater than that of Magic Blue (MB, tris(4-bromophenylaminium)hexachloroantimonate), a commercially available chemical oxidant that has been employed as a one-electron oxidant in various fields,[47-48] is also known that to decompose in the solid state – even upon storage in an inert atmosphere, generating byproducts called the "blues brothers", by dimerizing through its labile C-Br bonds.[49-50] This not only prevents the accuracy of the quantitative analysis of the oxidation process, but also may mislead the spectroscopic analysis. However, 1,9-DMe-3,7-BCF₃EPT-SbCl₆ is at least as stable in an inert environment in the solid state, perhaps due to its strong covalent bonds. We suspect that 1,9-DMe-3,7-BCF₃EPT-SbCl₆ decomposed in ambient conditions due to the formation of sulfoxide or sulfones compounds by reacting with atmospheric oxygen.

4.4 Conclusions

Here we showed that the combination of electron-donating groups positioned at locations that prevent the relaxation of the radical cation form, in combination with electron-withdrawing groups at unstrained positions, have an additive effect on the oxidation potential of phenothiazines compared to derivatives having only one type of substituent. The oxidation potential of both strained and electron-withdrawing substituents resulted in the creation of a new high-potential redox couple with different electronic structure compared to its unstrained counterparts. The first oxidation event of the neutral compound is reversible by cyclic voltammetry at scan rates from 25 to 500 mV/s. Importantly, the introduction of substituents to create this high-potential couple did not bring the reduction event into the solvent window. This result highlights a key advantage of this approach over introduction of more electron-withdrawing groups to raise oxidation potentials, which – if sufficiently electron-withdrawing – bring the first reduction event,

which is irreversible, into the solvent window. This feature may allow for strained phenothiazines to be used in applications that involve highly reducing environments.

4.5 Experimental

4.5.1 Synthesis

Materials

Potassium trifluoroacetate, copper (I) iodide, and cesium fluoride were purchased from Sigma Aldrich. Sodium hydride (60% dispersion in mineral oil), magnesium sulfate, N-methylpyrrolidone (NMP), 1,3-dimethyl-2-imidazolidinone (DMI), sodium sulfite, potassium hydroxide and antimony pentachloride (SbCl$_5$) were purchased from Acros Organics. Bromine, acetic acid, and tetrabutylammonium hexafluorophosphate (nBu$_4$NPF$_6$) were purchased from Sigma Aldrich. Anhydrous dichloromethane (DCM), anhydrous tetrahydrofuran (THF), and anhydrous N,N-dimethylformamide (DMF) were purchased from VWR and stored in a solvent purification system (L.T. Technologies). Silica gel used for column chromatography was purchased from Sorbent Technologies. Ethyl acetate and hexanes for column chromatography were purchased from Avantor Performance Materials. Solvents used for NMR spectroscopy were obtained from Cambridge Isotope Laboratories. ^{1}H, ^{19}F and ^{13}C NMR spectra were obtained on a 400 MHz Varian NMR spectrometer. ^{19}F NMR, chemical shifts are reported vs. CFCl$_3$ at 0 ppm by adjusting the chemical shift of hexafluorobenzene (Alfa Aesar), used as an internal reference, to -164.9 ppm. Mass spectra were obtained on an Agilent 5973 Network mass selective detector attached to Agilent 6890N Network GC system. Elemental analyses were performed by Atlantic Microlab, Inc.

4.5.2 Synthesis

N-ethylphenothiazine (EPT),[34] N-ethyl-3,7-dimethylphenothiazine (3,7-DMeEPT),[35] N-ethyl-3,7-bis(trifluoromethyl)phenothiazine (BCF$_3$EPT),[35] bis(o-tolyl)amine, 1,9-dimethylphenothiazine (1,9-DMePT), N-ethyl-1,9-dimethylphenothiazine

(1,9-DMeEPT),[36] and *N*-ethylphenothiazine antimonyhexachloride (EPT-SbCl$_6$),[24] were synthesized as previously reported.

3,7-Dibromo-1,9-dimethylphenothiazine (1,9-DMe-3,7-DBrPT). In an oven-dried 250 mL round-bottomed flask under nitrogen atmosphere, 1,9-DMePT (3.25 g, 14.3 mmol) was dissolved in anhydrous acetic acid (100 mL). A solution of bromine (2.12 mL, 41.5 mmol) in acetic acid (15 mL) was slowly transferred into the reaction mixture using an addition funnel. Then the reaction mixture was stirred in room temperature for a day until consumption of starting materials. Sodium sulfite (1.22 g, 2.02 mmol) was added into reaction mixture and stirred for 2 h till get a gray solution. After that reaction mixture was transferred into a 1 L beaker. Potassium hydroxide (2.51 g, 42.9 mmol) was dissolved in deionized water (100 mL) and the volume was raised to 300 mL after adding ice. This solution was poured into the reaction mixture and stirred using a glass rod, yielding a gray precipitate, which was filtered, rinsed with more deionized water, then dried overnight in a vacuum oven (50 °C, -0.1 MPa). Finally, the solid product was crystallized from ethanol, yielding the product as a gray crystalline solid (2.78 g, 51%). ^{1}H NMR (400 MHz, DMSO-d$_6$) δ 7.18 (m, 2H), 7.09 (m, 2H), 6.85 (s, 1H), 2.25 (s, 6H). ^{13}C NMR (100 MHz, CDCl$_3$) δ 138.9, 133.3, 133.0, 131.7, 127.2, 114.3, 16.8. GCMS: m/z 385 (100%), 383 (91%), 304 (37%), 302 (34%), 224 (38%), 192 (12%), 180 (8%), 111(10%). Anal. Calcd. for C$_{14}$H$_{11}$Br$_2$NS: C, 43.66; H, 2.88; N, 3.64. Found C, 43.85; H, 2.97; N, 3.63.

3,7-Dibromo-*N*-ethyl-1,9-dimethylphenothiazine (1,9-DMe-3,7-DBrEPT). In an oven-dried 250 mL round-bottomed flask under nitrogen atmosphere, 1,9-DMe-3,7-DBrPT (3.00 g, 7.80 mmol) was dissolved in a solution of anhydrous DMF (60 mL) and anhydrous THF (60 mL). Sodium hydride (0.78 g, 60 wt.% in mineral oil, 20 mmol) was added at room temperature, and the reaction mixture was stirred for 30 min. After that bromoethane (1.02 g, 48.6 mmol) was added to the reaction mixture and round bottom flask was equipped with a reflux condenser. Then the reaction mixture was refluxed by heating in an oil bath at 90 °C for 12 h. After completion the reaction, reaction mixture was cooled to room temperature and quenched with water. The organic product was extracted with ethyl acetate, and it was washed with brine and dried over MgSO$_4$. The organic extracts were filtered and concentrated by rotary evaporation. The resulting organic crude was purified

by silica gel column chromatography using a gradient of 0–4% ethyl acetate in hexanes as eluent, yielding the product as a white solid (2.15 g, 66%). ^{1}H NMR (400 MHz, DMSO-d_6) δ 7.41 – 7.31 (m, 4H), 3.39 (q, J = 7.0, 2H), 2.34 (s, 6H), 0.95 (t, J = 7.1, 3H). ^{13}C NMR (100 MHz, CDCl$_3$) δ 142.9, 135.9, 135.8, 132.2, 127.1, 117.4, 49.6, 18.2, 14.1. GCMS: m/z 413 (23%), 384 (100%), 382(54%), 304 (8%), 223 (10%). Anal. Calcd. for C$_{16}$H$_{15}$Br$_2$NS: C, 46.51; H, 3.66; N, 3.39. Found C, 46.59; H, 3.82; N, 3.34.

N-ethyl-1,9-dimethyl-3,7-bis(trifluoromethyl)phenothiazine (1,9-DMe-3,7-BCF$_3$EPT). 1,9-DMe-3,7-DBrEPT (1.25 g, 3.03 mmol) and copper(I) iodide (4.61 g, 24.2 mmol) were added into an oven dried 100 mL pressure vessel under nitrogen atmosphere. The pressure vessel was transferred to an argon filled glove box, then potassium trifluoroacetate (2.76 g, 18.2 mmol) and cesium fluoride (0.99 g 6.5 mmol) were added into the pressure vessel and removed from the glove box. N-Methylpyrrolidinone (NMP) (44 mL) and 1,3-dimethyl-2-imidazolidinone (10 mL) were added under N$_2$ atmosphere to the reaction mixture, which was sparged with N$_2$ for 10 min while immersed in oil bath preheated to 90 °C. The pressure vessel was sealed, and the temperature of the oil bath was raised to 180 °C after which the reaction mixture was stirred for 48 h. The reaction flask was removed from the oil bath, and the reaction mixture was allowed to cool to room temperature, then diluted with ethyl acetate and filtered through a pad of celite. Water was added to the filtrate and organic product was extracted with ethyl acetate. The combined organic layers were washed with brine and dried over MgSO$_4$. The organic extracts were filtered and concentrated by rotary evaporation. The resulting organic crude was purified by silica gel column chromatography using a gradient of 0-2% ethyl acetate in hexanes as the eluent, yielding the product as a white crystalline solid (0.62 g, 48%). ^{1}H NMR (400 MHz, DMSO-d_6) δ 7.58 – 7.51 (m, 4H), 3.57 (q, J = 7.1 Hz, 2H), 2.43 (s, 6H), 0.99 (t, J = 7.1 Hz, 3H). ^{13}C NMR (100 MHz, CDCl$_3$) δ 147.1, 134.9, 134.5, 127.0, 125.5, 122.8, 122.1, 50.1, 18.9, 14.8. ^{19}F NMR (400 MHz, CDCl$_3$) δ -65.4 (s, 6F). GCMS: m/z 391 (23%), 362 (100%), 330 (8%). Anal. Calcd. for C$_{18}$H$_{15}$F$_6$NS: C, 55.24; H, 3.86; N, 3.58. Found C, 55.04; H, 4.05; N, 3.60.

***N*-ethyl-3,7-dimethylphenothiazine antimonyhexachloride (3,7-DMeEPT-SbCl₆).** 3,7-DMeEPT (0.10 g, 0.39 mmol) was dissolved in anhydrous dichloromethane (5 mL) in an oven-dried 25 mL round-bottomed flask fitted with a rubber septum under nitrogen atmosphere after which the round-bottomed flask immersed in an ice water bath for 10 min. Then antimony pentachloride (0.080 mL, 0.58 mmol) was added into reaction mixture and stirred 15 min. Upon completion of the reaction, anhydrous diethyl ether (15 mL) was added gradually with continued stirring, resulting in a dark pink precipitate. The precipitate was filtered under nitrogen, then washed with more diethyl ether (20-30 mL) to remove unreacted starting material. The solid dark pink product (0.11 g, 50%) was dried under nitrogen and stored in a glove box. To grow crystals of this product, a saturated solution of 3,7-DMeEPT-SbCl₆ salt in anhydrous DCM was prepared. Then, a small volume of saturated solution (0.5 mL) transferred in an NMR tube and slowly layered it with anhydrous toluene (0.5 mL) to form two layers. Finally, the NMR tube was capped and vertically placed in a freezer set at 4 ºC, and crystals formed at the interface of the solvents.

***N*-ethyl-1,9-dimethylphenothiazine antimonyhexachloride (1,9-DMeEPT-SbCl₆).** 1,9-DMeEPT (0.10 g, 0.39 mmol) was dissolved in anhydrous dichloromethane (5 mL) in an oven-dried 25 mL round-bottomed flask fitted with a rubber septum under nitrogen atmosphere, then round-bottomed flask was cooled in an ice water bath for 10 minutes. Then antimony pentachloride (0.080 mL, 0.58 mmol) was added into reaction mixture and stirred 15 minutes. Upon completion of the reaction, anhydrous diethyl ether (15 mL) was added gradually with continued stirring, resulting in a blue precipitate. The precipitate was filtered under nitrogen, then washed with more diethyl ether (20-30 mL) to remove unreacted starting material. The solid blue product (0.10 g, 43%) was dried under nitrogen and stored in a glove box. To grow crystals of this product, a saturated solution of 1,9-DMeEPT-SbCl₆ salt in anhydrous DCM was prepared. Then, a small volume of saturated solution (0.5 mL) transferred in an NMR tube and slowly layered it with anhydrous diethyl ether (0.5 mL) to form two layers. Finally, the NMR tube was capped and vertically placed in a freezer set at 4 ºC, and crystals formed at the interface of the solvents.

***N*-ethyl-3,7-bis(trifluoromethyl)phenothiazine   antimonyhexachloride   (3,7-BCF₃EPT-SbCl₆).** 3,7-BCF₃EPT (0.10 g, 0.28 mmol) was dissolved in anhydrous

dichloromethane (5 mL) in an oven-dried 25 mL round-bottomed flask fitted with a rubber septum under nitrogen atmosphere, then round-bottomed flask was cooled in an ice water bath for 10 minutes. Antimony pentachloride (0.050 mL, 0.41 mmol) was added into reaction mixture and stirred 15 minutes. Upon completion of the reaction, anhydrous diethyl ether (15 mL) was added gradually with continued stirring, resulting in a dark green precipitate. The precipitate was filtered under nitrogen, then washed with more diethyl ether (20-30 mL) to remove unreacted starting material. The solid dark green product (0.12 g, 66%) was dried under nitrogen and stored in a glove box.

N-ethyl-1,9-dimethyl-3,7-bis(trifluoromethyl)phenothiazine antimonyhexachloride (1,9-DMe-3,7-BCF₃EPT-SbCl₆). 1,9-DMe-3,7-BCF₃EPT (0.18 g, 0.37 mmol) was dissolved in anhydrous dichloromethane (5 mL) in an oven-dried 25 mL round-bottomed flask fitted with a rubber septum under nitrogen atmosphere, then round-bottomed flask was cooled in an ice water bath for 10 minutes. Antimony pentachloride (0.080 mL, 0.55 mmol) was added into reaction mixture and stirred 15 minutes. Upon completion of the reaction, anhydrous diethyl ether (15 mL) was added gradually with continued stirring, resulting in a blue precipitate. The precipitate was filtered under nitrogen, then washed with more diethyl ether (20-30 mL) to remove unreacted starting material. The solid purple product (0.14 g, 42%) was dried under nitrogen and stored in a glove box. To grow crystals of this product, a saturated solution of 1,9-DMe-3,7-BCF₃EPT-SbCl₆ salt in anhydrous DCM was prepared. Then, a small volume of saturated solution (0.5 mL) transferred in an NMR tube and slowly layered it with anhydrous diethyl ether (0.5 mL) to form two layers. Finally, the NMR tube was capped and vertically placed in a freezer set at 4 ºC, and crystals formed at the interface of the solvents.

4.5.3 X-ray Crystallography

X-ray diffraction data were collected at 180(1) K on a Bruker D8 Venture kappa-axis diffractometer using MoK(alpha) X-rays. Raw data were integrated, scaled, merged and corrected for Lorentz-polarization effects using the APEX3 package.[37] Corrections for absorption were applied using SADABS.[38] The structure was solved by direct methods

(SHELXT)[39] and refinement was carried out against F^2 by weighted full-matrix least-squares (SHELXL).[40] Hydrogen atoms were found in difference maps, but subsequently placed at calculated positions and refined using a riding model. Non-hydrogen atoms were refined with anisotropic displacement parameters. Atomic scattering factors were taken from the International Tables for Crystallography.[41]

4.5.4 Cyclic Voltammetry

Cyclic voltammetry (CV) experiments were performed with a CH Instruments 600D potentiostat using a three-electrode system with glassy carbon as the working electrode, freshly anodized Ag/AgCl as the reference electrode, and a Pt wire as the counter electrode at 1 mM analyte in 0.1 M nBu_4NPF_6 in DCM. Voltammograms were recorded at a scan rate of 100 mV s^{-1}. Ferrocene or decamethylferrocene was used as an internal reference and oxidation potentials were calibrated relative to ferrocenium/ferrocene ($Cp_2Fe^{+/0}$). The diffusion coefficients of the active species at 1 mM concentration were calculated using Randles–Sevcik equation,[42]

$$i_p = 0.4463 \, nFAc \left(\frac{nFD}{RT} v \right)^{0.5}$$

where i_p is the peak current (A), n is the number of electrons transferred (-), F is the Faraday constant (96485 C mol^{-1}), A is the electrode area (cm^2), c is the concentration (mol cm^{-3}), D is the diffusion coefficient (cm^2 s^{-1}), R is the gas constant (8.314 J mol^{-1} K^{-1}), T is the absolute temperature (K), and v is the scan rate (V s^{-1}). The following scan rates were used for diffusion coefficient calculations: 25, 50, 75, 100, 200, 300, 400, and 500 mV s^{-1}.

4.5.5 Computational Studies

All density functional theory (DFT) calculations were performed using the Gaussian09 (Revision A.02b) software suite. Geometry optimizations of the neutral and radical-cation states were carried out using the B3LYP functional at the 6-311G(d,p) level of theory.[43] Frequency analyses of all (fully relaxed) optimized geometries were performed to ensure that the geometries were energetic minima.

4.5.6   UV-vis Spectroscopy

UV-vis spectra were obtained using optical glass cuvettes (Starna) with 2 or 10 mm path length on an Agilent 8453 diode array spectrophotometer. All the radical cation solutions were prepared in anhydrous DCM and transferred into cuvettes inside an argon filled glovebox. The capped cuvettes were taken out from the glove box for spectral analysis.

UV-vis study at 0.2 mM concentration: All phenothiazine radical cation salts (EPT-SbCl$_6$, 3,7-DMeEPT-SbCl$_6$, 1,9-DMeEPT-SbCl$_6$, 3,7-BCF$_3$EPT-SbCl$_6$, and 1,9-DMe-3,7-BCF$_3$EPT-SbCl$_6$) were dissolved in anhydrous DCM at 0.2 M and pipetted to 1 cm path length cuvettes. UV-vis spectra were collected at 5, 15, 30, 60, 120, 180, 240, 300 min after preparing samples.

UV-vis study at different concentrations: 1,9-DMe-3,7-BCF$_3$EPT-SbCl$_6$ was dissolved in anhydrous DCM at 1, 5, and 10 mM and pipetted to 2 mm path length cuvettes. UV-vis spectra were collected at 5, 15, 30, 60, 120, 180, 240, 300 min after preparing samples.

UV-vis study for shelf stability: Freshly synthesized radical cation salts of EPT-SbCl$_6$ and 1,9-DMe-3,7-BCF$_3$EPT-SbCl$_6$ were stored in two different environments; 1. stored in a glass vial and placed inside an argon filled glove box, 2. stored in a glass vial and placed on the bench top. The radical cation salts were weighed either inside of the glove box or outside of the glove box to prepare samples for UV-vis analysis, depending on where it has been stored. Then, all solutions were prepared in anhydrous DCM and transferred into cuvettes inside an argon filled glovebox. EPT-SbCl$_6$ was analyzed at 0.2 mM (in 10 mm pathlength cuvette) as its solubility is less than 1 mM in DCM and 1,9-DMe-3,7-BCF$_3$EPT-SbCl$_6$ was analyzed at 1 mM (in 2 mm pathlength cuvette) as it highly decays at 0.2 mM. At days 0, 7, 14 and 21, required amounts (to make a 0.2 or 1 mM solution) of each radical cation salt stored on bench-top (weighed outside the glovebox) and the ones stored inside the box (weighed inside the glovebox) were dissolved in anhydrous DCM (inside the glovebox) and prepared UV-vis samples for analysis.

CHAPTER 5. A COMPARATIVE STUDY OF ORGANIC RADICAL CATION STABILITY AND COULOMBIC EFFICIENCY FOR NONAQUEOUS REDOX FLOW BATTERIES

This chapter is reproduced from "A Comparative Study of Organic Radical Cation Stability and Coulombic Efficiency for Nonaqueous Redox Flow Battery Applications" by **N. Harsha Attanayake**, T.M. Suduwella, Aman Preet Kaur, Yichao Yan, Zhiming Liang, Sean R. Parkin, Melanie S. Sanford, and Susan A. Odom, which is in preparation.

5.1 Summary

When building energy dense RFBs, the solubility of redox couples and cell voltage of the flow cell are critical. However, the stability of the charged forms of redox active species suffers at their extreme redox potentials due to either self-discharge in electrolyte solutions or molecular degradation, presenting a challenge in achieving high cell voltages. In this work, we sought to explore the change of chemical stability and cycling stability of organic posolytes by considering variably functionalized electron donating redox active organic molecules at different oxidation potentials in a nonaqueous electrolyte systems. Further, variation of coulombic efficiency of posolytes with the chemical stability of their charged forms was compared, by performing bulk electrolysis and UV-vis experiments. The organic posolytes derived from high oxidation potentials exhibited either self-discharge or molecular degradation at their charged form, minimizing either coulombic efficiency or cycle lifetime in the galvanostatic cycling compared to the lower oxidation potential posolystes.

5.2 Introduction

A large variety of electron-donating and electron-accepting organic molecular cores are reported in literature to be used as posolytes and negolytes, respectively, for RFB applications.[1-5] However, they are still in their infancy and none of them have shown a sufficient stability to compete with the well-developed vanadium technology that offers at least 20 years of lifetime.[6] During the charging process of RFBs, neutral posolyte molecules oxidize and generate radical cations. In general, radical cations are more reactive

than their neutral forms, and thus they undergo in a variety of parasitic reactions (e.g. dimerization, nucleophilic reactions, disproportionation, and self-discharge) which affect the lifetime and coulombic efficiency (CE) of the battery.[3, 7-13] Therefore, developing organic posolytes with much stable charged form is indeed necessary to have efficient and long-running organic RFBs.

Among the reported posolytes, phenothiazine,[2, 8, 14] dialkoxybenzene,[15-16] ferrocene,[17-18] cyclopropenium,[12, 19] nitroxyl radicals,[20-21] and phenazine[22-23] have shown promising performance in screening experiments for nonaqueous RFBs. All these materials have shown chemically and electrochemically reversible reactions at least under cyclic voltammetry (CV) conditions in a given electrolyte, yet their long-term stability in galvanostatic cycling is different. As Kowalski *et al*. reported recently, it is quite difficult to compare the long-term stability and efficiency of active species in charge/discharge experiments due to variabilities in experimental conditions such as active species concentration, type of supporting salt and solvent, charge-discharge rate, and state of charge (SOC) variations.[24] Thus, an easy and a robust standardize technique is required to have a meaningful comparison.

The cycling stability and efficiency of a posolyte could be able to predict by measuring the chemical stability of its least stable charged state.[9, 25-26] The charged forms can be generated by a variety of techniques including chemical oxidation, electrochemical oxidation via bulk electrolysis, and irradiation with gamma rays.[7, 9, 25, 27] The purity of the radical cation salts is critical when they generate for a chemical stability determination. In the chemical oxidation method, by optimizing the reaction conditions it is possible to prevent unnecessary reactions and convert all the neutral components to their charged form in the reaction mixture, then isolate radical cation salts with a high purity – as a solid in most of the cases. Further, X-ray quality crystals of radical cations can be grown for structural identification. By contrast, radical cation generation with electrochemical techniques like bulk electrolysis (BE) may relatively easy and fast, however, purity could compromise due to the working electrode solution contamination with the trace side products crossing from the counter electrode. Further, electrochemical reactions are required to have conducting salts in the solution as nonaqueous solvents have very low conductivities. Thus, studying stability of charged species in the absence of supporting salts

is quite impossible unless otherwise active materials are conductive. Considering the afore mentioned methods for generating radical cations, we are interested in generating charged species using chemical oxidants, then isolate the radical cations as solids with a high purity and study the chemical stability in solution phase via UV-vis spectroscopy to predict the cycling stability and efficiency of organic posolytes.
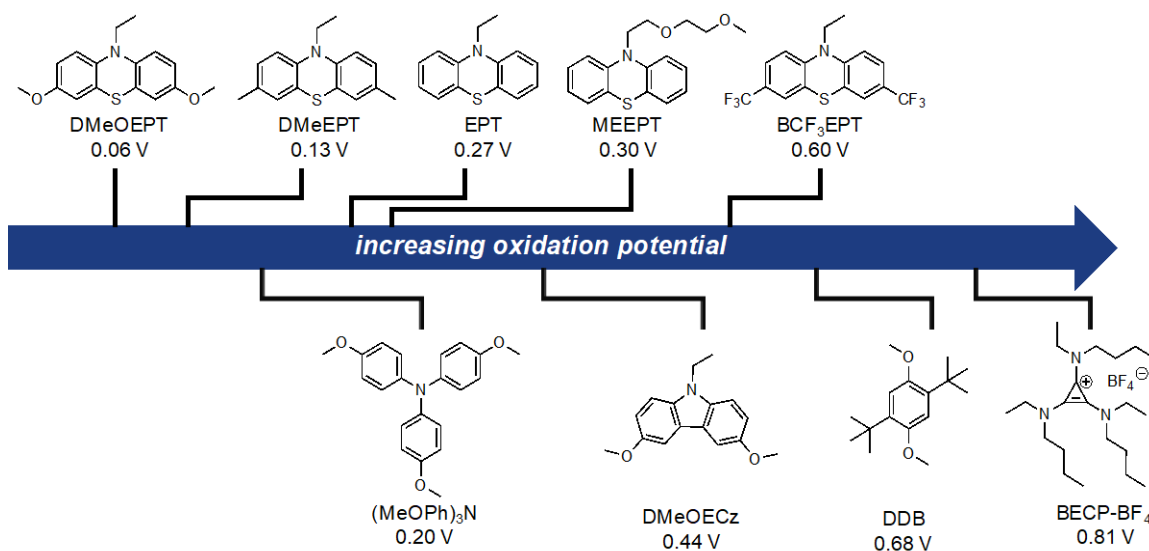
Figure 5.1. Representations of chemical structures as increasing their redox potential vs. $Cp_2Fe^{0/+}$; *N*-ethyl-3,7-dimethoxyphenothiazine (DMeOEPT), *N*-ethyl-3,7-dimethylphenothiazine (DMeEPT), 4,4,4-trimethoxytriphenylamine ((MeOPh)$_3$N), *N*-ethylphenothiazine (EPT), N-(2-(2-methoxyethoxy)-ethyl)phenothiazine (MEEPT), *N*-ethyl-3,6-dimethoxycarbazole (DMeOECz), *N*-ethyl-3,7-bis(trifluoromethyl)phenothiazine (BCF$_3$EPT), 1,4-ditertbutyl-2,5-dimethoxybenzene (DDB), and (*N*-butylethylamino)cyclopropenium tetrafluoroborate (BECP-BF$_4$). (MeOPh)$_3$N and DMeOECz was synthesized by Thilini Malsha Suduwella, BCF$_3$EPT was synthesized by Dr. Aman Preet Kaur, and BECP-BF$_4$ was synthesized by Yichao Yan.

Coulombic efficiency of RFBs is as important as the lifetime of a battery, but a limited number of studies have been focused on evaluating the facts behind efficiency losses. The CE fades could occur due to a variety of reasons including active species crossover through membrane/separator, parasitic reactions of active species, disproportionation, and self-discharge of charge species into their uncharged forms.[8, 11, 16, 28-30] To this end, we explore the change of chemical and cycling stabilities of organic posolytes with their oxidation potentials. We selected, variably functionalized electron donating redox active organic molecules including phenothiazine, triphenylamine,

carbazole, dialkoxybenzene, and cyclopropenium – all of which have different oxidation potentials for this study. The chemical stability of charged species was analyzed using UV-vis spectroscopy on isolated radical cation salts of organic posolytes in a common electrolyte solution. The CE variation with oxidation potential of posolytes was tested using BE cycling at variable concentrations of selected active species and at variable charge-discharge rates. Here, we report synthesis of charged and uncharged forms of differently functionalized posolytes, impact of trace impurities on the stability of charged forms, and a correlation between self-discharge and CE.

5.3   Results and Discussion

5.3.1   Synthesis

Uncharged form of all the posolytes (Figure 5.1) were either purchased or synthesized as previously reported (Detailed information is provided in the Experimental section). Radical cation salts/charged form of all nine posolytes were synthesized by chemical oxidation using $NOBF_4$ (nitrosonium tetrafluoroborate) as the chemical oxidant and oxidized products were isolated as solids. All the isolated radical cations have (BF_4^-) as the anion. Synthetic procedures and spectroscopic analysis are provided in the Experimental section.
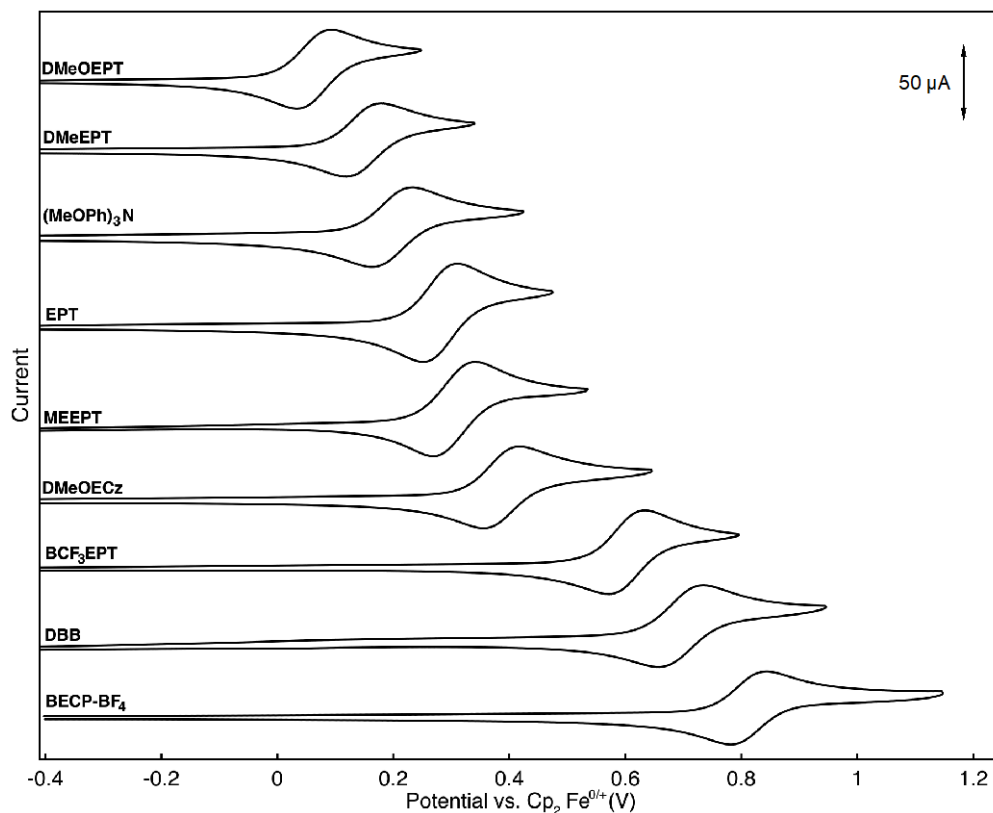
Figure 5.2. Cyclic voltammograms of the first oxidation of DMeOEPT, DMeEPT, (MeOPh)$_3$N, EPT, MEEPT, DMeOECz, BCF$_3$EPT, DDB, and BECP-BF$_4$ at 1 mM in 0.1 M TEABF$_4$ in acetonitrile, recorded at a scan rate of 100 mV/s. Voltammograms were calibrated to Cp$_2$Fe$^{0/+}$ at 0 V, using ferrocene as an internal reference. 100% iR correction was applied.

5.3.2 Cyclic Voltammetry

Cyclic Voltammetry (CV) was performed to determine electrochemical properties including redox potentials and the chemical and electrochemical reversibility of the posolytes. Voltammograms were recorded in 0.1 M TEABF$_4$/ACN electrolyte, and 100% iR correction was applied to compensate for solution resistance. Because we aimed to evaluate the stability of radical cation form (radical dication in case of BECP-BF$_4$) of the given posolytes, only the first oxidation event of the active species is chemically and electrochemically characterized. Figure 5.1 orders the posolytes according to their first oxidation potential, with calibrated scans of the first oxidation being show in Figure 5.2. This and other quantitative electrochemical data are summarized in Table 5.1. In this series,

111

oxidation potentials vary from the lowest at 0.06 V to the highest 0.81 V, referenced to $Cp_2Fe^{0/+}$ at 0 V.

Except for one case, with $(MeOPh)_3N$ which has a value of 1.25, the ratio of anodic and cathodic peak-current of all the molecules lie around 1 (range:1.01 to 1.11), showing that first redox event of all but one of the posolytes is chemically reversible. Analysis of peak-to-peak separations shows that the first oxidation events are also electrochemically reversible. This is true for the 100 mV/s scan rates shown in Figure 5.2 as well as the variable scan rates shown in Figure 5.3. Except for $(MeOPh)_3N$, all compounds show a linear relationship of peak-to-peak separations versus scan rate, as shown in the Randle-Sevcik analysis[38] plot in Figure 5.4

Cyclic Voltammetry (CV) was performed to determine fundamental electrochemical properties including redox potential, chemical and electrochemical reversibility of all posolytes. This experiment was done in 0.1 M $TEABF_4$/ACN electrolyte and 100% iR correction was applied to compensate the solution resistance. All the posolytes utilized in this study are arranged according to their first oxidation potential as shown in Figure 5.1. Further, voltammogram of the first oxidation event of posolytes are provided in Figure 5.2. Because we aimed to evaluate the stability of radical cation form of the given posolytes, only the first oxidation event of active species is chemically and electrochemically characterized. The ratio of anodic and cathodic peak-current of all the molecules lie around one, except $(MeOPh)_3N$ (Table 5.1) in 0.1 M $TEABF_4$/ACN. Thus, the first redox event of all the posolytes are chemically reversible, except for $(MeOPh)_3N$, which shows a partial reversibility. Further, kinetic analysis (peak-to-peak separation) shows that the first oxidation events are electrochemically reversible in the same electrolyte.

Table 5.1. Measured half-wave potentials ($E_{1/2}^{0/+}$) vs. $Cp_2Fe^{0/+}$, peak current ratios, and peak separations for the first oxidation, and diffusion coefficient of DMeOEPT, DMeEPT, (MeOPh)$_3$N, EPT, MEEPT, DMeOECz, BCF3EPT, DDB, and BECP-BF$_4$.

Compound	$E_{1/2}^{0/+}$ vs. $Cp_2Fe^{0/+}$ (V)	Peak-current ratio	Peak separation (mV)	Diffusion coefficient (x 10^{-6} cm^2 s^{-1})
DMeOEPT	0.06	1.05	59	14.6
DMeEPT	0.13	1.05	64	15.4
(MeOPh)$_3$N	0.20	1.25	70	4.17
EPT	0.27	1.01	59	16.3
MEEPT	0.30	1.03	58	12.3
DMeOECz	0.44	1.11	62	15.8
BCF3EPT	0.60	1.10	62	13.1
DDB	0.68	1.07	66	13.4
BECP-BF$_4$	0.81	1.09	59	11.2

In this series of molecules, oxidation potentials vary from 0.06 V to 0.81 V vs. $Cp_2Fe^{0/+}$. The oxidation potential of ethyl-substituted phenothiazines was altered by introducing either electron-donating groups (Figure 5.1: DMeOEPT 0.06 $Cp_2Fe^{0/+}$, DMeEPT 0.13 $Cp_2Fe^{0/+}$) or electron-withdrawing groups (Figure 5.1: BCF$_3$EPT 0.60 $Cp_2Fe^{0/+}$).[31] In the presence of electron-donating groups, generally, increasing the energy of HOMO (Highest Occupied Molecular Orbital) lowers the oxidation potential while electron-withdrawing groups increase the oxidation potential by lowering the energy of HOMO.[32-33] However, electron-donating dimethoxy substituted carbazole derivative (Figure 5.1: DMeOECz 0.44 V vs. $Cp_2Fe^{0/+}$) showed a higher oxidation potential than the similarly functionalized phenothiazine derivative (DMeOEPT, 0.06 V $Cp_2Fe^{0/+}$) due to the absence of the electron-rich sulfur atom in carbazole. Generally, a conjugated framework with a polarizable heteroatoms lowers the ionization potential of a molecule compared to its hydrocarbon counterparts.[34] DDB and BECP-BF$_4$ (0.68, 0.81 V vs. $Cp_2Fe^{0/+}$, respectively) exhibited the highest oxidation potentials in this series due to their diluted π-conjugation due to compared to the other molecular cores (Figure 5.1).
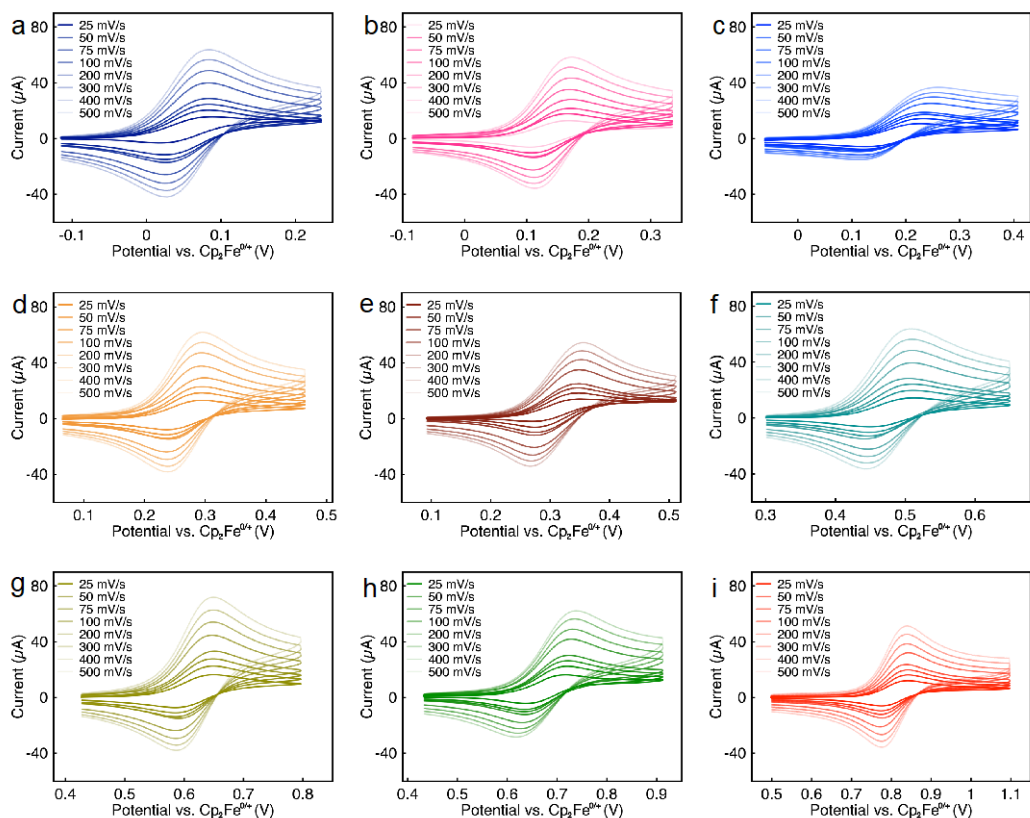
Figure 5.3. The scan rate-dependent cyclic voltammograms of active species at 1 mM in 0.1 M TEBF$_4$/ACN. DMeOEPT (a), DMeEPT (b), (MeOPh)$_3$N (c), EPT (d), MEEPT (e), DMeOECz (f), BCF$_3$EPT (g), DDB (h), and BECP-BF$_4$ (i) at scan rates of 25, 50, 75, 100, 200, 300, 400, and 500 mV s^{-1}. All cyclic voltammograms were referenced to ferrocene/ferrocenium at 0 V. 100% iR correction was applied.
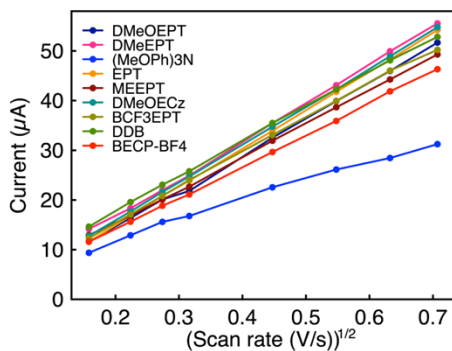
Figure 5.4. Randles–Sevcik plots for all the compounds, data acquired from Figure 5.3.

5.3.3 UV-vis Spectroscopy

Given that the first oxidation event of all posolytes was chemically and electrochemically reversible on the CV time scale even at slower scan rates (25 mV s^{-1}), as

114

shown in Figure 5.3. We further wanted to study the stability of charged form of all the posolytes in the same electrolyte as reversibility on the CV time scale does not always corelate with their long-term stability. Analysis of species intensity by UV-vis is a simple that has been utilizing in a variety of fields including energy storage to study the radical cations. Depending on the molar absorptivity of a species, a variety of concentrated radical cation solutions can be analyzed through UV-vis spectroscopy. Our previous studies showed that trace impurities present in ACN play a big role in the stability of radical cations in the solution phase.[7] Thus, it is important to find out a concentration limit to analyze the long-term stability of radical cation salts in 0.1 M TEABF$_4$/ACN electrolyte system which has the minimum impact from the electrolyte trace impurities on the stability. With this regard, we tested the stability of MEEPT-BF$_4$ at a concentration ranging from 0.1 to 10 mM in 0.1 M TEABF$_4$/ACN. We analyzed radical cation solutions with concentrations of 0.1 and 0.5 mM using a 10 mm pathlength cuvette while 1, 5, and 10 mM used a 1 mm pathlength cuvette to prevent the UV-vis detector saturation in the longer wavelength region of the absorption spectrum (600-950 nm). Figures 5.5a-e show the UV-vis absorption spectra of MEEPT-BF$_4$ in 0.1 M TEABF$_4$/ACN over period of 3 h. A comparison of absorbance changes over time at different concentrations are shown in the Figure 5.5f. The absorption of each concentrated sample at 5 min was normalized to a value of 1 at 770 nm. As we expected, stability of MEEPT-BF$_4$ varies with the concentration; at 0.1 mM, only 76% of the initial absorption intensity remained after 3 h, also 0.5, 1, 5, and 10 mM solutions showed 96%, 97%, 98%, 99% absorption intensity retention at 3 h, respectively (Figure 5.5f). This result suggests that the trace impurities presence in the electrolyte system, indeed triggers the radical cation decay at low concentrations. Thus, we selected to study the stability of charged forms of all the posolytes at 10 mM to prevent the effect of trace impurities on their stability.
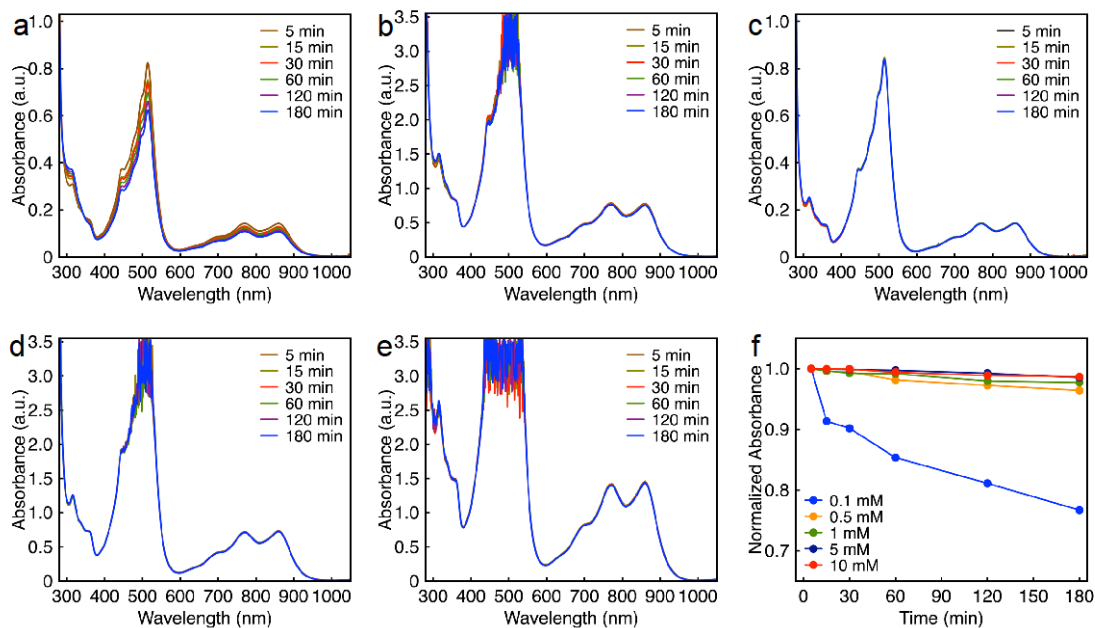
Figure 5.5. UV-vis absorption spectra of MEEPT-BF$_4$ at 0.1 (a), 0.5 (b), 1 (c) 5 (d), and 10 mM (e) over time in 0.1 M TEABF$_4$/ACN, recorded at 5, 15, 30, 60, 120, and 180 min after dissolution. Normalized absorbance of UV-vis absorbance at 770 nm vs time at various concentrations of MEEPT-BF$_4$ in 0.1 M TEABF$_4$/ACN (f). 0.1 and 0.5 mM samples were recorded using 10 mm path length cuvettes while 1, 5, and 10 mM samples were recorded using 1 mm pathlength cuvettes.

To study the long-term stability of the charged form of all the posolytes, these species were synthesized and isolated as solids via chemical oxidation. Nitrosonium tetrafluoroborate (NOBF$_4$) was chosen as the chemical oxidant because it has a higher oxidation potential than all the selected posolytes in this study and it generates NO gas as a biproduct, a gas that is removed from the reaction mixture during the radical cation salts preparation. The oxidized form of all the posolytes had tetrafluoroborate (BF$_4^-$) as the anion. The long-term chemical stability of radical cation salts in 0.1 M TEABF$_4$/ACN electrolyte solution was studied using UV-vis spectroscopy in 1 mm pathlength cuvettes. The changes of UV-vis absorption spectrum (intensity loss or new peak formation) was monitored over period of 24 h. Formation of new peaks in the absorption spectrum with time could result from the formation or cleavage of covalent bonds in the active species. The loss of intensity could arise either due to reduction of charged species to its neutral form through an electron transfer (self-discharge) mechanism or active species decomposition through covalent bond formation or cleavage. In this case, decomposed

116

products should have either an equal absorption profile to the initial charged species, or they should UV-vis inactive, hence remaining radical cations show up on the absorption spectrum with a reduced intensity.
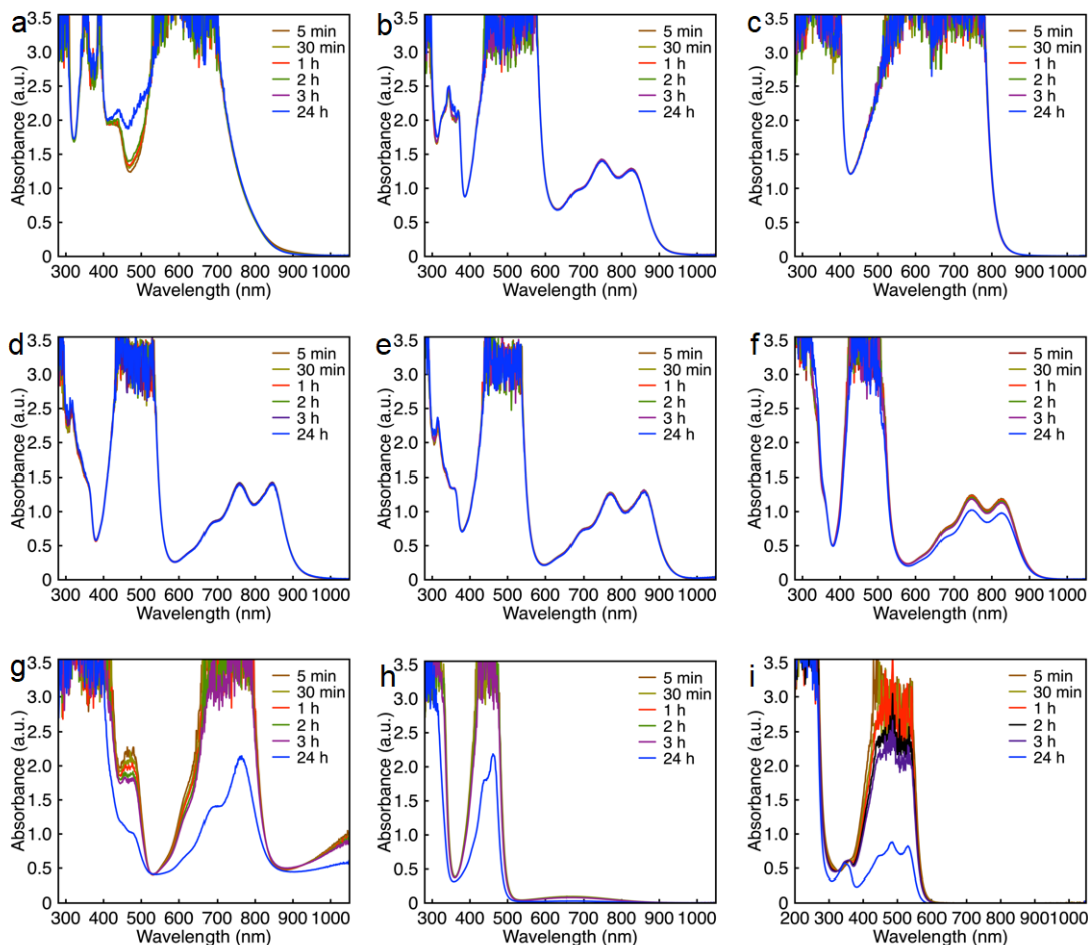
Figure 5.6. UV-vis absorption spectra of 10 mM radical cation slats of DMeOEPT (a), DMeEPT (b), (MeOPh)$_3$N (c), EPT (d), MEEPT (e), DMeOECz (f), BCF$_3$EPT (g), DDB (h), and BECP-BF$_4$ (i) in 0.1 M TEABF$_4$/ACN, recorded at 5 min, 0.5, 1, 2, 3, and 24 h after dissolution. The radical cation salts have tetrafluoroborate (BF$_4$) ion as the anion.

Figure 5.6 shows the UV-vis absorption spectra for radical cation salts of all the posolytes in 0.1 M TEABF$_4$/ACN over time. Even though most of the phenothiazine radical cation salts showed absorbance peaks at around 1.4 absorbance units in the long wavelength region, the UV-vis detector was saturated for the other radical cation salts at 10 mM in electrolyte solution (Figure 5.6: DMeOEPT (a), (MeOPh)$_3$N (c), DMeOECz (f), DDB (h), and BECP-BF$_4$ (i)). Thus, we are unable to provide a quantitative, decay analysis for the decayed radical cation salts based on peak intensities, although we can use non-

peak intensities – less reliable but still useful. The UV-vis absorption profiles of the radical cation salts prepared from low to moderate oxidation potential posolytes (Figure 5.6: DMeOEPT (a), DMeEPT (b), (MeOPh)$_3$N (c), EPT (d), and MEEPT (e)) were more persistent over the time while noticeable decay in absorption intensity was observed for the radical cations derived from the high oxidation potential posolytes (Figure 4: DMeOECz (f), BCF$_3$EPT (g), DDB (h), and BECP-BF$_4$ (i)).

The oxidized species of the highest oxidation potential posolyte, BECP-BF$_4$ showed the highest decay in absorption intensity over period of 24 h (Figure 5.6i). It is unclear that the absorption intensity loss is either due to self-discharge or active species decomposition as shape of the spectrum at 24 h cannot reliably be compared to the spectrum at 5 min due to the detector being saturated at the beginning of the experiment. If the decay process is due to self-discharge, the diluted decayed radical cation solution of BECP-BF$_4$ should show a similar absorption spectrum to its unoxidized form since the charged form lost the most of its intensity after 24 h. Thus, the decayed sample was diluted 10x in the glove box to obtain a 1 mM solution, which was inserted via syringe into 1 mm path length cuvette to record another UV-vis spectrum. For comparison, a 1 mM unoxidized BECP-BF$_4$ solution was prepared in the same electrolyte, and UV-vis spectrum was recorded in 1 mm path length cuvette. Figure 5.7 shows UV-vis spectra of oxidized form of BECP-BF$_4$ at 5 min and 24 h (brown and blue lines respectively), diluted solution of decayed radical cation (green line), and unoxidized form (shaded ash) of BECP-BF$_4$ in 0.1 M TEABF$_4$/ACN electrolyte solution. The diluted radical cation spectrum and the spectrum of unoxidized form of BECP-BF$_4$ are mostly overlap with each other. Thus, it can be concluded that the oxidized form of BECP-BF$_4$ has been converted to its unoxidized form through a self-discharge process rather than undergoing in a molecular decomposition through covalent bond formation or cleavage over the period of 24 h. The source of electrons for this reduction process is unclear. We speculate that trace water or other possible trace impurities present in electrolyte system such as metal ions, amine, amides, or acids could act as a reducing agent; or a reduction process could occur as a consequence of hydrogen transfer reaction with solvent/electrolyte as suggested by Zhang *et. al.* considering dimethoxybenzene derivatives. However, further studies are required to identify the source of electrons for the self-discharge process.[11]
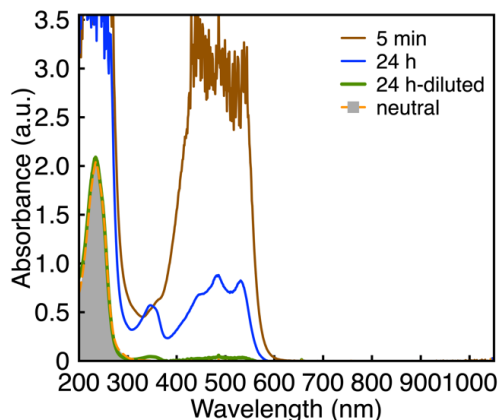
Figure 5.7. UV-vis spectrum of diluted BECP-BF$_4$ radical cation salt after 24 h and its neutral form at 1 mM in 0.1 M TEABF4/ACN.

5.3.4 Bulk electrolysis

In addition to active species crossover through membranes/separators in flow batteries, self-discharge of charged species could be another reason to the observed inefficiencies in charge-discharge capacities of flow batteries. Thus, we performed a systematic galvanostatic cycling study utilizing bulk electrolysis (BE) technique to determine the effect of charged species self-discharge on the coulombic efficiency during cell cycling. All BE experiments were done in a custom-made H cell, which has an ultra-fine porous glass frit (P5, Adams and Chittenden) to prevent the electrolyte mixing.
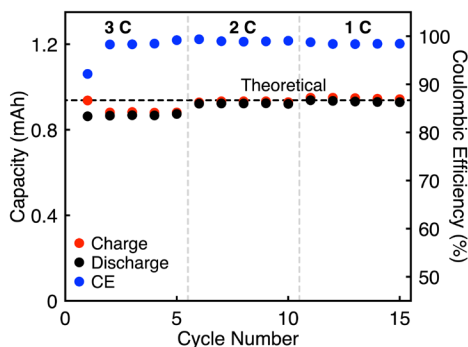
Figure 5.8. Bulk electrolysis cycling (capacity and CE vs. cycle number) of MEEPT at various charging rates including, 3, 2, and 1C. Both sides of the H cell contain 10 mM active species in 0.1 M TEABF4/ACN.

If trace impurities present in the electrolyte trigger the self-discharge of charged species, a relatively large portion of radical cation should convert its neutral form at a low

119

concentration of active species, and at an elevated concentration, the amount of conversion should be lower. Thus, at a high concentration of active species, we expect to see a higher CE compared to the CE at a lower active species concentration under the same conditions. Further, the CE could should lower as the as the rate of charge-discharge decreases. If BE cells are charged at faster rates, there will be less time for the self-discharge process compared to a slower charging. Thus, higher CE should result at a faster charging rate. By contrast, the CE should not change with the charging rate (C-rate) if charged form of the active species chemically stable without undergoing a process of self-discharge. With that in mind, first we tested moderate oxidation potential, MEEPT at 10 mM in 0.1 M TEABF$_4$/ACN (Figure 5.8). We selected MEEPT to validate this technique as the charged form of MEEPT (MEEPT-BF$_4$) showed a greater stability over time in the previous UV-vis experiment (Figure 5.6e). The BE cycling was done at three different C-rates (3, 2, and 1C) with five charge/discharge cycles at each C-rate. MEEPT showed high CE during BE cycling, and it's about 98-99%. Importantly CE did not change with the C-rate as we hypothesized. 1-2% of CE lost, might be a result of the active species cross over through the non-selective glass frit of H cell. Further, post-test CV analysis showed that MEEPT does not undergo redox center decomposition at each C-rate (Figure 5.11a).
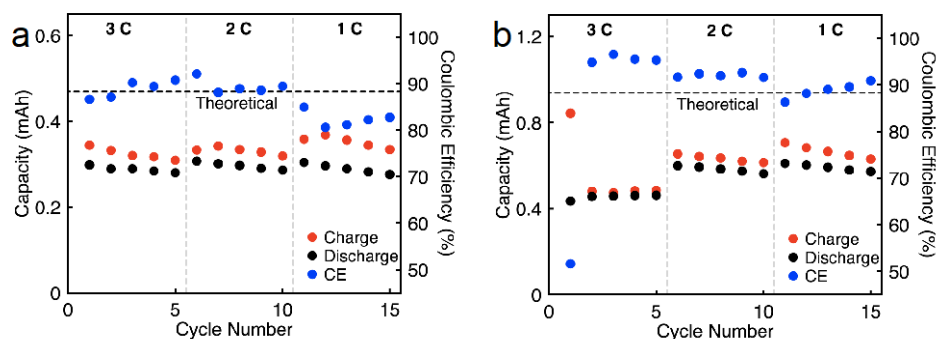
Figure 5.9. Bulk electrolysis cycling (capacity and CE vs. cycle number) of BECP-BF$_4$ in 0.1 M TEABF$_4$/ACN at 5 mM (a), and 10 mM (b). Both sides of the H cell contain active species with same concentration in 0.1 M TEABF$_4$/ACN and the experiment was conducted at various charging rates including, 3, 2, and 1C.

Next, we analyzed the highest oxidation potential BECP-BF$_4$ in BE, since we evidenced that charged form of BECP-BF$_4$ underwent in a self-discharge process from UV-vis experiment. This experiment was performed at two different concentrations (5 and 10 mM) in 0.1 M TEABF$_4$/ACN. The BE cycling was done at three different C-rates (3C, 2C,

and 1C) with five charge/discharge cycles at each C-rate, the same as was done for MEEPT analysis. Figure 5.9 shows CE and capacity vs. cycle number of BECP-BF$_4$ at 5 (a) and 10 (b) mM in 0.1 M TEABF$_4$/ACN. As we hypothesized, faster rates of charging in BE resulted a higher CE, perhaps due to a limited time for self-discharge. The CE was found to increase in the order of CE at 1C < CE at 2C < CE at 3C, and the trend remains the same regardless the active species concentration (Figure 5.9). The comparison of CE between 5 and 10 mM shows that BE cycling at 10 mM has higher CE than CE at 5 mM active species, in the same C-rate. This is perhaps due to the higher ratio of trace impurities in the electrolyte at 5 mM active species, compared to 10 mM, lead to the higher degree of self-discharge, thus, lower CE, as stated above. Further, post-test CV analysis (Figure 5.11b) of 10 mM BECP-BF$_4$ showed that most of the active material remained intact without showing a noticeable redox center decomposition at each C-rate. Thus, the observed relatively lower CE (90-95%) could not be a result of active species degradation.
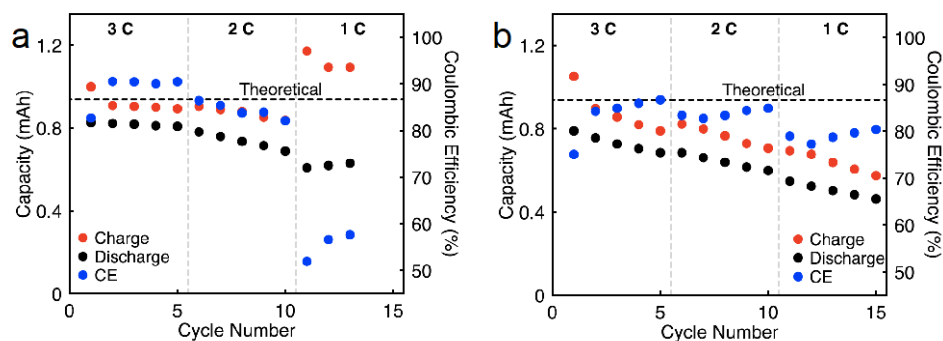
Figure 5.10. Bulk electrolysis cycling (capacity and CE vs. cycle number) of DMeOECz (a), and DDB (b) in at various charging rates including, 3, 2, and 1C. Both sides of the H cell contain 10 mM active species in 0.1 M TEABF$_4$/ACN.

Note that we aware that some CE could fade will result due to the active species crossover through non-selective P5 glass frit in the BE setup. We assumed that fraction of crossover at each C-rate could be equal. Thus, equal amount of CE could be faded at each C-rate similarly observed in BE analysis of MEEPT. Therefore, the effect of crossover can be eliminated from the CE comparison.
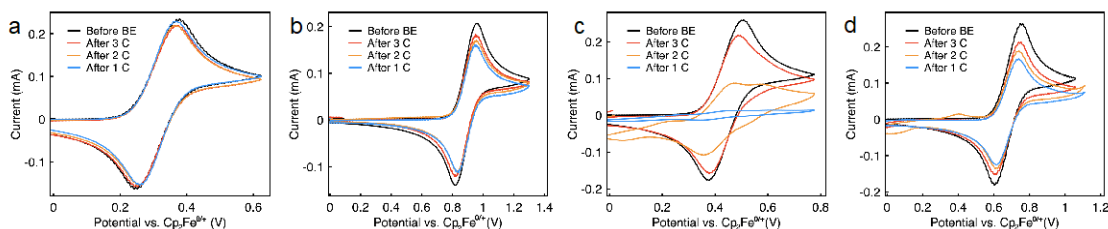
Figure 5.11. Post-BE cyclic voltammetry scans (100 mV s^{-1}) recorded on working electrode side of selected posolytes, before and after bulk electrolysis conducted at 10 mM in 0.1 M TEABF$_4$/ACN. The first oxidation events of MEEPT (a), BECP-BF$_4$ (b), DMeOECz (c), and DDB (d).

We analyzed more high potential compounds in BE to further study the relationship between self-discharge and CE. Here we selected DMeOECz and DDB as their radical cation salts exhibited a noticeable decay in the UV-vis experiment. Both compounds were analyzed at 10 mM in 0.1 M TEABF$_4$/ACN. Figure 5.10 shows the CE and capacity change vs. cycle number for DMeOECz (a) and DDB (b). DMeOECz showed a noticeable drop in CE with variable rates. As evidenced by post-cycling CV analysis, significantly decomposed during the BE experiment (Figure 5.11c). At 1 C, the redox center of DMeOECz was completely decomposed, thus we were unable to complete five charge-discharge cycles at this C rate. Therefore, the low CE in the BE and intensity decay in UV-vis experiment are most likely due to a molecular decomposition. DDB showed C-rate dependent CE variation (CE at 1C < CE at 2C < CE at 3C) similar to BECP-BF$_4$ (Figure 5.10b). But, unlike in BECP-BF$_4$, discharge capacity was decreased with the decreasing of C-rate, indicating some possible active species degradation. Further supporting, post-CV analysis showed that a certain amount of active species was decomposed during BE cycling. Thus, observed CE variation, perhaps result of a combination of radical cation self-discharge and molecular decomposition.

5.4   Conclusions

Here we synthesized and isolated the charged forms of nine different posolytes to determine their chemical stability in solution phase. The concentration dependent MEEPT-BF$_4$ stability study showed that the trace impurities presence in the electrolyte system, trigger the radical cation decay at low concentrations. The UV-vis experiments showed that the charged species derived from the low oxidation potential posolytes have higher

chemical stability over time compared to the charged species derived from the higher oxidation potential posolytes, perhaps due to the high voltage charged species underfoing faster electron transfer process with the trace electrolyte impurities, minimizing their persistency in the solution phase. High oxidation potentials posolytes exhibited either self-discharge or molecular degradation in their charged forms, minimizing either coulombic efficiency or cycle lifetime in the galvanostatic cycling, arising a challenge of utilizing high potential compounds in nonaqueous RFBs.

5.5   Experimental

5.5.1   Synthesis

Materials

Nitrosonium tetrafluoroborate (98%) was purchased from Alfa Aesar and was stored and weighed in an argon-filled glovebox (MBraun, O2 < 0.5 ppm, H2O < 0.5 ppm). N-((2-methoxy)ethoxy)ethylphenothiazine (MEEPT, > 98%) was purchased from TCI. 1,4-ditertbutyl-2,5-dimethoxybenzene (DDB, 99%) was purchased from 3M. Tetraethylammonium tetrafluoroborate (TEABF$_4$, > 99%) was purchased from BASF. Anhydrous acetonitrile (ACN, ≥ 99.9%) was purchased from J.T. Barker and stored in a solvent purification system (L.T. Technologies). Diethyl ether (anhydrous, ≥ 99%) was purchased from VWR. Cyclic voltammetry measurements and bulk electrolysis experiments were performed in a nitrogen filled drybox.

N-ethyl-3,7-dimethoxyphenothiazine (DMeOEPT),[14] *N*-ethyl-3,7-dimethylphenothiazine (DMeEPT),[32] 4,4,4-trimethoxytriphenylamine ((MeOPh)$_3$N),[35] *N*-ethylphenothiazine (EPT), *N*-ethyl-3,6-dimethoxycarbazole (DMeOECz),[36] *N*-ethyl-3,7-bis(trifluoromethyl)phenothiazine (BCF$_3$EPT),[37] (*N*-butylethylamino)cyclopropenium tetrafluoroborate (BECP-BF$_4$),[38] *N*-ethyl-3,7-dimethoxyphenothiazine tetrafluoroborate (DMeOEPT-BF$_4$),[14] *N*-ethyl-3,7-dimethylphenothiazine tetrafluoroborate (DMeEPT-BF4),[14] *N*-ethylphenothiazine (EPT-BF$_4$),[2] and *N*-ethyl-3,7-bis(trifluoromethyl)phenothiazine tetrafluoroborate (BCF$_3$EPT-BF$_4$)[37] were synthesized as previously reported.

***N*-ethyl-3,6-dimethoxycarbazole (DMeOECz).** A 250 mL round bottom flask was charged with 3,6-dibromo-*N*-ethylcarbazole (3.61 g, 10.2 mmol), NaOMe (8.82 g, 102 mmol), methanol (25 mL), pyridine (75 mL, 73 mmol), and CuI (7.82 g, 40.8 mmol) was added and reaction was refluxed overnight under nitrogen atmosphere. Upon completion of the reaction, the reaction mixture was diluted with EtOAc and washed with 1 M aq. HCl, water and brine. The combined organic phases were dried over anhydrous $MgSO_4$, filtered and crude mixture was concentrated by rotary evaporation. Finally, crude product was purified by silica gel column using 5% EtOAc in hexane mobile phase, which afforded 2.0 g (77%) of the pure product as a pale-yellow color crystalline solid. ^{1}H NMR (400 MHz, DMSO-*d6*) δ 7.71 (s, 2H), 7.41-7.48 (m, 2H), 7.02-7.08 (m, 2H), 4.35 (q, J = 6.8 Hz, 2H), 3.85 (s, 6H), 1.25 (t, J = 6.8, 3H). ^{13}C NMR (100 MHz, DMSO-*d6*) δ 152.7, 135.0, 122.35, 114.8, 109.7, 103.21, 55.61, 36.96, 13.68.

4,4,4-trimethoxytriphenylamine tetrafluoroborate ((MeOPh)₃N-BF₄). 4,4,4-trimethoxytriphenylamine (0.1 g, 0.3 mmol) and anhydrous dichloromethane (10 mL) was added to an oven dried 50 mL round bottomed flask and the mixture was cooled in an ice bath for 10 minutes while purging nitrogen. Then nitrosonium tetrafluoroborate (0.039 g, 0.33 mmol) was added to the prepared solution and stirred the mixture for 30 min under nitrogen. Upon completion of the reaction, anhydrous diethyl ether was added gradually with continued stirring. The resultant dark blue precipitate was filtered and dissolved in DCM (10 mL). Then the product was re-precipitated with anhydrous diethyl ether (10 mL). This process was repeated once more to ensure removal of any unreacted starting materials. The dark blue solid product (0.94 g, 75%) was dried under nitrogen and stored in an argon filled glovebox.

***N*-ethyl-3,6-dimethoxycarbazole tetrafluoroborate (DMeOECz-BF₄).** N-ethyl-3,7-dimethoxycarbazole (0.50 g, 1.9 mmol) and anhydrous acetonitrile (20 mL) were mixed together in an oven-dried 500 mL round bottomed flask. Then the reaction mixture was cooled in an ice bath. Then nitrosonium tetrafluoroborate (0.263 g, 2.25 mmol) was added to the reaction mixture and stirred for 30 minutes. Upon completion of the reaction, anhydrous diethyl ether was added gradually with continued stirring. The resultant dark

green precipitate was dissolved again in anhydrous acetonitrile and reprecipitated with anhydrous diethyl ether to remove unreacted starting materials. The dark green solid product (0.18 g, 45%) was dried under nitrogen and stored in an argon-filled glove box. Crystals for X-ray diffraction (XRD) were grown in DCM and diethyl ether. A saturated solution of salt in DCM (~0.3 mL) was placed in an NMR tube. Diethyl ether (~ 0.3 mL) was run down the side of the tube to form a discrete layer. The NMR tube was capped and kept in the freezer, and crystals were formed at the interface of the solvent layers.

1,4-ditertbutyl-2,5-dimethoxybenzene tetrafluoroborate (DDB-BF$_4$). DDB (0.51 g, 2.1 mmol) was dissolved in anhydrous dichloromethane (20 mL) in an oven-dried 100 mL round-bottomed flask fitted with a rubber septum under nitrogen atmosphere. Then round-bottomed flask was placed in an ice water bath for 10 min after which nitrosonium tetrafluroborate (0.297 g, 2.55 mmol) was added into resultant reaction mixture and stirred 20 min. Upon completion of the reaction, anhydrous diethyl ether (40 mL) was added gradually with continued stirring, resulting in a green precipitate. The precipitate was filtered under nitrogen, then it was further washed with anhydrous diethyl ether (40 mL). The light green solid product (0.45 g, 64%) was dried under nitrogen and stored in an argon filled glove box. To grow crystals of this product, a saturated solution of DDB-BF$_4$ salt in DCM (5 mL) was prepared in a septum sealed 20 mL glass vial. Then nitrogen gas was slowly purged to evaporate about 90% of the solvent over one hour and crystals were formed at the bottom of the vial.

(*N*-butylethylamino)cyclopropenium ditetrafluoroborate (BECP-(BF$_4$)$_2$). (0.20 g, 0.47 mmol) was dissolved in anhydrous dichloromethane (4 mL) in an oven-dried 20 mL glass vial fitted with a rubber septum under nitrogen atmosphere. Then glass vial was placed in an ice water bath for 10 min after which nitrosonium tetrafluroborate (67 mg, 0.57 mmol) was added into resultant reaction mixture and stirred 15 min. Upon completion of the reaction, anhydrous diethyl ether (10 mL) was added gradually with continued stirring, resulting in a red/orange precipitate. The solvents were removed through a cannula under a positive pressure. The resulting precipitate was further washed with anhydrous diethyl ether. The red solid product (95 mg, 40%) was dried under nitrogen and stored in an argon filled glove box.

5.5.2 Cyclic Voltammetry

Cyclic voltammetry (CV) experiments were performed using a 600D potentiostat (CH Instruments, Inc.) in a nitrogen-filled drybox. CVs were recorded in 0.1 TEABF$_4$/ACN at 1 mM active species with glassy carbon (CH Instruments, Inc.) as the working electrode, freshly anodized Ag/AgCl (CH Instruments, Inc.) as the reference electrode, and a Pt (CH Instruments, Inc.) wire as the counter electrode. Voltammograms were recorded at a scan rate of 100 mV s^{-1}. Ferrocene was used as an internal reference and the oxidation potential was calibrated with respect to ferrocene/ferrocenium ($Cp_2Fe^{0/+}$) redox couple. 100% iR correction was applied to compensate the solution resistance before recording CVs. The solution resistance was determined using iR compensation technique (CH Instruments 600D potentiostat). The resistance measured was ca.60 Ω, which leads a to correction of less than 5 mV at the highest measured current. The diffusion coefficients at 1 mM concentration of active species was calculated using Randles–Sevcik equation,[35]

$$i_p = 0.4463 \, nFAc \left(\frac{nFD}{RT} v \right)^{0.5}$$

where i_p is the peak current (A), n is the number of electrons transferred (-), F is the Faraday constant (96,485 C mol^{-1}), A is the electrode area (cm^2), c is the concentration (mol cm^{-3}), D is the diffusion coefficient (cm^{2}s^{-1}), R is the gas constant (8.314 J mol^{-1}K^{-1}), T is the absolute temperature (K), and v is the scan rate (V s^{-1}). The following scan rates were used for diffusion coefficient calculations: 25, 50, 75, 100, 200, 300, 400, and 500 mV s^{-1}.

5.5.3 UV-vis Spectroscopy

UV-vis spectra were obtained using optical glass cuvettes (Starna) with 1 or 10 mm path length on an Agilent 8453 diode array spectrophotometer. All the radical cation solutions were prepared in 0.1 M TEABF$_4$/ACN and transferred into cuvettes inside an argon filled glovebox. The capped cuvettes were taken out from the glove box for spectral analysis.

UV-vis study at different concentrations: MEEPT-BF$_4$ was dissolved in 0.1 M TEABF$_4$/ACN to prepare 0.1, 0.5, 1, 5 and 10 mM solutions. 0.1 and 0.5 mM radical cation

solutions were pipetted to 10 mm path length cuvettes while 1 mm path length cuvettes were utilized for 1, 5 and 10 mM radical cation solution analysis. UV-vis spectra were collected at 5, 15, 30, 60, 120, 180, 240, 300 min after preparing samples.

UV-vis study at 10 mM concentration: All radical cation salts (DMeOEPT-BF$_4$, DMeEPT-BF$_4$, (MeOPh)$_3$N-BF$_4$, EPT-BF$_4$, MEEPT-BF$_4$, DMeOECz-BF$_4$, BCF$_3$EPT-BF$_4$, DDB-BF$_4$, and (BECP-BF$_4$) -BF$_4$ were dissolved in 0.1 M TEABF$_4$/ACN at 10 mM and pipetted to 1 mm path length cuvettes. UV-vis spectra were collected at 5, 30, 60, 120, 180, 240, 300 min and 24 h after preparing samples.

5.5.4 Bulk electrolysis

Bulk electrolysis experiments were performed in custom made H cells as previously reported by Kowalski et al.[14] The H-cell has two electrolyte chambers separated by an ultra-fine porous glass frit (P5, Adams and Chittenden) which prevent the electrolyte mixing. Reticulated vitreous carbon (45 PPI, Duocell) served as the working and counter electrodes, which are placed in two chambers separately. Fritted Ag/Ag (cryptand)$^+$, contained 10 mM AgBF$_4$ in 0.1 M TEABF$_4$/ACN served as the reference electrode and it was placed next to the working electrode in the same chamber. In addition, a 3 mm-glassy carbon (CH Instruments, Inc.) electrode was attached to the working electrode chamber to record CVs, before and after bulk electrolysis experiments. 3.5 mL of electrolytes comprised of 10 mM neutral active species (MEEPT, DMeOECz, DDB, and BECP-BF$_4$) in 0.1 M TEABF$_4$/ACN were added to the both working and counter electrode chambers for charge-discharge cycling. The voltage cut-offs were determined after recording CVs on the working electrode side to avoid accessing undesired redox couples or electrolyte decomposition. The voltage boundaries for each active species as follows; MEEPT: 0.65-0 V, DMeOECz: 0.76-0.16 V, DDB: 1.1-0.45, and BECP-BF$_4$: 1.2-0.55 V vs. Ag/Ag$^+$. Both the working and counter electrode chambers were continuously stirred during bulk electrolysis cycling to maintain a good mass transfer while charging and discharging. The experiment was conducted at variable C rates, including 3C (2.814 mA), 2C (1.876 mA), and 1C (0.938 mA) by connecting to a BioLogic VSP potentiostat.

CHAPTER 6. CONCLUSIONS AND FUTURE DIRECTIONS

6.1   Summary

In this thesis, a set of new organic redox active molecules was developed and tested for application in nonaqueous redox flow batteries. Molecular design was approached by introducing a series of novel and robust molecular engineering principles to enhance physicochemical properties (solubility, stability, and redox potential), thus improving battery performance. The performance of developed materials was screened through a series of electroanalytical and spectroscopic methods including cyclic voltammetry, UV-vis spectroscopy, bulk electrolysis, and flow cell cycling.

Developing redox active organic molecules with permanently charged substituents was introduced as a viable method of increasing the solubility of active species by eliminating the requirement of supporting salt for flow battery studies. The results in Chapter 2 showed that permanently charged substituents keep ionic conductivity high while at the same time increasing the solubility of an ionic phenothiazine and an ionic viologen across all states of charge. The conductivity, viscosity, and diffusivity analysis of active species revealed that newly developed materials can be utilized in supporting-salt-free flow cell cycling, opening a new avenue to improve two performance aspects with one molecular modification. In addition to the solubility, multi-electron-transferring redox active species further increases the capacity and energy density of RFBs. Two new two-electron-donating phenothiazines were investigated in the Chapter 3. A new two-electron donating phenothiazine was sufficiently soluble in nonaqueous electrolytes and it was capable in providing 1 M electron to the flow battery system. Importantly, symmetric flow cell analysis of this species introduced challenges in employing multiple electron transfer materials in the flow cell environment. Molecular designing and chemical environment optimization towards increased solubility resulted in robust, high voltage phenothiazine derivatives for energy storage applications. Chapter 4 demonstrated the utilization of the effects of electron-withdrawing groups and sterically hindered groups to constructively increase the oxidation potential of phenothiazine. Further, isolation of an X-ray quality crystal of radical cation salt of the high voltage phenothiazine confirmed the substantial stability of its charged form in some situations. Generally, the charged forms of organic

redox materials are more reactive than their neutral counterparts, thus capacity retention or coulombic efficiency of RFBs is determined by the chemical stability of the charged species. The results from Chapter 5 showed charged species derived from the low oxidation potential posolytes have a higher chemical stability over time compared to the charged species derived from higher oxidation potential posolytes. Further, this study discussed challenges in utilizing high oxidation potential compounds in nonaqueous RFBs.

6.2 Future work

The development of novel, robust, inexpensive redox active species are indeed necessary for the growth of nonaqueous RFBs, as they are still in their infancy. Redox active organic molecules show promising features towards low-cost RFBs as they comprised of earth abundant elements (e.g. carbon, oxygen, and hydrogen). Therefore, a focus on developing highly soluble and highly stable organic redox active materials would up lift the current status of RFB performance.

Flow cells operating at high concentrations may experience poor capacity retention even when active materials are chemically stable. This could arise due to the high cell polarization. At high concentrations, the viscosity of the electrolyte system could be considerably high as they approach to their saturation point, resulting in a rise in cell resistance due to mass transfer limitations. Therefore, researchers should focus on increasing solubility of active species across the all states of charge without significantly increasing their viscosity. This could be achieved through introducing appropriate functional groups to the redox active cores and screening the viscosity of a series of commercially available supporting salts in the presence and absence of active materials. However, as discussed in this thesis, high concentrations of supporting salt could be problematic when flow cells are operating at 3-4 M concentration of active species. Thus, research field should be more focused on the developing stable, ionic conductive redox active materials while keeping viscosity low to operate supporting-salt-free systems.

Although developing multi-electron transfer materials are interested as a feasible method of increasing the capacity and energy density of flow batteries, such materials are required to have an equal chemical stability at each state of charge to achieve stable capacity retention in flow cell cycling. Therefore, it is necessary to quantify and improve the

chemical stability of redox active materials in each states of charge. Multi-electron-transfer materials with considerably high potential separation could be of interest as bipolar active materials to be operated in symmetric RFB as a solution for the active species crossover. However, threshold potential separations need to be quantified in electrochemical analysis to mainatin the flow cell efficiencies.

Indeed, the community should focus more on developing high oxidation potential posolytes and low reduction potential negolytes to get the advantage of nonaqueous solvents/electrolytes. The charged forms of high oxidation potential compounds are highly reducing, and more studies are required to understand the source of electron present in the electrolyte system to prevent the electron-transfer reactions, thus improve the efficiency of RFBs. The chemical stability of charged forms of posolytes could depend on the identity of the anion. Thus, designing systematic studies to evaluate the effect of the anion/s on the chemical stability of high oxidation potential posolytes would open a new avenue in the field of redox chemistry to enhance the performance of high-open-circuit voltage RFBs. Further, chemical stability of redox active species (charged forms) should be evaluated at the concentration of active species that could operate in a real flow battery conditions due to the following. (i). At low concentrations, trace solvent/electrolyte impurities may play a role on the stability. (ii). Analysis at high concentrations would help to understand the effect of aggregation/ion-pair formation on the stability.

Beyond the redox active organic materials presented in this thesis, indeed, the possibilities are endless as the organic nonaqueous RFB field is only about a decade old. Thus, exploring new materials would help to further enhance the physicochemical properties (solubility, stability, and redox potential) of active species, aiming to design high energy, long lasting, and affordable RFB technology.

REFERENCES

Chapter 1

1. IEA, Global Energy & CO2 Status Report 2019. International Energy Agency: 2019.

2. What is U.S. electricity generation by energy source. https://www.eia.gov/tools/faqs/faq.php?id=427&t=3.

3. Brockway, P. E.; Owen, A.; Brand-Correa, L. I.; Hardt, L., Estimation of global final-stage energy-return-on-investment for fossil fuels with comparison to renewable energy sources. *Nat. Energy* **2019,** *4*, 612-621.

4. CIA World Factbook. https://www.cia.gov/library/publications/the-world-factbook/geos/xx.html.

5. Su, L.; Kowalski, J. A.; Carroll, K. J.; Brushett, F. R., Recent Developments and Trends in Redox Flow Batteries. In *Green Energy Tech.*, 2015; Vol. 172, pp 673-712.

6. Cerling, T. E.; Dearing, M. D.; Ehleringer, J. R., *A History of Atmospheric CO2 and its Effects on pPants, Animals, and Ecosystems*. Springer: 2005.

7. Leung, P.; Shah, A. A.; Sanz, L.; Flox, C.; Morante, J. R.; Xu, Q.; Mohamed, M. R.; Ponce de Leon, C.; Walsh, F. C., Recent Developments in Organic Redox Flow Batteries: A Critical Review. *J. Power Sources* **2017,** *360*, 243-283.

8. Kowalski, J. A.; Su, L.; Milshtein, J. D.; Brushett, F. R., Recent Advances in Molecular Engineering of Redox Active Organic Molecules for Nonaqueous Flow Batteries. *Curr. Opin. Chem. Eng.* **2016,** *13*, 45-52.

9. Edenhofer, O.; Seyboth, K.; Creutzig, F.; Schlömer, S., On the Sustainability of Renewable Energy Sources. *Annual Review of Environment and Resources* **2013,** *38*, 169-200.

10. Weitemeyer, S.; Kleinhans, D.; Vogt, T.; Agert, C., Integration of Renewable Energy Sources in future power systems: The role of storage. *Renewable Energy* **2015,** *75*, 14-20.

11. U.S. DOE (2019) Global Energy Storage Database Projects. **2019**.

12. Grid Energy Storage, U.S. Department of Energy. **2013**.

13. Akhil, A. A. H., G.; Currier, A. B.; Kaun, B. C.; Rastler, D. M.; Chen, S. B.; Cotter, A.; L.; Bradshaw, D. T. G., W. D. , DOE/EPRI 2013 Electricity Storage Handbook in Collaboration with NRECA. EdAlbuq. NM Sandia Natl. Lab.
. **2013**.

14. Milshtein, J. D.; Kaur, A. P.; Casselman, M. D.; Kowalski, J. A.; Modekrutti, S.; Zhang, P. L.; Attanayake, N. H.; Elliott, C. F.; Parkin, S. R.; Risko, C.; Brushett, F. R.; Odom, S.

A., High Current Density, Long Duration Cycling of Soluble Organic Active Species for Non-Aqueous Redox Flow Batteries. *Energy Environ. Sci.* **2016,** *9*, 3531-3543.

15. Milshtein, J. D.; Barton, J. L.; Darling, R. M.; Brushett, F. R., 4-Acetamido-2,2,6,6-tetramethylpiperidine-1-oxyl as a Model Organic Redox Active Compound for Nonaqueous Flow Batteries. *J. Power Sources* **2016,** *327*, 151-159.

16. Duan, W.; Huang, J.; Kowalski, J. A.; Shkrob, I. A.; Vijayakumar, M.; Walter, E.; Pan, B.; Yang, Z.; Milshtein, J. D.; Li, B.; Liao, C.; Zhang, Z.; Wang, W.; Liu, J.; Moore, J. S.; Brushett, F. R.; Zhang, L.; Wei, X., "Wine-Dark Sea" in an Organic Flow Battery: Storing Negative Charge in 2,1,3-Benzothiadiazole Radicals Leads to Improved Cyclability. *ACS Energy Lett.* **2017,** *2* (5), 1156-1161.

17. Elgammal, R. A.; Tang, Z.; Sun, C.-N.; Lawton, J.; Zawodzinski, T. A., Species Uptake and Mass Transport in Membranes for Vanadium Redox Flow Batteries. *Electrochim. Acta* **2017,** *237*, 1-11.

18. Kim, S.; Thomsen, E.; Xia, G.; Nie, Z.; Bao, J.; Recknagle, K.; Wang, W.; Viswanathan, V.; Luo, Q.; Wei, X., 1 kW/1 kWh advanced vanadium redox flow battery utilizing mixed acid electrolytes. *J. Power Sources* **2013,** *237*, 300-309.

19. Wang, Y.; He, P.; Zhou, H., Li-Redox Flow Batteries Based on Hybrid Electrolytes: At the Cross Road between Li-ion and Redox Flow Batteries. *Advanced Energy Materials* **2012,** *2*, 770-779.

20. Khor, A.; Leung, P.; Mohamed, M.; Flox, C.; Xu, Q.; An, L.; Wills, R.; Morante, J.; Shah, A., Review of zinc-based hybrid flow batteries: From fundamentals to applications. *Mater. today energy* **2018,** *8*, 80-108.

21. Hagedorn, N. H. *NASA Redox Storage System Development Project. Final Report*; National Aeronautics and Space Administration, Cleveland, OH (USA). Lewis …: 1984.

22. Rychcik, M.; Skyllas-Kazacos, M., Characteristics of a New All-Vanadium Redox Flow Battery. *Journal of Power Sources* **1988,** *22*, 59-67.

23. Skyllas-Kazacos, M.; Rychcik, M.; Robins, R. G.; Fane, A.; Green, M., New All-Vanadium Redox Flow Cell. *Journal of the Electrochemical Society* **1986,** *133*, 1057.

24. Darling, R. M.; Gallagher, K. G.; Kowalski, J. A.; Ha, S.; Brushett, F. R., Pathways to Low-Cost Electrochemical Energy Storage: A Comparison of Aqueous and Nonaqueous Flow Batteries. *Energy Environ. Sci.* **2014,** *7*, 3459-3477.

25. Cho, J.; Jeong, S.; Kim, Y., Commercial and Research Battery Technologies for Electrical Energy Storage Applications. *PROG ENERG COMBUST* **2015,** *48*, 84-101.

26. Gong, K.; Fang, Q.; Gu, S.; Li, S. F. Y.; Yan, Y., Nonaqueous Redox-Flow Batteries: Organic Solvents, Supporting Electrolytes, and Redox Pairs. *Energy Environ. Sci.* **2015,** *8*, 3515-3530.

27. Vanysek, P., *CRC Handbook of Chemistry and Physics*. 1998; Vol. 87.

28. Hazza, A.; Pletcher, D.; Wills, R., A Novel flow Battery: A Lead Acid Battery Based on an Electrolyte with Soluble Lead (II) Part I. Preliminary Studies. *Phys Chem Chem Phys* **2004,** *6*, 1773-1778.

29. Singh, P., Application of non-aqueous solvents to batteries. *J. Power Sources* **1984,** *11* (1-2), 135-142.

30. Singh, P., Application of non-aqueous solvents to batteries. *J. power sources* **1984,** *11*, 135-142.

31. Xu, K., Nonaqueous liquid electrolytes for lithium-based rechargeable batteries. *Chem. rev.* **2004,** *104*, 4303-4418.

32. Yan, Y.; Robinson, S. G.; Sigman, M. S.; Sanford, M. S., Mechanism-Based Design of a High-Potential Catholyte Enables a 3.2 V All-Organic Nonaqueous Redox Flow Battery. *J. Am. Chem. Soc.* **2019,** *141*, 15301-15306.

33. Iyer, V. A.; Schuh, J. K.; Montoto, E. C.; Nemani, V. P.; Qian, S.; Nagarjuna, G.; Rodríguez-López, J.; Ewoldt, R. H.; Smith, K. C., Assessing the Impact of Electrolyte Conductivity and Viscosity on the Reactor Cost and Pressure Drop of Redox-Active Polymer Flow Batteries. *J. Power Sources* **2017,** *361*, 334-344.

34. Brushett, F. R.; Vaughey, J. T.; Jansen, A. N., An All-Organic Non-aqueous Lithium-ion Redox Flow Battery. *Adv. Energy Mater.* **2012,** *2*, 1390-1396.

35. Park, M.; Beh, E. S.; Fell, E. M.; Jing, Y.; Kerr, E. F.; De Porcellinis, D.; Goulet, M. A.; Ryu, J.; Wong, A. A.; Gordon, R. G., A high voltage aqueous zinc–organic hybrid flow battery. *Adv. Energy Mater.* **2019,** *9*, 1900694.

36. Zhang, J.; Huang, J.; Robertson, L. A.; Shkrob, I. A.; Zhang, L., Comparing Calendar and Cycle Life Stability of Redox Active Organic Molecules for Nonaqueous Redox Flow Batteries. *J. Power Sources* **2018,** *397*, 214-222.

37. Milshtein, J. D.; Fisher, S. L.; Breault, T. M.; Thompson, L. T.; Brushett, F. R., Feasibility of a Supporting-Salt-Free Nonaqueous Redox Flow Battery Utilizing Ionic Active Materials. *ChemSusChem* **2017,** *10*, 2080-2088.

38. Dmello, R.; Milshtein, J. D.; Brushett, F. R.; Smith, K. C., Cost-driven Materials Selection Criteria for Redox Flow Battery Electrolytes. *J. Power Sources* **2016,** *330*, 261-272.

39. Li, B.; Li, L.; Wang, W.; Nie, Z.; Chen, B.; Wei, X.; Luo, Q.; Yang, Z.; Sprenkle, V., Fe/V Redox Flow Battery Electrolyte Investigation and Optimization. *J. Power Sources* **2013,** *229*, 1-5.

40. Stephenson, D.; Kim, S.; Chen, F.; Thomsen, E.; Viswanathan, V.; Wang, W.; Sprenkle, V., Electrochemical Model of the Fe/V Redox Flow Battery. *J. Electrochem. Soc.* **2012,** *159*, A1993-A2000.

41. Xu, Q.; Zhao, T. S.; Wei, L.; Zhang, C.; Zhou, X. L., Electrochemical Characteristics and Transport Properties of Fe(II)/Fe(III) Redox Couple in a Non-aqueous Reline Deep Eutectic Solvent. *Electrochim. Acta* **2015,** *154*, 462-467.

42. Hwang, S.; Kim, H.-s.; Ryu, J. H.; Oh, S. M., Ni(II)-Chelated Thio-crown Complex as a Single Redox Couple for Non-Aqueous Flow Batteries. *Electrochem. Commun.* **2017,** *85*, 36-39.

43. Xie, C.; Zhang, H.; Xu, W.; Wang, W.; Li, X., A Long Cycle Life, Self-Healing Zinc–Iodine Flow Battery with High Power Density. *Angew. Chem. Int. Ed.* **2018**.

44. Selverston, S.; Savinell, R. F.; Wainright, J. S., Zinc-Iron Flow Batteries with Common Electrolyte. *J. Electrochem. Soc.* **2017,** *164*, A1069-A1075.

45. Liu, W.; Liu, Y.; Zhang, H.; Xie, C.; Shi, L.; Zhou, Y.-G.; Li, X., A Highly Stable Neutral Viologen/Bromine Aqueous Flow Battery with High Energy and Power Density. *Chem. Comm.* **2019**.

46. Oh, K.; Kang, T. J.; Park, S.; Tucker, M. C.; Weber, A. Z.; Ju, H., Effect of Flow-Field Structure on Discharging and Charging Behavior of Hydrogen/Bromine Redox Flow Batteries. *Electrochim. Acta* **2017,** *230*, 160-173.

47. Cabrera, P. J.; Yang, X.; Suttil, J. A.; Brooner, R. E. M.; Thompson, L. T.; Sanford, M. S., Evaluation of Tris-Bipyridine Chromium Complexes for Flow Battery Applications: Impact of Bipyridine Ligand Structure on Solubility and Electrochemistry. *Inorg. Chem.* **2015,** *54*, 10214-10223.

48. Bae, C.-H.; Roberts, E.; Dryfe, R., Chromium Redox Couples for Application to Redox Flow Batteries. *Electrochim. Acta* **2002,** *48*, 279-287.

49. Hwang, S.; Kim, H.-s.; Ryu, J. H.; Oh, S. M., N-ferrocenylphthalimide; A Single Redox Couple formed by attaching a Ferrocene Moiety to Phthalimide for Non-Aqueous Flow Batteries. *J. Power Sources* **2018,** *395*, 60-65.

50. Mai, Z.; Zhang, H.; Li, X.; Bi, C.; Dai, H., Sulfonated Poly(tetramethydiphenyl ether ether ketone) Membranes for Vanadium Redox Flow Battery Application. *J. Power Sources* **2011,** *196*, 482-487.

51. Burgess, M.; Moore, J. S.; Rodriguez-Lopez, J., Redox Active Polymers as Soluble Nanomaterials for Energy Storage. *Acc Chem Res* **2016,** *49*, 2649-2657.

52. Montoto, E. C.; Nagarjuna, G.; Hui, J.; Burgess, M.; Sekerak, N. M.; Hernandez-Burgos, K.; Wei, T. S.; Kneer, M.; Grolman, J.; Cheng, K. J.; Lewis, J. A.; Moore, J. S.;

Rodriguez-Lopez, J., Redox Active Colloids as Discrete Energy Storage Carriers. *J. Am. Chem. Soc.* **2016,** *138*, 13230-13237.

53. Critical Mineral Resources of the United States—Economic and Environmental Geology and Prospects for Future Supply. USGS, Ed. https://pubs.usgs.gov/pp/1802/u/pp1802u.pdf: 2017.

54. Yang, Z.; Tong, L.; Tabor, D. P.; Beh, E. S.; Goulet, M.-A.; Porcellinis, D.; Aspuru-Guzik, A.; Gordon, R. G.; Aziz, M. J., Alkaline Benzoquinone Aqueous Flow Battery for Large-Scale Storage of Electrical Energy. *Adv. Energy Mater.* **2018,** *8*, 1702056.

55. Huskinson, B.; Marshak, M. P.; Suh, C.; Er, S.; Gerhardt, M. R.; Galvin, C. J.; Chen, X.; Aspuru-Guzik, A.; Gordon, R. G.; Aziz, M. J., A Metal-Free Organic-Inorganic Aqueous Flow Battery. *Nature* **2014,** *505*, 195-198.

56. Liu, Y.; Goulet, M.-A.; Tong, L.; Liu, Y.; Ji, Y.; Wu, L.; Gordon, R. G.; Aziz, M. J.; Yang, Z.; Xu, T., A Long Lifetime All-Organic Aqueous Flow Battery Utilizing TMAP-TEMPO Radical. *Chem* **2019,** *5*, 1861-1870.

57. Hollas, A.; Wei, X.; Murugesan, V.; Nie, Z.; Li, B.; Reed, D.; Liu, J.; Sprenkle, V.; Wang, W., A Biomimetic High-capacity Phenazine-Based Anolyte for Aqueous Organic Redox Flow Batteries. *Nat. Energy* **2018,** *3*, 508-514.

58. Sevov, C. S.; Samaroo, S. K.; Sanford, M. S., Cyclopropenium Salts as Cyclable, High-Potential Catholytes in Nonaqueous Media. *Adv. Energy Mater.* **2017,** *7*, 1602027-1602032.

59. Sevov, C. S.; Brooner, R. E.; Chenard, E.; Assary, R. S.; Moore, J. S.; Rodriguez-Lopez, J.; Sanford, M. S., Evolutionary Design of Low Molecular Weight Organic Anolyte Materials for Applications in Nonaqueous Redox Flow Batteries. *J. Am. Chem. Soc.* **2015,** *137*, 14465-72.

60. DeBruler, C.; Hu, B.; Moss, J.; Luo, J.; Liu, T. L., A Sulfonate-Functionalized Viologen Enabling Neutral Cation Exchange, Aqueous Organic Redox Flow Batteries toward Renewable Energy Storage. *ACS Energy Lett.* **2018,** *3*, 663-668.

61. Attanayake, N. H.; Kowalski, J. A.; Greco, K.; Casselman, M. D.; Milshtein, J. D.; Chapman, S. J.; Parkin, S. R.; Brushett, F. R.; Odom, S. A., Tailoring Two-Electron Donating Phenothiazines to Enable High Concentration Redox Electrolytes for Use in Nonaqueous Redox Flow Batteries. *Chem. Mater.* **2019,** *31*, 4353-4363.

62. Kwon, G.; Lee, K.; Lee, M. H.; Lee, B.; Lee, S.; Jung, S.-K.; Ku, K.; Kim, J.; Park, S. Y.; Kwon, J. E., Bio-inspired Molecular Redesign of a Multi-redox Catholyte for High-Energy Non-aqueous Organic Redox Flow Batteries. *Chem* **2019,** *5*, 2642-2656.

63. Kwon, G.; Lee, S.; Hwang, J.; Shim, H.-S.; Lee, B.; Lee, M. H.; Ko, Y.; Jung, S.-K.; Ku, K.; Hong, J., Multi-redox Molecule for High-Energy Redox Flow Batteries. *Joule* **2018,** *2*, 1771-1782.

64. Robinson, S. G.; Yan, Y.; Hendriks, K. H.; Sanford, M. S.; Sigman, M. S., Developing a predictive solubility model for monomeric and oligomeric cyclopropenium-based flow battery catholytes. *J. Am. Chem. Soc.* **2019**, *141*, 10171-10176.

65. Geysens, P.; Li, Y.; Vankelecom, I.; Fransaer, J.; Binnemans, K., Highly Soluble 1,4-Diaminoanthraquinone Derivative for Nonaqueous Symmetric Redox Flow Batteries. *ACS Sustain. Chem. Eng.* **2020,** *8*, 3832-3843.

66. Chai, J.; Lashgari, A.; Cao, Z.; Williams, C. K.; Wang, X.; Dong, J.; Jiang, J. J., PEGylation-Enabled Extended Cyclability of a Non-Aqueous Redox Flow Battery. *ACS Appl. Mater. Interfaces* **2020**.

67. Kaur, A. P.; Holubowitch, N. E.; Ergun, S.; Elliott, C. F.; Odom, S. A., A Highly Soluble Organic Catholyte for Non-aqueous Redox Flow Batteries. *Energy Technol.* **2015,** *3*, 476-480.

68. Kowalski, J. A.; Casselman, M. D.; Kaur, A. P.; Milshtein, J. D.; Elliott, C. F.; Modekrutti, S.; Attanayake, N. H.; Zhang, N.; Parkin, S. R.; Risko, C.; Brushett, F. R.; Odom, S. A., A Stable Two-Electron-Donating Phenothiazine for Application in Nonaqueous Redox Flow Batteries. *J. Mater. Chem. A* **2017,** *5*, 24371-24379.

69. Chen, R., Toward High-Voltage, Energy-Dense and Durable Aqueous Organic Redox Flow Batteries: Role of the Supporting Electrolytes. *ChemElectroChem*.

70. Dai, G.; Gao, Y.; Niu, Z.; He, P.; Zhang, X.; Zhao, Y.; Zhou, H., Promote the Voltage of Organic Cathode Materials by Diluting the Electron Density in the π-Conjugated Skeleton. *ChemSusChem* **2020**.

71. Casselman, M. D.; Elliott, C. F.; Modekrutti, S.; Zhang, P. L.; Parkin, S. R.; Risko, C.; Odom, S. A., Beyond the Hammett Effect: Using Strain to Alter the Landscape of Electrochemical Potentials. *Chemphyschem* **2017,** *18*, 2142-2146.

72. Haddon, R., Chemistry of the Fullerenes: The Manifestation of Strain in a Cass of Continuous Aromatic Molecules. *Science* **1993,** *261*, 1545-1550.

73. Chen, Q.; Trinh, M. T.; Paley, D. W.; Preefer, M. B.; Zhu, H.; Fowler, B. S.; Zhu, X.-Y.; Steigerwald, M. L.; Nuckolls, C., Strain-Induced Stereoselective Formation of Blue-Emitting Cyclostilbenes. *J. Am. Chem. Soc.* **2015,** *137*, 12282-12288.

Chapter 2

1. Gong, K.; Fang, Q.; Gu, S.; Li, S. F. Y.; Yan, Y., Nonaqueous Redox-Flow Batteries: Organic Solvents, Supporting Electrolytes, and Redox Pairs. *Energy Environ. Sci.* **2015,** *8*, 3515-3530.

2. LOBO, V. M.; Quaresma, J., Handbook of electrolyte solutions. B. *Physical sciences data* **1989,** *41*.

3. Milshtein, J. D.; Kaur, A. P.; Casselman, M. D.; Kowalski, J. A.; Modekrutti, S.; Zhang, P. L.; Attanayake, N. H.; Elliott, C. F.; Parkin, S. R.; Risko, C.; Brushett, F. R.; Odom, S. A., High Current Density, Long Duration Cycling of Soluble Organic Active Species for Non-Aqueous Redox Flow Batteries. *Energy Environ. Sci.* **2016,** *9*, 3531-3543.

4. Laramie, S. M.; Milshtein, J. D.; Breault, T. M.; Brushett, F. R.; Thompson, L. T., Performance and Cost Characteristics of Multi-Electron Transfer, Common ion Exchange Non-aqueous Redox Flow Batteries. *J. Power Sources* **2016,** *327*, 681-692.

5. Milshtein, J. D.; Barton, J. L.; Carney, T. J.; Kowalski, J. A.; Darling, R. M.; Brushett, F. R., Towards Low Resistance Nonaqueous Redox Flow Batteries. *J. Electrochem. Soc.* **2017,** *164*, A2487-A2499.

6. Darling, R. M.; Gallagher, K. G.; Kowalski, J. A.; Ha, S.; Brushett, F. R., Pathways to Low-Cost Electrochemical Energy Storage: A Comparison of Aqueous and Nonaqueous Flow Batteries. *Energy Environ. Sci.* **2014,** *7*, 3459-3477.

7. Dmello, R.; Milshtein, J. D.; Brushett, F. R.; Smith, K. C., Cost-driven Materials Selection Criteria for Redox Flow Battery Electrolytes. *J. Power Sources* **2016,** *330*, 261-272.

8. Milshtein, J. D.; Fisher, S. L.; Breault, T. M.; Thompson, L. T.; Brushett, F. R., Feasibility of a Supporting-Salt-Free Nonaqueous Redox Flow Battery Utilizing Ionic Active Materials. *ChemSusChem* **2017,** *10* (9), 2080-2088.

9. Bate, A. B.; Kalin, J. H.; Fooksman, E. M.; Amorose, E. L.; Price, C. M.; Williams, H. M.; Rodig, M. J.; Mitchell, M. O.; Cho, S. H.; Wang, Y., Synthesis and Antitubercular Activity of Quaternized Promazine and Promethazine Derivatives. *Bioorg. Med. Chem. Lett.* **2007,** *17* (5), 1346-1348.

10. Krause, L.; Herbst-Irmer, R.; Sheldrick, G. M.; Stalke, D., Comparison of Silver and Molybdenum Microfocus X-ray Sources for Single-Crystal Structure Determination. *J. Appl. Crystallogr.* **2015,** *48*, 3-10.

11. Sheldrick, G. M., SHELXT–Integrated Space-Group and Crystal-Structure Determination. *Acta Crystallogr. A* **2015,** *71*, 3-8.

12. Sheldrick, G. M., Crystal Structure Refinement with SHELXL. *Acta Crystallogr. C* **2015,** *71*, 3-8.

13. Wilson, A. J. C., *International Tables for Crystallography: Mathematical, Physical, and Chemical Tables*. International Union of Crystallography: 1992; Vol. C.

14. Iyer, V. A.; Schuh, J. K.; Montoto, E. C.; Nemani, V. P.; Qian, S.; Nagarjuna, G.; Rodríguez-López, J.; Ewoldt, R. H.; Smith, K. C., Assessing the Impact of Electrolyte

Conductivity and Viscosity on the Reactor Cost and Pressure Drop of Redox-Active Polymer Flow Batteries. *J. Power Sources* **2017,** *361*, 334-344.

15. Zhang, J.; Corman, R. E.; Schuh, J. K.; Ewoldt, R. H.; Shkrob, I. A.; Zhang, L., Solution Properties and Practical Limits of Concentrated Electrolytes for Nonaqueous Redox Flow Batteries. *J. Phys. Chem. C* **2018,** *122* (15), 8159-8172.

16. Edward, J. T., Molecular Volumes and the Stokes-Einstein Equation. *J. Chem. Educ.* **1970,** *47*, 261-270.

17. Compton, R. G.; Banks, C. E., *Understanding Voltammetry.* 2nd ed.; Imperial College Press, London: 2011.

18. Narayana, K. A.; Casselman, M. D.; Elliott, C. F.; Ergun, S.; Parkin, S. R.; Risko, C.; Odom, S. A., N-Substituted Phenothiazine Derivatives: How the Stability of the Neutral and Radical Cation Forms Affects Overcharge Performance in Lithium-ion Batteries. *ChemPhysChem* **2015,** *16*, 1179-1189.

19. Kowalski, J. A.; Casselman, M. D.; Kaur, A. P.; Milshtein, J. D.; Elliott, C. F.; Modekrutti, S.; Attanayake, N. H.; Zhang, N.; Parkin, S. R.; Risko, C.; Brushett, F. R.; Odom, S. A., A Stable Two-Electron-Donating Phenothiazine for Application in Nonaqueous Redox Flow Batteries. *J. Mater. Chem. A* **2017,** *5*, 24371-24379.

20. Attanayake, N. H.; Kowalski, J. A.; Greco, K. V.; Casselman, M. D.; Milshtein, J. D.; Chapman, S. J.; Parkin, S. R.; Brushett, F. R.; Odom, S. A., Tailoring Two-Electron-Donating Phenothiazines To Enable High-Concentration Redox Electrolytes for Use in Nonaqueous Redox Flow Batteries. *Chem. Mater.* **2019,** *31*, 4353-4363.

21. Kaur, A. P.; Harris, O. C.; Attanayake, N. H.; Liang, Z.; Parkin, S. R.; Tang, M. H.; Odom, S. A., Quantifying Environmental Effects on the Solution and Solid-State Stability of a Phenothiazine Radical Cation. *Chem. Mater.* **2020,** *32*, 3007-3017.

22. Hammett, L. P., The Effect of Structure Upon the Reactions of Organic Compounds. Benzene Derivatives. *J. Am. Chem. Soc.* **1937,** *59*, 96-103.

23. Sanford, M.; Shrestha, A.; Hendriks, K.; Sigman, M.; Minteer, S., Realization of an Asymmetric Non-Aqueous Redox Flow Battery Through Molecular Design to Minimize Active Species Crossover and Decomposition. *Chemistry – A European Journal* **2020,** *n/a* (n/a).

24. Milshtein, J. D.; Barton, J. L.; Darling, R. M.; Brushett, F. R., 4-Acetamido-2,2,6,6-tetramethylpiperidine-1-oxyl as a Model Organic Redox Active Compound for Nonaqueous Flow Batteries. *J. Power Sources* **2016,** *327*, 151-159.

25. Hudak, N. S.; Small, L. J.; Pratt, H. D.; Anderson, T. M., Through-Plane Conductivities of Membranes for Nonaqueous Redox Flow Batteries. *J. Electrochem. Soc.* **2015,** *162*, A2188-A2194.

26. Duan, W.; Huang, J.; Kowalski, J. A.; Shkrob, I. A.; Vijayakumar, M.; Walter, E.; Pan, B.; Yang, Z.; Milshtein, J. D.; Li, B.; Liao, C.; Zhang, Z.; Wang, W.; Liu, J.; Moore, J. S.; Brushett, F. R.; Zhang, L.; Wei, X., "Wine-Dark Sea" in an Organic Flow Battery: Storing Negative Charge in 2,1,3-Benzothiadiazole Radicals Leads to Improved Cyclability. *ACS Energy Lett.* **2017,** *2* (5), 1156-1161.

27. Huang, J.; Pan, B.; Duan, W.; Wei, X.; Assary, R. S.; Su, L.; Brushett, F. R.; Cheng, L.; Liao, C.; Ferrandon, M. S.; Wang, W.; Zhang, Z.; Burrell, A. K.; Curtiss, L. A.; Shkrob, I. A.; Moore, J. S.; Zhang, L., The Lightest Organic Radical Cation for Charge Storage in Redox Flow Batteries. *Sci. Rep.* **2016,** *6*, 32102-32111.

28. Vaid, T. P.; Sanford, M. S., An Organic Super-Electron-Donor as a High Energy Density Negative Electrolyte for Nonaqueous Flow Batteries. *Chem. Comm.* **2019,** *55* (74), 11037-11040.

29. Goulet, M.-A.; Tong, L.; Pollack, D. A.; Tabor, D. P.; Odom, S. A.; Aspuru-Guzik, A.; Kwan, E. E.; Gordon, R. G.; Aziz, M. J., Extending the Lifetime of Organic Flow Batteries via Redox State Management. *J. Am. Chem. Soc.* **2019,** *141*, 8014-8019.

30. Wei, X.; Li, B.; Wang, W., Porous Polymeric Composite Separators for Redox Flow Batteries. *Polym. Rev.* **2015,** *55* (2), 247-272.

31. Rodby, K. E.; Carney, T. J.; Gandomi, Y. A.; Barton, J. L.; Darling, R. M.; Brushett, F. R., Assessing the levelized cost of vanadium redox flow batteries with capacity fade and rebalancing. *Journal of Power Sources* **2020**, 227958.

Chapter 3

1. Milshtein, J. D.; Kaur, A. P.; Casselman, M. D.; Kowalski, J. A.; Modekrutti, S.; Zhang, P. L.; Attanayake, N. H.; Elliott, C. F.; Parkin, S. R.; Risko, C.; Brushett, F. R.; Odom, S. A., High Current Density, Long Duration Cycling of Soluble Organic Active Species for Non-Aqueous Redox Flow Batteries. *Energy Environ. Sci.* **2016,** *9*, 3531-3543.

2. Kowalski, J. A.; Casselman, M. D.; Kaur, A. P.; Milshtein, J. D.; Elliott, C. F.; Modekrutti, S.; Attanayake, N. H.; Zhang, N.; Parkin, S. R.; Risko, C.; Brushett, F. R.; Odom, S. A., A Stable Two-Electron-Donating Phenothiazine for Application in Nonaqueous Redox Flow Batteries. *J. Mater. Chem. A* **2017,** *5*, 24371-24379.

3. Narayana, K. A.; Casselman, M. D.; Elliott, C. F.; Ergun, S.; Parkin, S. R.; Risko, C.; Odom, S. A., N-Substituted Phenothiazine Derivatives: How the Stability of the Neutral and Radical Cation Forms Affects Overcharge Performance in Lithium-ion Batteries. *ChemPhysChem* **2015,** *16*, 1179-1189.

4. Ergun, S.; Elliott, C. F.; Kaur, A. P.; Parkin, S. R.; Odom, S. A., Overcharge Performance of 3,7-disubstituted N-Ethylphenothiazine Derivatives in Lithium-ion Batteries. *Chem. Comm.* **2014,** *50*, 5339-5341.

5. Bruker-AXS (2016). APEX3 Bruker-AXS Inc., M., WI, USA.

6. Krause, L.; Herbst-Irmer, R.; Sheldrick, G. M.; Stalke, D., Comparison of Silver and Molybdenum Microfocus X-ray Sources for Single-Crystal Structure Determination. *J. Appl. Crystallogr.* **2015,** *48*, 3-10.

7. Sheldrick, G. M., SHELXT–Integrated Space-Group and Crystal-Structure Determination. *Acta Crystallogr. A* **2015,** *71*, 3-8.

8. Sheldrick, G. M., Crystal Structure Refinement with SHELXL. *Acta Crystallogr. C* **2015,** *71*, 3-8.

9. Prince, E.; Wilson, A. J. C., *International Tables for Crystallography*. 2004.

10. Compton, R. G.; Banks, C. E., *Understanding Voltammetry*. 2nd ed.; Imperial College Press, London: 2011.

11. Milshtein, J. D.; Barton, J. L.; Darling, R. M.; Brushett, F. R., 4-Acetamido-2,2,6,6-tetramethylpiperidine-1-oxyl as a Model Organic Redox Active Compound for Nonaqueous Flow Batteries. *J. Power Sources* **2016,** *327*, 151-159.

12. Goulet, M.-A.; Aziz, M. J., Flow Battery Molecular Reactant Stability Determined by Symmetric Cell Cycling Methods. *J. Electrochem. Soc.* **2018,** *165*, A1466-A1477.

Chapter 4

1. Ergun, S.; Elliott, C. F.; Kaur, A. P.; Parkin, S. R.; Odom, S. A., Overcharge Performance of 3,7-disubstituted N-Ethylphenothiazine Derivatives in Lithium-ion Batteries. *Chem. Comm.* **2014,** *50*, 5339-5341.

2. Zhang, J.; Huang, J.; Robertson, L. A.; Shkrob, I. A.; Zhang, L., Comparing Calendar and Cycle Life Stability of Redox Active Organic Molecules for Nonaqueous Redox Flow Batteries. *J. Power Sources* **2018,** *397*, 214-222.

3. Hammett, L. P., The Effect of Structure Upon the Reactions of Organic Compounds. Benzene Derivatives. *J. Am. Chem. Soc.* **1937,** *59*, 96-103.

4. Dewar, M. J.; Grisdale, P. J., Substituent Effects. I. Introduction. *J. Am. Chem. Soc.* **1962,** *84*, 3539-3541.

5. Kowalski, J. A.; Carney, T. J.; Huang, J.; Zhang, L.; Brushett, F. R., An investigation on the impact of halidization on substituted dimethoxybenzenes. *Electrochim. Acta* **2020,** *335,* 135580.

6. Zhang, Z.; Zhang, L.; Schlueter, J. A.; Redfern, P. C.; Curtiss, L.; Amine, K., Understanding the Redox Shuttle Stability of 3, 5-di-tert-butyl-1, 2-dimethoxybenzene for Overcharge Protection of Lithium-ion Batteries. *J. Power Sources* **2010,** *195,* 4957-4962.

7. Huang, J.; Su, L.; Kowalski, J. A.; Barton, J. L.; Ferrandon, M.; Burrell, A. K.; Brushett, F. R.; Zhang, L., A Subtractive Approach to Molecular Engineering of Dimethoxybenzene-Based Redox Materials for Non-aqueous Flow Batteries. *J. Mater. Chem. A* **2015,** *3,* 14971-14976.

8. Schwager, P.; Bülter, H.; Plettenberg, I.; Wittstock, G., Review of Local In Situ Probing Techniques for the Interfaces of Lithium-Ion and Lithium–Oxygen Batteries. *Energy Technol.* **2016,** *4,* 1472-1485.

9. Moshurchak, L.; Buhrmester, C.; Wang, R.; Dahn, J., Comparative Studies of Three Redox Shuttle Molecule Classes for Overcharge Protection of LiFePO4-Based Li-ion Cells. *Electrochim. Acta* **2007,** *52,* 3779-3784.

10. Wei, X.; Xu, W.; Vijayakumar, M.; Cosimbescu, L.; Liu, T.; Sprenkle, V.; Wang, W., TEMPO-Based Catholyte for High-Energy Density Nonaqueous Redox Flow Batteries. *Adv. Mater.* **2014,** *26,* 7649-7653.

11. Bergner, B. J.; Schürmann, A.; Peppler, K.; Garsuch, A.; Janek, J. r., TEMPO: A Mobile Catalyst for Rechargeable Li-O2 Batteries. *J. Am. Chem. Soc.* **2014,** *136,* 15054-15064.

12. Attanayake, N. H.; Kowalski, J. A.; Greco, K. V.; Casselman, M. D.; Milshtein, J. D.; Chapman, S. J.; Parkin, S. R.; Brushett, F. R.; Odom, S. A., Tailoring Two-Electron-Donating Phenothiazines To Enable High-Concentration Redox Electrolytes for Use in Nonaqueous Redox Flow Batteries. *Chem. Mater.* **2019,** *31,* 4353-4363.

13. Kaur, A. P.; Ergun, S.; Elliott, C. F.; Odom, S. A., 3,7-Bis(trifluoromethyl)-N-ethylphenothiazine: A Redox Shuttle with Extensive Overcharge Protection in Lithium-ion Batteries. *J. Mater. Chem. A* **2014,** *2,* 18190-18193.

14. Milshtein, J. D.; Kaur, A. P.; Casselman, M. D.; Kowalski, J. A.; Modekrutti, S.; Zhang, P. L.; Attanayake, N. H.; Elliott, C. F.; Parkin, S. R.; Risko, C.; Brushett, F. R.; Odom, S. A., High Current Density, Long Duration Cycling of Soluble Organic Active Species for Non-Aqueous Redox Flow Batteries. *Energy Environ. Sci.* **2016,** *9,* 3531-3543.

15. Li, S.; Ai, X.; Yang, H.; Cao, Y., A Polytriphenylamine-Modified Separator with Reversible Overcharge Protection for 3.6 V-Class Lithium-ion Battery. *J. Power Sources* **2009,** *189,* 771-774.

16. Pasala, V.; Ramachandra, C.; Sethuraman, S.; Ramanujam, K., A High Voltage Organic Redox Flow Battery with Redox Couples O2/Tetrabutylammonium Complex and Tris (4-bromophenyl) amine as Redox Active Species. *J. Electrochem. Soc.* **2018,** *165*, A2696-A2702.

17. Dunn, R. P.; Kafle, J.; Krause, F. C.; Hwang, C.; Ratnakumar, B. V.; Smart, M. C.; Lucht, B. L., Electrochemical Analysis of Li-ion Cells Containing Triphenyl Phosphate. *J. Electrochem. Soc.* **2012,** *159*, A2100-A2108.

18. Casselman, M. D.; Kaur, A. P.; Narayana, K. A.; Elliott, C. F.; Risko, C.; Odom, S. A., The Fate of Phenothiazine-based Redox Shuttles in Lithium-ion Batteries. *Phys. Chem. Chem. Phys.* **2015,** *17*, 6905-6912.

19. Chen, Z.; Amine, K., Bifunctional Electrolyte Additive for Lithium-ion Batteries. *Electrochem. Commun.* **2007,** *9*, 703-707.

20. Zhang, L.; Zhang, Z.; Wu, H.; Amine, K., Novel Redox Shuttle Additive for High-Voltage Cathode Materials. *Energy Environ. Sci.* **2011,** *4*, 2858-2862.

21. Moshurchak, L.; Lamanna, W.; Bulinski, M.; Wang, R.; Garsuch, R. R.; Jiang, J.; Magnuson, D.; Triemert, M.; Dahn, J., High-Potential Redox Shuttle for Use in Lithium-ion Batteries. *J. Electrochem. Soc.* **2009,** *156*, A309-A312.

22. Bell, F.; Ledwith, A.; Sherrington, D., Cation-Radicals: tris-(p-Bromophenyl) Amminium perchlorate and hexachloroatimonate. *J. Chem. Soc. (C)* **1969**, 2719-2720.

23. Steckhan, E., Indirect Electroorganic Syntheses—A Modern Chapter of Organic Electrochemistry [New Synthetic Methods (59)]. *Angew. Chem. Int. Ed. Engl* **1986,** *25*, 683-701.

24. Odom, S. A.; Ergun, S.; Poudel, P. P.; Parkin, S. R., A Fast, Inexpensive Method for Predicting Overcharge Performance in Lithium-ion Batteries. *Energy Environ. Sci.* **2014,** *7*, 760-767.

25. Mi, Z.; Yang, P.; Wang, R.; Unruangsri, J.; Yang, W.; Wang, C.; Guo, J., Stable Radical Cation-Containing Covalent Organic Frameworks Exhibiting Remarkable Structure-Enhanced Photothermal Conversion. *J. Am Chem. Soc.* **2019,** *141*, 14433-14442.

26. Fukui, N.; Cha, W.; Shimizu, D.; Oh, J.; Furukawa, K.; Yorimitsu, H.; Kim, D.; Osuka, A., Highly planar diarylamine-fused porphyrins and their remarkably stable radical cations. *Chem. Sci.* **2017,** *8*, 189-199.

27. Maier, J.; Turner, D., Steric Inhibition of Resonance Studied by Molecular Photoelectron Spectroscopy. Part 1.—Biphenyls. *Faraday Discuss. Chem. Soc.* **1972,** *54*, 149-167.

28. Andrews, L.; Arlinghaus, R. T.; Payne, C. K., Absorption Spectra of Substituted Biphenyl and Related Cations in Solid Argon and a Comparison with Photoelectron Spectra. *J. Chem. Soc. Faraday Transl. Mater. Res.* **1983,** *79*, 885-895.

29. Hutchison, G. R.; Ratner, M. A.; Marks, T. J., Hopping Transport in Conductive Heterocyclic Oligomers: Reorganization Energies and Substituent Effects. *J. Am. Chem. Soc.* **2005,** *127*, 2339-2350.

30. Zade, S. S.; Bendikov, M., Twisting of Conjugated Oligomers and Polymers: Case Study of Oligo-and Polythiophene. *Chem. Eur. J.* **2007,** *13*, 3688-3700.

31. Pascal, R. A., Twisted acenes. *Chem. Rev.* **2006,** *106*, 4809-4819.

32. Casselman, M. D.; Elliott, C. F.; Modekrutti, S.; Zhang, P. L.; Parkin, S. R.; Risko, C.; Odom, S. A., Beyond the Hammett Effect: Using Strain to Alter the Landscape of Electrochemical Potentials. *Chemphyschem* **2017,** *18*, 2142-2146.

33. Ergun, S.; Casselman, M. D.; Kaur, A. P.; Attanayake, N. H.; Parkin, S. R.; Odom, S. A., Improved Synthesis of N-Ethyl-3, 7-Bis (Trifluoromethy) Phenothiazine. *New J. Chem.* **2020,** *44*, 11349-11355.

34. Narayana, K. A.; Casselman, M. D.; Elliott, C. F.; Ergun, S.; Parkin, S. R.; Risko, C.; Odom, S. A., N-Substituted Phenothiazine Derivatives: How the Stability of the Neutral and Radical Cation Forms Affects Overcharge Performance in Lithium-Ion Batteries. *ChemPhysChem* **2015,** *16* (6), 1179-1189.

35. Ergun, S.; Elliott, C. F.; Kaur, A. P.; Parkin, S. R.; Odom, S. A., Controlling oxidation potentials in redox shuttle candidates for lithium-ion batteries. *The Journal of Physical Chemistry C* **2014,** *118* (27), 14824-14832.

36. Casselman, M. D.; Elliott, C. F.; Modekrutti, S.; Zhang, P. L.; Parkin, S. R.; Risko, C.; Odom, S. A., Beyond the Hammett Effect: Using Strain to Alter the Landscape of Electrochemical Potentials. *ChemPhysChem* **2017**.

37. Bruker-AXS (2016). APEX3 Bruker-AXS Inc., Madison, WI, USA.

38. Krause, L.; Herbst-Irmer, R.; Sheldrick, G. M.; Stalke, D., Comparison of Silver and Molybdenum Microfocus X-ray Sources for Single-Crystal Structure Determination. *J. Appl. Crystallogr.* **2015,** *48*, 3-10.

39. Sheldrick, G. M., SHELXT–Integrated Space-Group and Crystal-Structure Determination. *Acta Crystallogr. A* **2015,** *71*, 3-8.

40. Sheldrick, G. M., Crystal Structure Refinement with SHELXL. *Acta Crystallogr. C* **2015,** *71*, 3-8.

41. Otwinowski, Z.; Minor, W., [20] Processing of X-ray Diffraction Data Collected in Oscillation Mode. In *Methods Enzymol.*, Elsevier: 1997; Vol. 276, pp 307-326.

42. Compton, R. G.; Banks, C. E., *Understanding Voltammetry*. 2nd ed.; Imperial College Press, London: 2011.

43. Frisch, M.; Trucks, G.; Schlegel, H.; Scuseria, G.; Robb, M.; Cheeseman, J.; Scalmani, G.; Barone, V.; Mennucci, B.; Petersson, G., *Gaussian 09; Gaussian, Inc* **2009,** *32*, 5648-5652.

44. Kaur, A. P.; Harris, O. C.; Attanayake, N. H.; Liang, Z.; Parkin, S. R.; Tang, M. H.; Odom, S. A., Quantifying Environmental Effects on the Solution and Solid-State Stability of a Phenothiazine Radical Cation. *Chem. Mater.* **2020,** *32*, 3007-3017.

45. Roth, H. D., Structure and Reactivity of Organic Radical Cations. In *Photoinduced Electron Transfer IV*, Springer: 1992.

46. Schmittel, M.; Burghart, A., Understanding Reactivity Patterns of Radical Cations. *Angew. Chem. Int. Ed. Engl.* **1997,** *36*, 2550-2589.

47. Connelly, N. G.; Geiger, W. E., Chemical Redox Agents for Organometallic Chemistry. *Chem. Rev.* **1996,** *96*, 877-910.

48. Talipov, M. R.; Rathore, R., Robust Aromatic Cation Radicals as Redox Tunable Oxidants. *Organic Redox Systems: Synthesis, Properties, and Applications* **2015**.

49. Talipov, M. R.; Hossain, M. M.; Boddeda, A.; Thakur, K.; Rathore, R., A Search for Blues Brothers: X-ray Crystallographic/Spectroscopic Characterization of the Tetraarylbenzidine Cation Radical as a Product of Aging of Solid Magic Blue. *Org. biomol. chem.* **2016,** *14*, 2961-2968.

50. Eberson, L.; Larsson, B., Electron Transfer Reactions in Organic Chemistry. IX.* Acyloxylation and/or Debromodimerization Instead of. *Acta Chem. Scand.* **1986,** *40*, 210-225.

Chapter 5

1. Wei, X.; Duan, W.; Huang, J.; Zhang, L.; Li, B.; Reed, D.; Xu, W.; Sprenkle, V.; Wang, W., A High-Current, Stable Nonaqueous Organic Redox Flow Battery. *ACS Energy Lett.* **2016,** *1* (4), 705-711.

2. Milshtein, J. D.; Kaur, A. P.; Casselman, M. D.; Kowalski, J. A.; Modekrutti, S.; Zhang, P. L.; Attanayake, N. H.; Elliott, C. F.; Parkin, S. R.; Risko, C.; Brushett, F. R.; Odom, S. A., High Current Density, Long Duration Cycling of Soluble Organic Active Species for Non-Aqueous Redox Flow Batteries. *Energy Environ. Sci.* **2016,** *9*, 3531-3543.

3. Kwabi, D. G.; Ji, Y.; Aziz, M. J., Electrolyte Lifetime in Aqueous Organic Redox Flow Batteries: A Critical Review. *Chemi. Rev.* **2020**.

4. Leung, P.; Shah, A. A.; Sanz, L.; Flox, C.; Morante, J. R.; Xu, Q.; Mohamed, M. R.; Ponce de Leon, C.; Walsh, F. C., Recent Developments in Organic Redox Flow Batteries: A Critical Review. *J. Power Sources* **2017,** *360*, 243-283.

5. Luo, J.; Hu, B.; Hu, M.; Zhao, Y.; Liu, T. L., Status and Prospects of Organic Redox Flow Batteries towards Sustainable Energy Storage. *ACS Energy Lett.* **2019**.

6. Darling, R. M.; Gallagher, K. G.; Kowalski, J. A.; Ha, S.; Brushett, F. R., Pathways to Low-Cost Electrochemical Energy Storage: A Comparison of Aqueous and Nonaqueous Flow Batteries. *Energy Environ. Sci.* **2014,** *7*, 3459-3477.

7. Kaur, A. P.; Harris, O. C.; Attanayake, N. H.; Liang, Z.; Parkin, S. R.; Tang, M. H.; Odom, S. A., Quantifying Environmental Effects on the Solution and Solid-State Stability of a Phenothiazine Radical Cation. *Chem. Mater.* **2020,** *32*, 3007-3017.

8. Attanayake, N. H.; Kowalski, J. A.; Greco, K.; Casselman, M. D.; Milshtein, J. D.; Chapman, S. J.; Parkin, S. R.; Brushett, F. R.; Odom, S. A., Tailoring Two-Electron Donating Phenothiazines to Enable High Concentration Redox Electrolytes for Use in Nonaqueous Redox Flow Batteries. *Chem. Mater.* **2019,** *31*, 4353-4363.

9. Zhang, J.; Huang, J.; Robertson, L. A.; Shkrob, I. A.; Zhang, L., Comparing Calendar and Cycle Life Stability of Redox Active Organic Molecules for Nonaqueous Redox Flow Batteries. *J. Power Sources* **2018,** *397*, 214-222.

10. Zhang, J.; Yang, Z.; Shkrob, I. A.; Assary, R. S.; Tung, S. o.; Silcox, B.; Duan, W.; Zhang, J.; Su, C. C.; Hu, B.; Pan, B.; Liao, C.; Zhang, Z.; Wang, W.; Curtiss, L. A.; Thompson, L. T.; Wei, X.; Zhang, L., Annulated Dialkoxybenzenes as Catholyte Materials for Non-aqueous Redox Flow Batteries: Achieving High Chemical Stability through Bicyclic Substitution. *Adv. Energy Mater.* **2017,** *7*, 1701272.

11. Huang, J.; Pan, B.; Duan, W.; Wei, X.; Assary, R. S.; Su, L.; Brushett, F. R.; Cheng, L.; Liao, C.; Ferrandon, M. S.; Wang, W.; Zhang, Z.; Burrell, A. K.; Curtiss, L. A.; Shkrob, I. A.; Moore, J. S.; Zhang, L., The Lightest Organic Radical Cation for Charge Storage in Redox Flow Batteries. *Sci. Rep.* **2016,** *6*, 32102-32111.

12. Yan, Y.; Robinson, S. G.; Sigman, M. S.; Sanford, M. S., Mechanism-Based Design of a High-Potential Catholyte Enables a 3.2 V All-Organic Nonaqueous Redox Flow Battery. *J. Am. Chem. Soc.* **2019,** *141*, 15301-15306.

13. Wei, X.; Xu, W.; Huang, J.; Zhang, L.; Walter, E.; Lawrence , C.; Vijayakumar, M.; Henderson, W. A.; Liu, T.; Cosimbescu, L.; Li, B.; Sprenkle, V.; Wang, W., Radical Compatibility with Nonaqueous Electrolytes and Its Impact on an All-Organic Redox Flow Battery. *Angew. Chem. Int. Ed.* **2015,** *54* (30), 8684-8687.

14. Kowalski, J. A.; Casselman, M. D.; Kaur, A. P.; Milshtein, J. D.; Elliott, C. F.; Modekrutti, S.; Attanayake, N. H.; Zhang, N.; Parkin, S. R.; Risko, C.; Brushett, F. R.; Odom, S. A., A Stable Two-Electron-Donating Phenothiazine for Application in Nonaqueous Redox Flow Batteries. *J. Mater. Chem. A* **2017,** *5*, 24371-24379.

145

15. Huang, J.; Su, L.; Kowalski, J. A.; Barton, J. L.; Ferrandon, M.; Burrell, A. K.; Brushett, F. R.; Zhang, L., A Subtractive Approach to Molecular Engineering of Dimethoxybenzene-Based Redox Materials for Non-aqueous Flow Batteries. *J. Mater. Chem. A* **2015,** *3*, 14971-14976.

16. Duan, W.; Huang, J.; Kowalski, J. A.; Shkrob, I. A.; Vijayakumar, M.; Walter, E.; Pan, B.; Yang, Z.; Milshtein, J. D.; Li, B.; Liao, C.; Zhang, Z.; Wang, W.; Liu, J.; Moore, J. S.; Brushett, F. R.; Zhang, L.; Wei, X., "Wine-Dark Sea" in an Organic Flow Battery: Storing Negative Charge in 2,1,3-Benzothiadiazole Radicals Leads to Improved Cyclability. *ACS Energy Lett.* **2017,** *2* (5), 1156-1161.

17. Cosimbescu, L.; Wei, X.; Vijayakumar, M.; Xu, W.; Helm, M. L.; Burton, S. D.; Sorensen, C. M.; Liu, J.; Sprenkle, V.; Wang, W., Anion-Tunable Properties and Electrochemical Performance of Functionalized Ferrocene Compounds. *Sci. Rep.* **2015,** *5*, 14117.

18. Hu, B.; DeBruler, C.; Rhodes, Z.; Liu, T. L., Long-Cycling Aqueous Organic Redox Flow Battery (AORFB) toward Sustainable and Safe Energy Storage. *J. Am. Chem. Soc.* **2017,** *139*, 1207-1214.

19. Hendriks, K. H.; Robinson, S. G.; Braten, M. N.; Sevov, C. S.; Helms, B. A.; Sigman, M. S.; Minteer, S. D.; Sanford, M. S., High-Performance Oligomeric Catholytes for Effective Macromolecular Separation in Nonaqueous Redox Flow Batteries. *ACS Cent. Sci.* **2018,** *4*, 189-196.

20. Wei, X.; Xu, W.; Vijayakumar, M.; Cosimbescu, L.; Liu, T.; Sprenkle, V.; Wang, W., TEMPO-Based Catholyte for High-Energy Density Nonaqueous Redox Flow Batteries. *Adv. Mater.* **2014,** *26*, 7649-7653.

21. Liu, T.; Wei, X.; Nie, Z.; Sprenkle, V.; Wang, W., A Total Organic Aqueous Redox Flow Battery Employing a Low Cost and Sustainable Methyl Viologen Anolyte and 4-HO-TEMPO Catholyte. *Adv. Energy Mater.* **2016,** *6* (3), n/a.

22. Hollas, A.; Wei, X.; Murugesan, V.; Nie, Z.; Li, B.; Reed, D.; Liu, J.; Sprenkle, V.; Wang, W., A Biomimetic High-capacity Phenazine-Based Anolyte for Aqueous Organic Redox Flow Batteries. *Nat. Energy* **2018,** *3*, 508-514.

23. Kwon, G.; Lee, S.; Hwang, J.; Shim, H.-S.; Lee, B.; Lee, M. H.; Ko, Y.; Jung, S.-K.; Ku, K.; Hong, J., Multi-Redox Molecule for High-Energy Redox Flow Batteries. *Joule* **2018,** *2* (9), 1771-1782.

24. Kowalski, J. A.; Neyhouse, B. J.; Brushett, F. R., The Impact of Bulk Electrolysis Cycling Conditions on the Perceived Stability of Redox Active Materials. *Electrochem. commun.* **2019,** *111*, 106625.

25. Odom, S. A.; Ergun, S.; Poudel, P. P.; Parkin, S. R., A Fast, Inexpensive Method for Predicting Overcharge Performance in Lithium-ion Batteries. *Energy Environ. Sci.* **2014,** *7*, 760-767.

26. Kaur, A. P.; Ergun, S.; Elliott, C. F.; Odom, S. A., 3,7-Bis(trifluoromethyl)-N-ethylphenothiazine: A Redox Shuttle with Extensive Overcharge Protection in Lithium-ion Batteries. *J. Mater. Chem. A* **2014,** *2*, 18190-18193.

27. Roth, H. D., Structure and Reactivity of Organic Radical Cations. In *Photoinduced Electron Transfer IV*, Springer: 1992.

28. Perry, M. L.; Saraidaridis, J. D.; Darling, R. M., Crossover mitigation strategies for redox-flow batteries. *Curr. Opin. Electrochem.* **2020**.

29. Goulet, M.-A.; Tong, L.; Pollack, D. A.; Tabor, D. P.; Odom, S. A.; Aspuru-Guzik, A.; Kwan, E. E.; Gordon, R. G.; Aziz, M. J., Extending the Lifetime of Organic Flow Batteries via Redox State Management. *J. Am. Chem. Soc.* **2019,** *141*, 8014-8019.

30. Vaid, T. P.; Sanford, M. S., An Organic Super-Electron-Donor as a High Energy Density Negative Electrolyte for Nonaqueous Flow Batteries. *Chem. Comm.* **2019,** *55* (74), 11037-11040.

31. Hammett, L. P., The Effect of Structure Upon the Reactions of Organic Compounds. Benzene Derivatives. *J. Am. Chem. Soc.* **1937,** *59*, 96-103.

32. Ergun, S.; Elliott, C. F.; Kaur, A. P.; Parkin, S. R.; Odom, S. A., Overcharge Performance of 3,7-disubstituted N-Ethylphenothiazine Derivatives in Lithium-ion Batteries. *Chem. Comm.* **2014,** *50*, 5339-5341.

33. Dai, G.; Gao, Y.; Niu, Z.; He, P.; Zhang, X.; Zhao, Y.; Zhou, H., Dilution of the Electron Density in the π-Conjugated Skeleton of Organic Cathode Materials Improves the Discharge Voltage. *ChemSusChem* **2020**.

34. Ergun, S.; Elliott, C. F.; Kaur, A. P.; Parkin, S. R.; Odom, S. A., Controlling Oxidation Potentials in Redox Shuttle Candidates for Lithium-ion Batteries. *J. Phys. Chem. C* **2014,** *118* (27), 14824-14832.

35. Hernandez-Perez, A. C.; Collins, S. K., A visible-light-mediated synthesis of carbazoles. *Angew. Chem. Int.* **2013,** *52*, 12696-12700.

36. Nielsen, C. B.; Brock-Nannestad, T.; Hammershøj, P.; Reenberg, T. K.; Schau-Magnussen, M.; Trpcevski, D.; Hensel, T.; Salcedo, R.; Baryshnikov, G. V.; Minaev, B. F., Azatrioxa [8] circulenes: Planar Anti-Aromatic Cyclooctatetraenes. *Chem. Eur. J.* **2013,** *19*, 3898-3904.

37. Ergun, S.; Casselman, M. D.; Kaur, A. P.; Attanayake, N. H.; Parkin, S. R.; Odom, S. A., Improved synthesis of N-ethyl-3, 7-bis (trifluoromethyl) phenothiazine. *New J. Chem.* **2020,** *44*, 11349-11355.

38. Robinson, S. G.; Yan, Y.; Hendriks, K. H.; Sanford, M. S.; Sigman, M. S., Developing a predictive solubility model for monomeric and oligomeric cyclopropenium-based flow battery catholytes. *J. Am. Chem. Soc.* **2019,** *141*, 10171-10176.

39. Compton, R. G.; Banks, C. E., *Understanding Voltammetry*. 2nd ed.; Imperial College Press, London: 2011.

Nuwan Harsha Attanayake

Education
Ph.D. Organic Materials Chemistry, University of Kentucky, Lexington, KY, USA
Expected graduation date: December 4, 2020
    Thesis title: Developing and Testing Redox Active Organic Molecules for Nonaqueous
    Redox Flow Battery Applications

B.S. Chemistry, University of Peradeniya, Sri Lanka (2009-2013)

Fellowships, Honors, and Awards
- Outstanding Poster Presentation, KY NSF EPSCoR-Super Collider Annual Meeting. (2018)
- Outstanding Oral Qualifying Exam Award, Department of Chemistry, University of Kentucky. (2018)
- Chair's Scholarship, Department of Chemistry, University of Kentucky. Provided on the basis of outstanding undergraduate record and the high recommendations on the academic performance, scientific capabilities, and accomplishments. (2015)

Peer-Reviewed Publications
9) Liang, Z.; Suduwella, T.M.; Attanayake, N.H.; Kaur, A.P.; Landon, J.; Odom, S.A. "A High Energy Density Organic Redox Flow Battery Operated at -40 °C." Submitted to *ACS Energy Lett.,* nz-2020-019654.

8) Attanayake, N.H.; Kaur, A.P.; Suduwella, T.M.; Parkin, S.R.; Odom, S.A. "A Stable, Highly Reducing Radical Cation." Submitted to *New J. Chem*, NJ-ART-09-2020-004434.

7) Attanayake, N.H.; Liang, Z.; Wang, Y.; Kaur, A.P.; Parkin, S.R.; Mobley, J.K.; Ewoldt, R.H.; Landon, J.; Odom, S.A. "Dual Function Organic Active Materials for Nonaqueous Redox Flow Batteries." Submitted to *Materials Advances,* MA-ART-09-2020-000706.

6) Ergun, S.E.; Casselman, M.D.; Kaur, A.P.; Attanayake, N.H.; Parkin, S.R.; Odom, S.A. "Improved Synthesis of *N*-Ethyl-3,7-Bis(Trifluoromethy)Phenothiazine." *New J. Chem.* 2020, *44*, 11349-11355.

5) Wang, Y.; Kaur, A.P.; Attanayake, N.H.; Yu, Z.; Suduwella, T.M.; Cheng, L.; Odom, 32, 083108. :, R.H. "Viscous flow properties and hydrodynamic diameter of phenothiazine-based redox-active molecules in different supporting salt environments" *Phys. Fluids* **2020**,

4) Kaur, A.P.; Harris, O.; Attanayake, N.H.; Liang, Z.; Parkin, S.R.; Tang M.; Odom, S.A. "Quantifying Environmental Effects on the Solution and Solid-State Stability of Phenothiazine Radical Cations." *Chem. Mater.* 2020, *32*, 3007-3017.

3) Attanayake, N.H.; Kowalski, J.; Greco, K.V.; Casselman, M.D.; Milshtein, J.; Chapman, S.; Parkin, S.R.; Brushett, F.R.; Odom, S.A. "Tailoring Two-Electron Donating Phenothiazines To Enable High Concentration Redox Electrolytes for Use in Nonaqueous Redox Flow Batteries." *Chem. Mater.* 2019, *31,* 4353-4363.

2) Kowalski, J.A.; Casselman, M.D.; Kaur, A.P.; Milshtein, J.D.; Elliott, C.F.; Modekrutti, S.; Attanayake, N.H.; Zhang, N.; Parkin, S.R.; Risko, C.; Brushett, F.R.; Odom, S.A. "A Stable Two-Electron-Donating Phenothiazine for Application in Nonaqueous Redox Flow Batteries." *J. Mater. Chem. A* 2017, *5*, 24371-24379.

1) Milshtein, J.D.; Kaur, A.P.; Casselman, M.D.; Kowalski, J.A.; Modekrutti, S.; Zhang, P.L.; Attanayake, N.H.; Elliott, C.F.; Parkin, S.R.; Risko, C.; Brushett, F.R.; Odom, S.A. "High Current Density, Long Duration Cycling of Soluble Organic Active Species for Non-Aqueous Redox Flow Batteries." *Energy Environ. Sci.* 2016, *9*, 3531-3543.